

Jordan Journal of P H Y S I C S

An International Peer-Reviewed Research Journal

Volume 13, No. 3, December 2020, Jumada 1 1442 H

Jordan Journal of Physics (JJP): An International Peer-Reviewed Research Journal funded by the Scientific Research Support Fund, Jordan, and published biannually by the Deanship of Research and Graduate Studies, Yarmouk University, Irbid, Jordan.

EDITOR-IN-CHIEF:

Ibrahim O. Abu Al-Jarayesh

Department of Physics, Yarmouk University, Irbid, Jordan.

ijaraysh@yu.edu.jo

EDITORIAL BOARD:	ASSOCIATE EDITORIAL BOARD
<p>Prof. Nabil Y. Ayoub <i>President, American University of Madaba, Madaba, Jordan.</i> nabil.ayoub@ju.edu.jo</p>	<p>Prof. Mark Haggmann <i>Desert Electronics Research Corporation, 762 Lacey Way, North Salt Lake 84064, Utah, U. S. A.</i> MHaggmann@NewPathResearch.Com</p>
<p>Prof. Marwan S. Mousa <i>Department of Physics, Mu'tah University, Al-Karak, Jordan.</i> mmousa@mutah.edu.jo</p>	<p>Dr. Richard G. Forbes <i>Dept. of Electrical and Electronic Engineering, University of Surrey, Advanced Technology Institute and Guildford, Surrey GU2 7XH, UK.</i> r.forbes@surrey.ac.uk</p>
<p>Prof. Jamil M. Khalifeh <i>Department of Physics, University of Jordan, Amman, Jordan.</i> jkalifa@ju.edu.jo</p>	<p>Prof. Roy Chantrell <i>Physics Department, The University of York, York, YO10 5DD, UK.</i> roy.chantrell@york.ac.uk</p>
<p>Prof. Abdalmajeid M. Alyassin <i>Department of Physics, Yarmouk University, Irbid, Jordan.</i> alyassin@yu.edu.jo</p>	<p>Prof. Susamu Taketomi <i>2-35-8 Higashisakamoto, Kagoshima City, 892-0861, Japan.</i> staketomi@hotmail.com</p>
<p>Prof. M-Ali H. Al-Akhras (AL-Omari) <i>Department of Physics, Jordan University of Science & Technology, Irbid, Jordan.</i> alakmoh@just.edu.jo</p>	
<p>Prof. Mohammad Al-Sugheir <i>Department of Physics, The Hashemite University, Zarqa, Jordan.</i> msugh@hu.edu.jo</p>	
<p>Prof. Tareq F. Hussein <i>Department of Physics, The University of Jordan, Amman, Jordan.</i> t.hussein@ju.edu.jo</p>	
<p>Prof. Ibrahim A. Bsoul <i>Department of Physics, Al al-Bayt University, Mafraq, Jordan.</i> Ibrahimbsoul@yahoo.com</p>	

Editorial Secretary: Majdi Al-Shannaq.

Languages Editor: Haider Al-Momani

Manuscripts should be submitted to:

Prof. Ibrahim O. Abu Al-Jarayesh
Editor-in-Chief, Jordan Journal of Physics
Deanship of Research and Graduate Studies
Yarmouk University-Irbid-Jordan
Tel. 00 962 2 7211111 Ext. 2075
E-mail: jjp@yu.edu.jo
Website: <http://Journals.yu.edu.jo/jjp>

Jordan Journal of PHYSICS

An International Peer-Reviewed Research Journal

Volume 13, No. 3, December 2020, Jumada 1 1442 H

INTERNATIONAL ADVISORY BOARD

Prof. Dr. Ahmad Saleh

Department of Physics, Yarmouk University, Irbid, Jordan.
salema@yu.edu.jo

Prof. Dr. Aurore Savoy-Navarro

LPNHE Université de Paris 6/IN2P3-CNRS, Tour 33, RdC 4,
Place Jussieu, F 75252, Paris Cedex 05, France.
auore@lfnhep.in2p3.fr

Prof. Dr. Bernard Barbara

Laboratoire Louis Neel, Salle/Room: D 108, 25, Avenue des
Martyrs BP 166, 38042-Grenoble Cedex 9, France.
Barbara@grenoble.cnrs.fr

Prof. Dr. Bruno Guiderdoni

Observatoire Astronomique de Lyon, g, avenue Ch. Antre-F-69561,
Saint Genis Laval Cedex, France.
Bruno.guiderdoni@olos.univ-lyon1.fr

Prof. Dr. Buford Price

Physics Department, University of California, Berkeley, CA 94720,
U. S. A.
bprice@berkeley.edu

Prof. Dr. Colin Cough

School of Physics and Astronomy, University of Birmingham, B15
2TT, U. K.
c.gough@bham.ac.uk

Prof. Dr. Desmond Cook

Department of Physics, Condensed Matter and Materials Physics
Research Group, Old Dominion University, Norfolk, Virginia
23529, U. S. A.
Dcook@physics.odu.edu

Prof. Dr. Evgeny Sheshin

MIPT, Institutskij per. 9, Dogoprudnyi 141700, Russia.
sheshin@lafeet.mipt.ru

Prof. Dr. Hans Ott

Laboratorium fuer Festkorperphysik, ETH Honggerberg, CH-
8093 Zurich, Switzerland.
ott@solid.phys.ethz.ch

Prof. Dr. Herwig Schopper

President SESAME Council, Chairman Scientific Board UNESCO
IBSP Programme, CERN, 1211 Geneva, Switzerland.
Herwig.Schopper@cern.ch

Prof. Dr. Humam Ghassib

Department of Physics, The University of Jordan, Amman 11942,
Jordan.
humamg@ju.edu.jo

Prof. Dr. Khalid Tougan

Chairman of Jordan Atomic Energy Commission, Amman, Jordan.

Prof. Dr. Nasr Zubeidev

President: Al-Zaytoonah University of Jordan, Amman, Jordan.
President@alzaytoonah.edu.jo

Prof. Dr. Patrick Roudeau

Laboratoire de l'Accelérateur, Lineaire (LAL), Université Paris-
Sud 11, Batiment 200, 91898 Orsay Cedex, France.
roudeau@mail.cern.ch

Prof. Dr. Paul Chu

Department of Physics, University of Houston, Houston, Texas
77204-5005, U. S. A.
Ching-Wu.Chu@mail.uh.edu

Prof. Dr. Peter Dowben

Nebraska Center for Materials and Nanoscience, Department of
Physics and Astronomy, 255 Behlen Laboratory (10th and R
Streets), 116 Brace Lab., P. O. Box 880111, Lincoln, NE 68588-
0111, U. S. A.
pdowben@unl.edu

Prof. Dr. Peter Mulser

Institute fuer Physik, T.U. Darmstadt, Hochschulstr. 4a, 64289
Darmstadt, Germany.
Peter.mulser@physik.tu-darmstadt.de

Prof. Dr. Rasheed Azzam

Department of Electrical Engineering, University of New Orleans
New Orleans, Louisiana 70148, U. S. A.
razzam@uno.edu

Prof. Dr. Shawqi Al-Dallal

Department of Physics, Faculty of Science, University of Bahrain,
Manamah, Kingdom of Bahrain.

Prof. Dr. Wolfgang Nolting

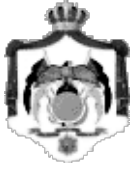
Institute of Physics / Chair: Solid State Theory, Humboldt-
University at Berlin, Newtonstr. 15 D-12489 Berlin, Germany
Wolfgang.nolting@physik.hu-berlin.de

Prof. Dr. Ingo Hofmann

GSI Darmstadt, Planckstr. 1, 64291, Darmstadt, Germany.
i.hofmann@gsi.de

Prof. Dr. Jozef Lipka

Department of Nuclear Physics and Technology, Slovak University
of Technology, Bratislava, Ilkovicova 3, 812 19 Bratislava,
Slovakia.
Lipka@elf.stuba.sk



The Hashemite Kingdom of Jordan



Yarmouk University

Jordan Journal of
PHYSICS

An International Peer-Reviewed Research Journal
Funded by the Scientific Research Support Fund

Volume 13, No. 3, December 2020, Jumada 1 1442 H

Instructions to Authors

Instructions to authors concerning manuscript organization and format apply to hardcopy submission by mail, and also to electronic online submission via the Journal homepage website (<http://jjp.yu.edu.jo>).

Manuscript Submission

1- **E-mail to** : jjp@yu.edu.jo

2- **Online**: Follow the instructions at the journal homepage website.

Original *Research Articles*, *Communications* and *Technical Notes* are subject to critical review by minimum of two competent referees. Authors are encouraged to suggest names of competent reviewers. *Feature Articles* in active Physics research fields, in which the author's own contribution and its relationship to other work in the field constitute the main body of the article, appear as a result of an invitation from the Editorial Board, and will be so designated. The author of a *Feature Article* will be asked to provide a clear, concise and critical status report of the field as an introduction to the article. *Review Articles* on active and rapidly changing Physics research fields will also be published. Authors of *Review Articles* are encouraged to submit two-page proposals to the Editor-in-Chief for approval. Manuscripts submitted in *Arabic* should be accompanied by an Abstract and Keywords in English.

Organization of the Manuscript

Manuscripts should be typed double spaced on one side of A4 sheets (21.6 x 27.9 cm) with 3.71 cm margins, using Microsoft Word 2000 or a later version thereof. The author should adhere to the following order of presentation: Article Title, Author(s), Full Address and E-mail, Abstract, PACS and Keywords, Main Text, Acknowledgment. Only the first letters of words in the Title, Headings and Subheadings are capitalized. Headings should be in **bold** while subheadings in *italic* fonts.

Title Page: Includes the title of the article, authors' first names, middle initials and surnames and affiliations. The affiliation should comprise the department, institution (university or company), city, zip code and state and should be typed as a footnote to the author's name. The name and complete mailing address, telephone and fax numbers, and e-mail address of the author responsible for correspondence (designated with an asterisk) should also be included for official use. The title should be carefully, concisely and clearly constructed to highlight the emphasis and content of the manuscript, which is very important for information retrieval.

Abstract: A one paragraph abstract not exceeding 200 words is required, which should be arranged to highlight the purpose, methods used, results and major findings.

Keywords: A list of 4-6 keywords, which expresses the precise content of the manuscript for indexing purposes, should follow the abstract.

PACS: Authors should supply one or more relevant PACS-2006 classification codes, (available at <http://www.aip.org/pacs/pacs06/pacs06-toc.html>)

Introduction: Should present the purpose of the submitted work and its relationship to earlier work in the field, but it should not be an extensive review of the literature (e.g., should not exceed 1 ½ typed pages).

Experimental Methods: Should be sufficiently informative to allow competent reproduction of the experimental procedures presented; yet concise enough not to be repetitive of earlier published procedures.

Results: should present the results clearly and concisely.

Discussion: Should be concise and focus on the interpretation of the results.

Conclusion: Should be a brief account of the major findings of the study not exceeding one typed page.

Acknowledgments: Including those for grant and financial support if any, should be typed in one paragraph directly preceding the References.

References: References should be typed double spaced and numbered sequentially in the order in which they are cited in the text. References should be cited in the text by the appropriate Arabic numerals, enclosed in square brackets. Titles of journals are abbreviated according to list of scientific periodicals. The style and punctuation should conform to the following examples:

1. Journal Article:

- a) Heisenberg, W., Z. Phys. 49 (1928) 619.
- b) Bednorz, J. G. and Müller, K. A., Z. Phys. B64 (1986) 189
- c) Bardeen, J., Cooper, L.N. and Schrieffer, J. R., Phys. Rev. 106 (1957) 162.
- d) Asad, J. H., Hijjawi, R. S., Sakaji, A. and Khalifeh, J. M., Int. J. Theor. Phys. 44(4) (2005), 3977.

2. Books with Authors, but no Editors:

- a) Kittel, C., "Introduction to Solid State Physics", 8th Ed. (John Wiley and Sons, New York, 2005), chapter 16.
- b) Chikazumi, S., C. D. Graham, JR, "Physics of Ferromagnetism", 2nd Ed. (Oxford University Press, Oxford, 1997).

3. Books with Authors and Editors:

- a) Allen, P. B. "Dynamical Properties of Solids", Ed. (1), G. K. Horton and A. A. Maradudin (North-Holland, Amsterdam, 1980), p137.
- b) Chantrell, R. W. and O'Grady, K., "Magnetic Properties of Fine Particles" Eds. J. L. Dormann and D. Fiorani (North-Holland, Amsterdam, 1992), p103.

4. Technical Report:

Purcell, J. "The Superconducting Magnet System for the 12-Foot Bubble Chamber", report ANL/HEP6813, Argonne Natl. Lab., Argonne, III, (1968).

5. Patent:

Bigham, C. B., Schneider, H. R., US patent 3 925 676 (1975).

6. Thesis:

Mahmood, S. H., Ph.D. Thesis, Michigan State University, (1986), USA (Unpublished).

7. Conference or Symposium Proceedings:

Blandin, A. and Lederer, P. Proc. Intern. Conf. on Magnetism, Nottingham (1964), P.71.

8. Internet Source:

Should include authors' names (if any), title, internet website, URL, and date of access.

9. Prepublication online articles (already accepted for publication):

Should include authors' names (if any), title of digital database, database website, URL, and date of access.

For other types of referenced works, provide sufficient information to enable readers to access them.

Tables: Tables should be numbered with Arabic numerals and referred to by number in the Text (e.g., Table 1). Each table should be typed on a separate page with the legend above the table, while explanatory footnotes, which are indicated by superscript lowercase letters, should be typed below the table.

Illustrations: Figures, drawings, diagrams, charts and photographs are to be numbered in a consecutive series of Arabic numerals in the order in which they are cited in the text. Computer-generated illustrations and good-quality digital photographic prints are accepted. They should be black and white originals (not photocopies) provided on separate pages and identified with their corresponding numbers. Actual size graphics should be provided, which need no further manipulation, with lettering (Arial or Helvetica) not smaller than 8 points, lines no thinner than 0.5 point, and each of uniform density. All colors should be removed from graphics except for those graphics to be considered for publication in color. If graphics are to be submitted digitally, they should conform to the following minimum resolution requirements: 1200 dpi for black and white line art, 600 dpi for grayscale art, and 300 dpi for color art. All graphic files must be saved as TIFF images, and all illustrations must be submitted in the actual size at which they should appear in the journal. Note that good quality hardcopy original illustrations are required for both online and mail submissions of manuscripts.

Text Footnotes: The use of text footnotes is to be avoided. When their use is absolutely necessary, they should be typed at the bottom of the page to which they refer, and should be cited in the text by a superscript asterisk or multiples thereof. Place a line above the footnote, so that it is set off from the text.

Supplementary Material: Authors are encouraged to provide all supplementary materials that may facilitate the review process, including any detailed mathematical derivations that may not appear in whole in the manuscript.

Revised Manuscript and Computer Disks

Following the acceptance of a manuscript for publication and the incorporation of all required revisions, authors should submit an original and one more copy of the final disk containing the complete manuscript typed double spaced in Microsoft Word for Windows 2000 or a later version thereof. All graphic files must be saved as PDF, JPG, or TIFF images.

Allen, P.B., “.....”, in: Horton, G.K., and Muradudin, A. A., (eds.), “Dynamical.....”, (North.....), pp....

Reprints

Twenty (20) reprints free of charge are provided to the corresponding author. For orders of more reprints, a reprint order form and prices will be sent with the article proofs, which should be returned directly to the Editor for processing.

Copyright

Submission is an admission by the authors that the manuscript has neither been previously published nor is being considered for publication elsewhere. A statement transferring copyright from the authors to Yarmouk University is required before the manuscript can be accepted for publication. The necessary form for such transfer is supplied by the Editor-in-Chief. Reproduction of any part of the contents of a published work is forbidden without a written permission by the Editor-in-Chief.

Disclaimer

Opinions expressed in this Journal are those of the authors and neither necessarily reflects the opinions of the Editorial Board or the University, nor the policy of the Higher Scientific Research Committee or the Ministry of Higher Education and Scientific Research. The publisher shoulders no responsibility or liability whatsoever for the use or misuse of the information published by JJP.

Indexing

JJP is currently indexing in:

	<p>Emerging Sources Citation Index (ESCI)</p>	
		

Jordan Journal of
P H Y S I C S

An International Peer-Reviewed Research Journal

Volume 13, No. 3, December 2020, Jumada 1 1442 H

Editorial Preface

This special issue of Jordan Journal of Physics (JJP) presents 18 selected papers presented at the Fourth International Symposium on Dielectric Materials and Applications (ISyDMA 4) that was held Under the Patronage of His Royal Highness Prince Hamzah Bin Al Hussein between 2-4/5/2019 at the IT Auditorium of the University of Jordan. These papers were subjected to standard refereeing of JJP.



Jordan Journal of
P H Y S I C S

An International Peer-Reviewed Research Journal

Volume 13, No. 3, December 2020, Jumada 1 1442 H

Fourth International Symposium on Dielectric Materials and
Applications (ISyDMA 4)
2nd to 4th May 2019
University of Jordan, Amman, Jordan

Guest Editor Preface

Welcome to this Special Issue containing articles selected from the Fourth Int. Symposium on Dielectric Materials and Applications (ISyDMA 4) organized by the Univ. of Jordan (JU), Amman, Jordan and the Jordan University of Science and Technology (JUST), Irbid, Jordan in cooperation with The Jordanian Club of Humboldt Fellows (JCHF), Al-Ahliyya Amman University (AAU), Moroccan Association of Advanced Materials and Moroccan Society of Applied Physics. After three prestigious editions, ISyDMA 1 (Rabat-Kenitra, Morocco, 4-6/5/2016), ISyDMA 2 (Bucharest, Romania, 11-14/7/2017) and ISyDMA 3 (Beni Mellal, Morocco, 18-20/4/2018), a 4th edition of ISyDMA was held in Amman; Under the Patronage of His Royal Highness Prince Hamzah Bin Al Hussein between 2-4/5/2019 at the IT Auditorium of UJ. This event provided an Int. forum for reporting recent developments in advanced dielectric materials and applications with technical, keynote and tutorial sessions covering hot topics in dielectric materials advances.

A Pre-Conf. School was organized by JUST jointly with the ISyDMA 4 at Al Karama Auditorium, JUST, from 30/4 to 1/5/2019, under the chairmanship of Prof. Dr. AL Omari Mohammed-Ali and full support from Dean of Science and Arts Faculty Prof. Dr. Qutaibah T. Khatatbeh. The scope of this School was to familiarize graduate students and junior researchers with the state of art in advanced materials for various applications.

The goal of the ISyDMA 4 Symposium was to provide a platform for researchers, scientists from all over the world to exchange ideas, hold a wide range of discussions on recent developments in dielectric materials and their innovative applications. It addressed materials scientists, physicists, chemists, biologists, and electrical engineers engaged in fundamental and applied research or technical investigations on such materials. It provided an Int. forum to discuss current research on electrical insulation, dielectric phenomena and related topics. The scope of the ISyDMA'4 includes, but is not limited to:

- Dielectric properties, polarization phenomena and applications, physics of space charge in non-conductive materials, polymers, composites, ceramics, glasses, biodielectrics, nanodielectrics, metamaterials, piezoelectric, pyroelectric and ferroelectric materials.

- Impedance spectroscopy applications to electrochemical and dielectric phenomena.
- Dielectrics for superconducting applications, industrial and biomedical applications, dielectric materials for electronics & photonics, diagnostic applications for dielectrics, dielectrics for electrical systems, electrical conduction and breakdown in dielectrics, surface and interfacial phenomena.
- Electrical insulation in high voltage power equipment and cables, ageing, discharges HV insulation, space charge and its effects in dielectrics, gaseous electrical breakdown and discharges.
- High voltage (HV) insulation design using computer based analysis. Partial discharges in insulation: detection methods and impact on ageing, monitoring and diagnostic methods for electrical insulation degradation, measurement techniques, modeling and theory.
- Solar energy Materials.

The accepted papers, offer a good look into the subjects covered by the meeting and are a bit of the 30 oral and 40 poster presentations made in the ISyDMA 4 under chairmanship of Prof. Dr. AL-HUSSEIN Mahmoud (UJ), Prof. Dr. MOUSA Marwan S. (Mu'tah Univ., Al-Karak, Jordan), Prof. Dr. Al OMARI Mohammed-Ali (JUST), Prof. Dr. AL-SOUD Yaseen (Al al-Bayt Univ., Al-Mafraq, Jordan), Dr. SHATNAWI Moneeb (UJ), Dr. JABER Ahmad A. (AAU), Prof. Dr. ACHOUR Mohammed Essaid (Univ. Ibn Tofail, Kenitra, Morocco), Prof. Dr. OUERIAGLI Amane (Cadi Ayyad Univ., Marrakech, Morocco) and Prof. Dr. MABROUKI Mustapha (Sultan Moulay Slimane Univ., Beni-Mellal, Morocco) with help of scientific and organizing Committees.

The Symposium could summarize the reasons for which the Jordan Journal of Physics (JJP) devoted the issue number 02 of volume 13 to various Investigations on dielectric materials. An important reason for the success of the Symposium was the participation of Prof. Dr. COSTA Luis Cadillon (Portugal), Prof. Dr. GRACA Manuel Pedro Fernandes (Portugal), Prof. Dr. MABROUKI Mustapha (Morocco), Prof. Dr. OMARI Ahmad (Jordan), Prof. Dr. PETKOV Plamen (Bulgaria), Prof. Dr. PETKOVA Tamara, (Bulgaria), Prof. Dr. PETRA Uhlmann (Germany), Prof. Dr. POPOV Cyril (Germany) and Prof. Dr. Mahmood Sami H. (Jordan) as plenary conference speakers but the 100 participants created a good and rich scientific atmosphere.

Offering to the Int. Community some results from the conference, acknowledging JJP Editor in Chief Prof. Dr. ABU AL-JARAYESH Ibrahim from Yarmouk Univ., Irbid, Jordan, his Editorial Board and staff for the good job made to extend the Symposium to readers of this journal.

Guest Editors

Prof. Dr. ACHOUR Mohammed Essaid

Prof. Dr. MOUSA Marwan Suleiman

Prof. Dr. AL OMARI Mohammed-Ali

Dr. JABER Ahmad Asaad (Al Ahliyya Amman University)

Jordan Journal of

P H Y S I C S

An International Peer-Reviewed Research Journal

Volume 13, No. 3, December 2020, Jumada 1 1442 H

Fourth International Symposium on Dielectric Materials and Applications (ISyDMA 4)

2th to 4th May 2019

University of Jordan, Amman, Jordan

Prof. Dr. AL-HUSSEIN Mahmoud

Conf. Chairman

University of Jordan, Amman, Jordan

Prof. Dr. MOUSA Marwan Suleiman

Conf. Co-Chairman

Mu'tah University, Al-Karak, Al-karak, Jordan

Prof. Dr. AL OMARI Mohammed-Ali

Pre-Conf. School Chairman

Jordan University of Science and Technology, Irbid, Jordan

Prof. Dr. AL-SOUD Yaseen

Conf. Co-Chairman

Al al-Bayt University, Al-Mafraq, Jordan

Dr. SHATNAWI Moneeb

Conf. Co-Chairman

University of Jordan, Amman, Jordan

Prof. Dr. ACHOUR Mohammed Essaid

Conf. Chairman

University Ibn Tofail, Kenitra, Morocco

Prof. Dr. OUERIAGLI Amane

Conf. Co-Chairman

Cadi Ayyad Univeristy, Marrakech, Morocco

Prof. Dr. MABROUKI Mustapha

Conf. Co-Chairman

Sultan Moulay Slimane University, Beni-Mellal, Morocco

Organizing Committee

Prof. Dr. Mahmoud Al-Hussein

Department of Physics, The University of Jordan, Amman

Prof. Dr. Marwan Mousa

Department of Physics, Mu'tah University, Al-Karak

Prof. Dr. Bashar Lahlouh

Department of Physics, The University of Jordan, Amman

Prof. Dr. Moneeb Shatnawi

Department of Physics, The University of Jordan, Amman

Prof. Dr. Yaseen Alsoud

Dept. of Chemistry Faculty of Science Al al-Bayt University, Al-Mafraq

Prof. Dr. Mohammad El-Khateeb

Department of Applied Chemical Sciences Jordan University of Science and Technology Irbid

Prof. Dr. Mohammed-Ali Al-Omari

Department of Applied Physical Sciences Jordan University of Science and Technology

Prof. Dr. Mousa Jafar

Department of Physics, The University of Jordan, Amman

Prof. Dr. Sami Mahmood

Department of Physics, The University of Jordan, Amman

Prof. Dr. Ibrahim Abu-Aljarayesh

Department of Physics, Yarmouk University, Irbid

Prof. Dr. Qutaibah Khatatbeh

Department of Mathematics and Statistics Jordan University of Science and Technology Irbid

Prof. Dr. Ikhlas Tarawneh

Al-Hussein Bin Talal University

Dr. Ahmad Asaad Jaber

Al-Ahliyya Amman University, Amman

Dr. Inshad Yousef

German-Jordanian University, Amman

Dr. Amer Dakheel Al-Oqali

Physics Department, Mutah University

Dr. Ali Taani

Applied Science Department, Aqaba University College, Al-Balqa' Applied University

Dr. Riad Salem Ababneh

Department of Physics, Yarmouk University Irbid

Dr. Muna Abu-Dalo

Department of Applied Chemical Sciences Jordan University of Science and Technology Irbid

Dr. Nusaiba Al-Nemrawi

Department of Pharmaceutical Technology Jordan University of Science and Technology Irbid

Dr. Wala Al-Tamimi

Department of Physics, The University of Jordan, Amman

Dr. Joseph Bawalsah

Al-Ahliyya Amman University, Amman

Jordan Journal of
P H Y S I C S

An International Peer-Reviewed Research Journal

Volume 13, No. 3, December 2020, Jumada 1 1442 H

Table of Contents:

Articles	Pages
Critical Behavior of Electrical Conductivity for Reduced Graphene Oxide/Epoxy Resin Composites	181-190
Y. Nioua, S. El Bouazzaoui, B. M. G. Melo, P. R. Prezas, M. E. Achour, M. P. F. Graça, L. C. Costa, A. Fattoum and M. E. Touhami	
Analysis of the Various Effects of Coating W Tips with Dielectric EpoxyLite 478 Resin or UPR-4 Resin Coatings under Similar Operational Conditions	191-199
A. Al Soud, A. Knápek and M. S. Mousa	
Electrical Properties in Large Frequency and Temperature Ranges of $Sr_{0.6}Ca_{0.4}TiO_3$ Ceramics	201-210
H. Ait Laasri, A. Tachafine, D. Fasquelle, N. Tentillier, M. Elaatmani, L. C. Costa and J. -C. Carru	
Microstructure and Dielectric Properties of $BaFe_{12}O_{19}$ Hexaferrite Nanoparticles: Effect of Cobalt Addition and Calcination Temperature	211-219
H. Shehabi, M. Rekaby, R. Sayed Hassan and R. Awad	
Dielectric Properties of $Y_3Fe_5O_{12}$ (YIG) Prepared at Different Molarities of NaOH	221-226
B. Assi, Z. Bitar, W. Malaeb and R. Awad	
Effect of the Polyamide Type on the Physical Properties of Layered Polyaniline Composite Films	227-232
D. Mezdour and M. Tabellout	
Graphene and Related 2D Materials for Desalination: A Review of Recent Patents	233-242
M.W. Aqra and A.A. Ramanathan	
Probability Distribution of Magnetic Field Strengths through the Cyclotron Lines in High-Mass X-ray Binaries	243-251
A. Taani, A. Abushattal, A. Khasawneh, N. Almusleh and M. Al-Wardat	
Composite Metallic Nano Emitters Coated with a Layer of Insulator Covered by Au Layer	253-262
A. Al Soud, R. N. Al Buqain and M. S. Mousa	

Critical Behavior of Electrical Conductivity for Reduced Graphene Oxide/Epoxy Resin Composites

Y. Nioua^a, S. El Bouazzaoui^a, B. M. G. Melo^b, P. R. Prezas^b, M. E. Achour^a,
M. P. F. Graça^b, L. C. Costa^b, A. Fattoum^c and M. E. Touhami^d

^aLaboratory of Materials Physics and Subatomic, Faculty, University Ibn Tofail, BP 242, 14000, Kenitra, Morocco.

^bI3N and Physics Department, University of Aveiro, 3810-193 Aveiro, Portugal.

^cResearch Unit of Materials, Environment and Energy, Sciences Faculty of Gafsa, 2112 Gafsa, Tunisia.

^dLaboratoire d'Ingénierie des Matériaux et d'Environnement: Modélisation et Application, Sciences Faculty, University Ibn Tofail, BP 133, 14000, Kenitra, Morocco.

Doi : <https://doi.org/10.47011/13.3.1>

Received on: 08/08/2019;

Accepted on: 5/12/2019

Abstract: In this paper, we analyze the dc and ac electrical conductivities, in the 240 to 400 K temperature range and 10^2 to 10^6 Hz frequency range, of a percolating system synthesized by mixing reduced graphene oxide (rGO) particles in insulating epoxy resin matrix, diglycidyl ether of bisphenol A (DGEBA). We found that the dc electrical conductivity of the samples is strongly related to the rGO content, indicating a percolating behavior with percolation threshold $\phi_C \approx 4\%$. The critical behavior of the dc electrical conductivity as a function of the temperature indicates a strong positive temperature coefficient and a negative temperature coefficient of resistivity below and above the transition temperature T_g , respectively. Moreover, the results showed that the dc conductivity obeys the Arrhenius law and the ac electrical conductivity is both frequency and temperature dependent and follows the Jonscher's power law.

Keywords: Composites, Dielectric properties, Fillers, Glass transition, Graphene.

Introduction

Electrically conductive polymer composite materials, formed by inserting conductive particles, such as graphite, carbon black (CB), carbon nanotubes (CNTs), ... etc., into an insulating polymer matrix, are considered to be an important group of multifunctional materials for many potential engineering applications [1-3]. Since its discovery by Geim's group in 2004 [4], graphene (GE) has proven to be better than other carbonaceous materials concerning many unique properties, such as very large Young's modulus (≈ 1 TPa) and fracture strength (≈ 130

GPa), high thermal conductivity (≈ 5000 W/mK), high electrical conductivity (≈ 6000 S/cm) and high surface area (≈ 2600 m²/g) [5]. These properties attracted great interest in the modern electronics and electrical engineering fields and provide graphene the potential to enhance electronic devices, sensors, energy storage systems, potential battery cells and biomedical applications [6-7]. Recently, extensive investigation has been focused on the exploration of the graphene-based materials properties for the fabrication of nanocomposites

with different polymer matrices [8], on the description of the synthesis methodologies of these nanocomposites and on the characterization of their mechanical properties [9]. However, there is a scarce amount of reports addressing the electrical and dielectric properties of polymer/graphene composite materials. In our previous work [10], we presented the impedance spectroscopy analysis of composite materials, fabricated by mixing reduced graphene oxide (rGO) in an epoxy resin, over a broad frequency and temperature range.

In the present work, our primary interest is to analyze the dc and ac electrical conductivities of epoxy resin polymer loaded with rGO particles, in the 240 to 400 K temperature range over the 10^2 up to 10^6 Hz frequency range. Secondly, we focus our interest on the analysis of the positive temperature coefficient (PTCR) [11-13] and negative temperature coefficient (NTCR) [14] effects which are observed on the electrical measurements, at temperatures below and above the glass transition temperature (T_g). Furthermore, we used some theoretical models dealing with the charge transport mechanisms in disordered materials to fit the experimental results.

Experimental

Materials

The samples investigated in this study are reduced graphene oxide (rGO) particles dispersed in an epoxy resin matrix (DGEBA). The rGO was purchased from Graphenea, with an average particle size of about 260-295 nm, the density is 1.91 g.cm^{-3} and the specific surface area [15] is between 423 and $500 \text{ m}^2.\text{g}^{-1}$. The insulating resin epoxy prepolymer D.E.R. 321 has an epoxy equivalent weight of 180–188 (g/eq), a density of 1.14 g.cm^{-3} at 25 °C, a viscosity of 500–700 (mPa.s) at 25 °C and a glass transition temperature $T_g \approx 360 \text{ K}$. Eight samples with 0 (pure polymer), 2, 3, 4, 6, 8, 10 and 14 wt % of rGO were synthesized by mixing the desired volume fraction ϕ with the prepolymer, followed by the curing process. Gelation took 5 minutes for each sample and subsequently, the mixture was poured into a mold. After a few hours, the samples were unmolded and left to rest for about 24 h, in order to complete the polymerization process and to promote the homogeneity of the inclusion distribution in the polymer matrix [10]. The

sample morphology of the rGO/epoxy composite materials was analyzed using by scanning electron microscopy SEM (SEM, HITACHI S-3200N).

Electrical Measurements

For the electrical measurements, the samples were prepared as discs with a diameter of 15 mm and a thickness of 2 mm and the electrical contacts were formed by painting both opposite faces with a conductive silver paint. The dc electrical conductivity σ_{dc} measurements were made in a helium atmosphere, in the temperature range from 240 to 400 K using a Keithley 617 programmable electrometer. The temperature dependent alternating current (ac) impedance spectra were measured by using an Agilent 4292A impedance analyzer in the C_P-R_P configuration over broad frequency (100 kHz -1 MHz) and temperature ranges (240-400K). The complex admittance $Y^*(\omega) = 1/Z^*(\omega) = G(\omega) + jB(\omega)$ could be converted into the complex permittivity formalism $\epsilon^*(\omega) = \epsilon'(\omega) - j\epsilon''(\omega)$ using the relations $\epsilon'(\omega) = B(\omega)e / \epsilon_0 A \omega$ and $\epsilon''(\omega) = G(\omega)e / \epsilon_0 A \omega$, where A is the cross-sectional area of the sample, e is its thickness and ϵ_0 is the free space permittivity. The terms $G(\omega)$ and $B(\omega)$ are, respectively, the conductance and the susceptance of the samples [16-17]; afterward, the ac electrical conductivity can be calculated using the relation $\sigma_{ac}(\omega) = \omega \cdot \epsilon_0 \cdot \epsilon''$ [16].

Results and Discussion

Morphological Characteristics

The SEM micrographs of the rGO/epoxy nanocomposites, with rGO concentrations of $\phi = 4.42 \%$ and $\phi = 6.21 \%$, are shown in Fig. 1. The reduced graphene oxide particles are selectively dispersed in the epoxy polymer and with further increase of the rGO gradually, a continuous conductive path forms in the polymer matrix. Both micrographs show rGO clusters due to their tendency to agglomerate in the polymer matrix. Aggregation and overlapping structures are easily formed in the graphene/polymer composites, because the graphene nanoparticles have a large specific surface area ($423 - 500 \text{ m}^2/\text{g}$) [14].

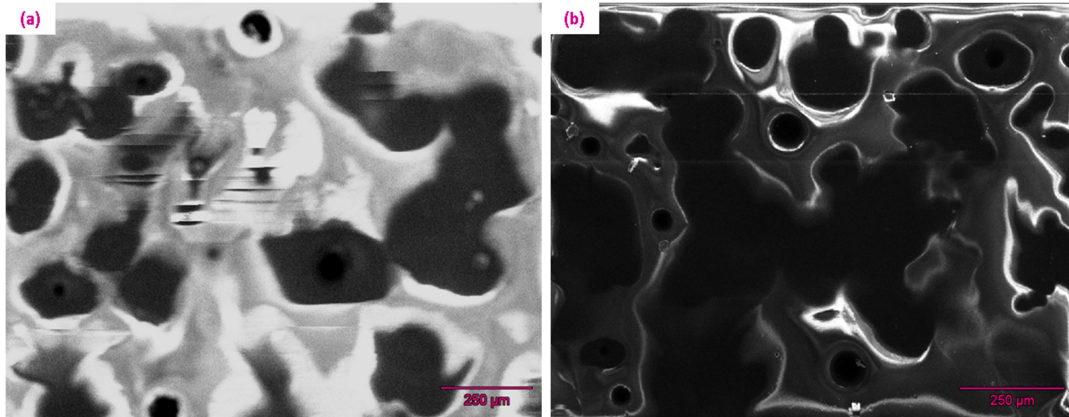


FIG. 1. SEM micrographs of the rGO/epoxy composites with 4.42 % (a) and 6.21 % (b) filler concentrations.

Percolation Threshold

Fig. 2 shows the dc electrical conductivity of the rGO/epoxy composites as a function of the rGO concentration, at room temperature. It is observed that, at very low filler loading, the electrical conductivity is dominated by the insulator polymer matrix and the conductivity values in this range are around 10^{-13} ($\text{S}\cdot\text{m}^{-1}$), typical of dielectric materials. On the other hand, for higher filler loadings, a sharp increase in the electrical conductivity, over 8 orders of magnitude (from 1.52×10^{-11} S/m for 3.66 % to 1.93×10^{-3} S/m for 4.93 % of rGO), is observed. This abrupt transition indicates the formation of an interconnected rGO network, causing a decrease in the distance that separates the sheets.

The percolation threshold is clearly observed and the experimental ϕ_c value was estimated to be around ≈ 4 %. The obtained percolation threshold is higher than those of a series of rGO/polymer composites reported by A. J. Marsden et al. [18]. This disagreement may be related to the shape of the conductive particles (rGO) [19], aggregation and overlapping of reduced graphene oxide due to its large specific surface area [20-21], the viscosity of the composite, because the very low percolation thresholds are always achieved with a low viscosity system [22] and could be also a result of the degree of dispersion between rGO particles and the polymer matrix [22].

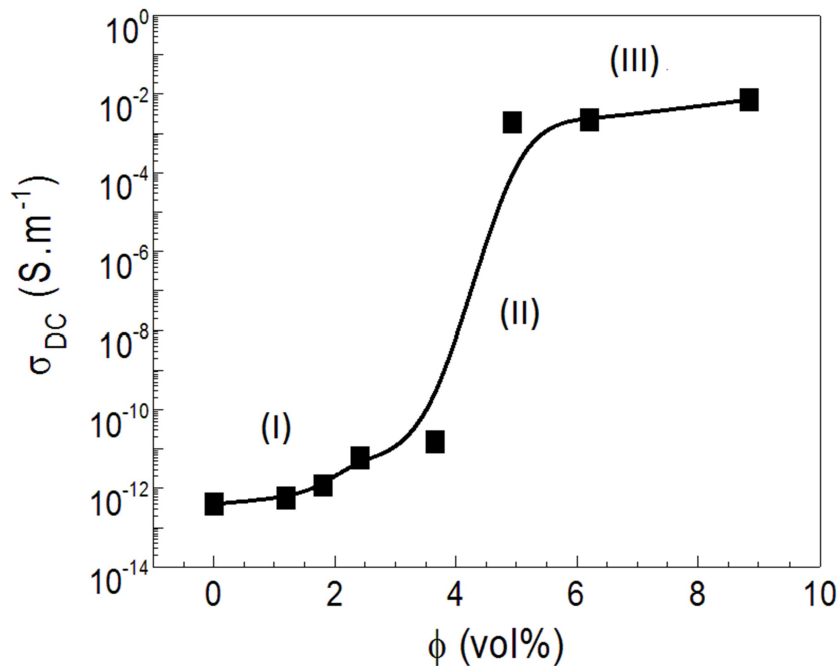


FIG. 2. dc electrical conductivity, σ_{dc} versus rGO concentration in the rGO/epoxy composites, at room temperature $T = 300$ K.

Electrical Resistivity Analysis

The distribution of the conductive particles in a polymer insulating matrix can give rise to electrically conductive polymer composites and some of these materials can exhibit a critical behavior around the glass transition temperature (T_g). Below T_g , some materials show an abrupt increase in resistivity when the temperature changes only over a few degrees. This phenomenon is known as PTCR effect.

Fig. 3 depicts the electrical resistivity ($\rho = 1 / \sigma_{dc}$) of the rGO/epoxy composites as a function of temperature, for concentrations above the percolation threshold. In order to analyze and understand the data presented in Fig. 3, it is necessary to consider three regions: (i) from 240 to $T_g \approx 356$ K [10], in which the resistivity decreases with temperature, which is a typical behavior for semiconductors and insulators; (ii) from 356 to 380 K, where the opposite behavior is observed, typical of

conductive materials: an increase of the electrical resistivity with temperature, showing a PTCR effect. The mechanism responsible for this behavior may be attributed to the tunneling effect and it can be explained as follows: above a critical temperature (T_g), the epoxy polymer volume expansion is enhanced and the interparticle distance tends to rapidly increase with increasing temperature, causing a sharp increase in the resistivity [12, 23-24]; (iii) Above 380 K, a similar variation occurs as observed in (i). In the latter temperature region, one can see a decrease of the resistivity with increasing temperature, showing the NTCR effect. It is generally accepted that the NTCR effect is attributed to the reaggregation of the conductive fillers and the reformation of the conductive networks [14]. Overall, one can say that the electrical resistivity temperature variation of the composite materials above the threshold filler concentration is consistent with a PTCR effect above the glass transition temperature T_g .

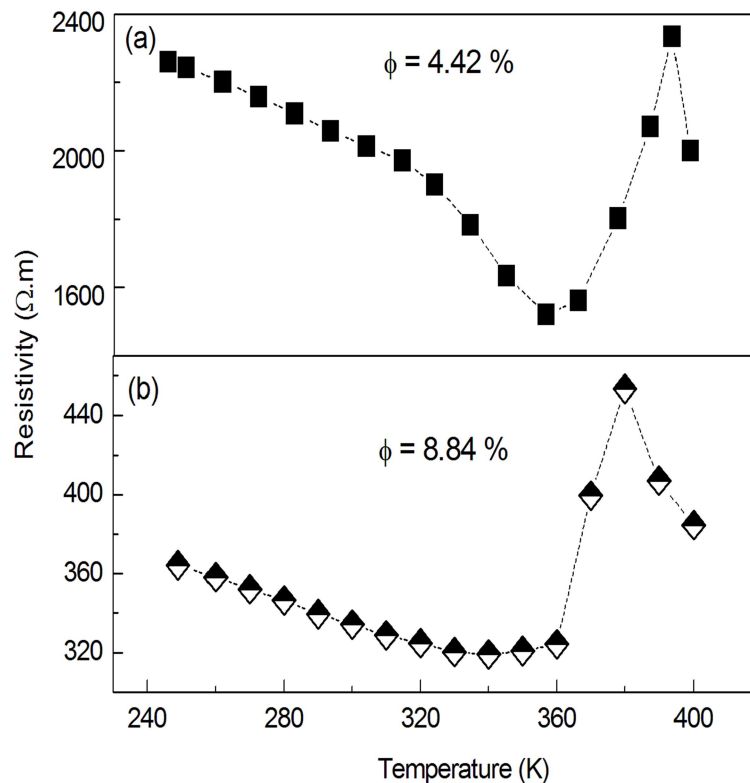


FIG. 3: Temperature dependence of the resistivity of the rGO/epoxy composites, for concentrations above the percolation threshold 4.42 % (a), 6.21% (b) and 8.84 % (c).

For further discussion of the PTCR effect, it is important to consider the PTCR intensity I_{PTC} , defined as the ratio of the maximum resistivity

(ρ_{max}) to the resistivity at room temperature (ρ_{RT}), which can be calculated from the temperature dependence of the composite's resistivity, as shown in Eq. (1) [23]:

$$I_{PTC} = \frac{\rho_{max}}{\rho_{RT}} \quad (1)$$

Fig. 4a shows the PTC intensity of the rGO/epoxy composites as a function of the rGO content, for concentrations above the percolation threshold. As expected, the rGO concentration has a significant influence on the PTC intensity. We see that the highest value is obtained for $\phi \approx 6.21\%$, then it decreases with increasing rGO content. Fig. 4b and Fig. 4c show some results of the PTC intensity from other rGO/epoxy composites of our previous works, made from epoxy resin-filled carbon nanotubes (CNTs); namely, CNT/polyester composite (Fig. 4b) [16] and CNT/epoxy composite (Fig. 4c)

[25]. These indicate that the I_{PTC} for the rGO/epoxy is relatively high compared to the other polymeric composite materials; this result can be explained by the strong agglomeration of the conductive particles (rGO) in the polymer matrix, because agglomeration may have a strong influence on the PTCR effect of the composite materials [14]. Additionally, we would like to indicate that the increase of resistivity with the increment of the temperature seen in the rGO/epoxy composites has been largely studied and such information is critical for the development of multifunctional polymer composites. A similar study has also been reported by Jun-Wei Zha et al. [26] for CB/MWNT/HDPE and CB/HDPE composites' materials.

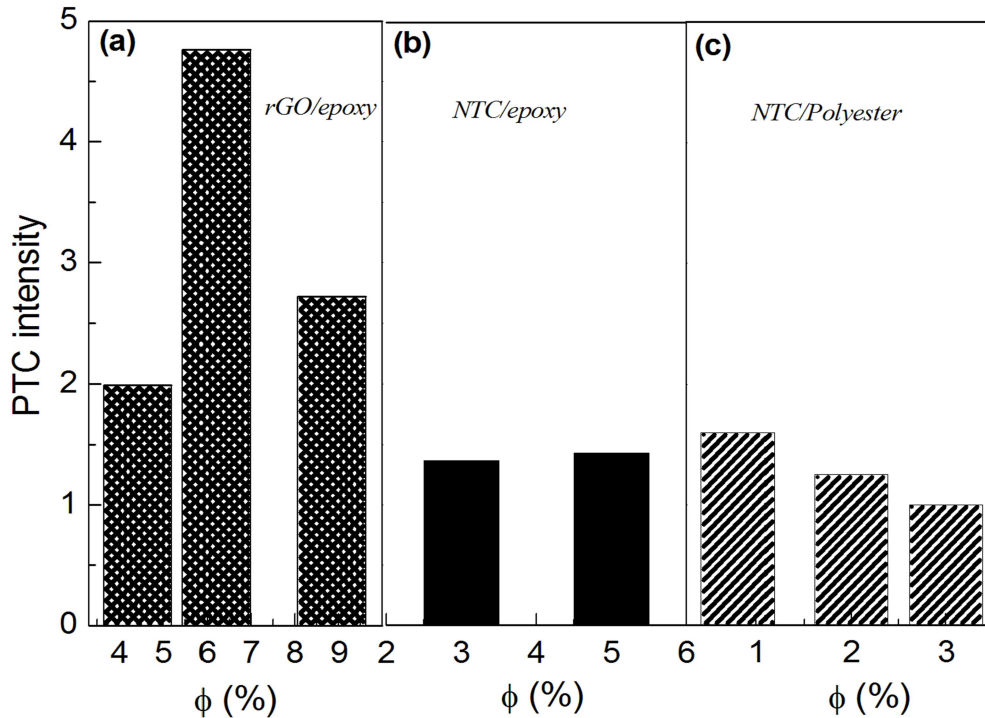


FIG. 4. PTC intensity of the rGO/epoxy composites compared with other systems from our previous works.

AC Electrical Conductivity Analysis

To a better understanding of the frequency and temperature dependence of the electrical properties of the studied samples, ac electrical conductivity measurements were carried out for all samples. Fig. 5 summarizes the ac conductivity as a function of frequency for several temperatures, for a concentration below the percolation threshold (3.66 %). It is visible

that at low frequencies, the ac electrical conductivity remains constant, especially for high temperatures; this is attributed to the dc electrical conductivity contribution. At higher frequencies, it becomes strongly frequency and temperature dependent and increases with increasing frequency for all the evaluated temperatures.

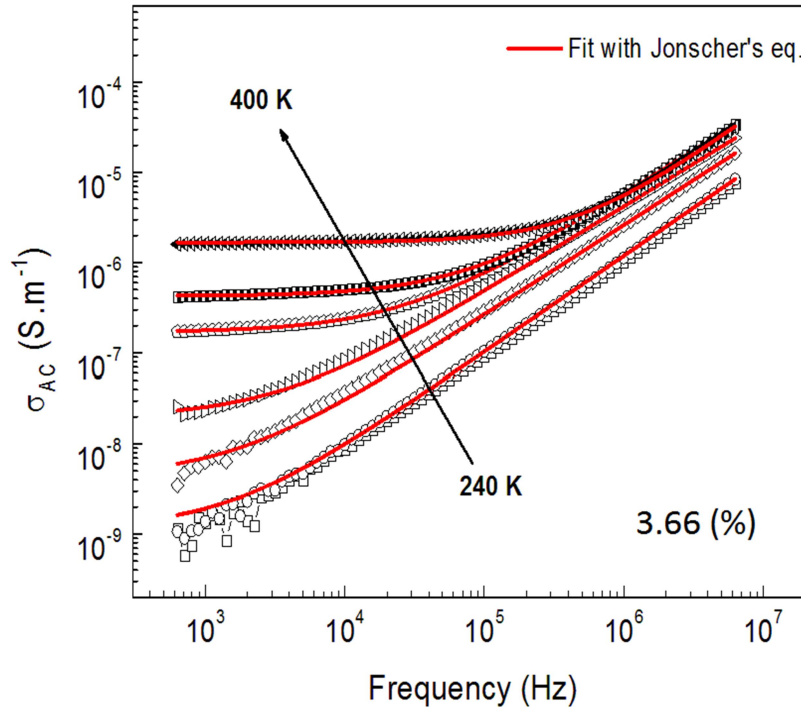


FIG. 5. Ac conductivity as a function of the frequency for various temperatures, for a concentration below the percolation threshold, 3.66 %. The solid curve represents the fitting according to the Jonscher's universal power law.

Fig. 6 reports the obtained results for $\phi \approx 6.21\%$; i.e., above the percolation threshold. It is also clear that the ac electrical conductivity is both frequency and temperature dependent. At low frequencies, σ_{ac} remains constant or tends to constant values, but it is strongly dependent on the temperature. The low-frequency plateau in σ_{ac} consists of the dc conductivity contribution. At higher frequencies, the conductivity becomes strongly frequency dependent and the origin of this behavior is related to the relaxation phenomena arising from mobile charge carriers [27]. The observed frequency dependence of the ac conductivity can be described by the Jonscher's universal power law [27-28].

$$\sigma_{ac}(\omega, T) = \sigma_{dc} + A\omega^s \quad (2)$$

where σ_{dc} is the frequency independent component of the ac conductivity, ω is the angular frequency, A is a temperature dependent parameter and the exponent s is interpreted as a measure of the degree of interaction between the charge carriers and the environment in their

vicinity [29]. In general, the exponent s values are in the $0 \leq s \leq 1$ range. The experimental values of s , extracted using the Jonscher's power law in the σ_{ac} plots of the rGO/epoxy composites (at 300 K), for concentrations below and above percolation threshold, are reported in our previous work [10]. For samples above the percolation threshold, we can see that the temperature effect on the ac electrical conductivity shows a PTCR and NTCR effect below and above the glass transition temperature T_g , respectively. This can be clearly observed in Fig. 6, for 6.21 % of rGO, as an example. Three distinct regions are observed: below 350 K, where there is an increase of the ac electrical conductivity with increasing temperature (Fig. 6a), from 360 to 380 K (Fig. 6b), where an opposite behavior is observed, indicating the PTCR effect and finally, the results above 380 K (Fig. 6c) indicate an NTCR effect. A similar phenomenon has also been reported by K. Abazine et al. [16] for CNT/polyester composites below and above the glass transition temperature.

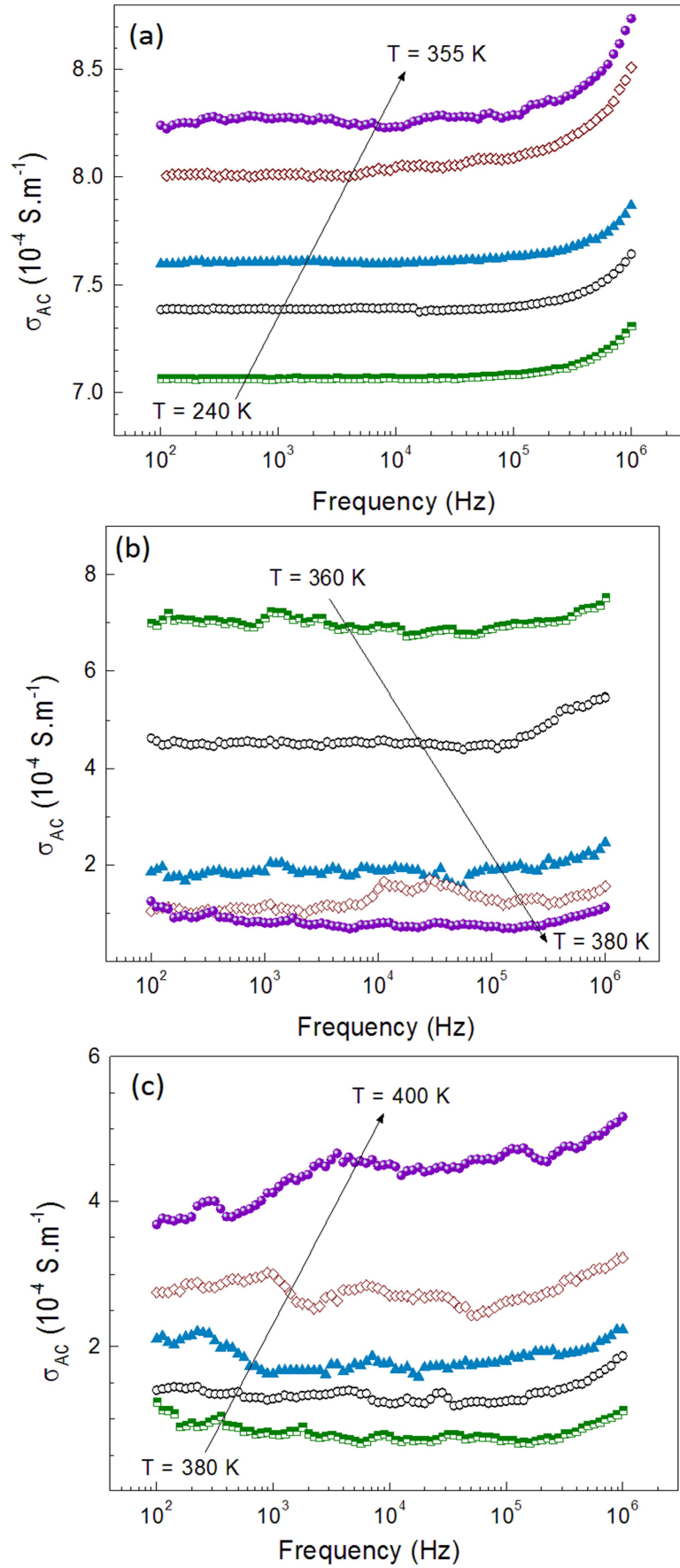


FIG. 6. Frequency dependence of the ac conductivity, σ_{ac} for a concentration above the percolation threshold, 6.21 %, for temperatures below and above the glass transition (T_g).

The experimental values of the s parameter are plotted in Fig. 7 for samples above the percolation threshold, where one can see that it is temperature dependent and we can identify the three distinct domains, for all samples. The typical value of s between 0 and 1 suggests ac conductivity through a hopping mechanism. The

highest value of s describes a completely correlated system. In our case, the obtained value is low, which can be related to the effect of the distribution of relaxation path times and the degree of interaction between the charge carriers and the environment in their vicinity.

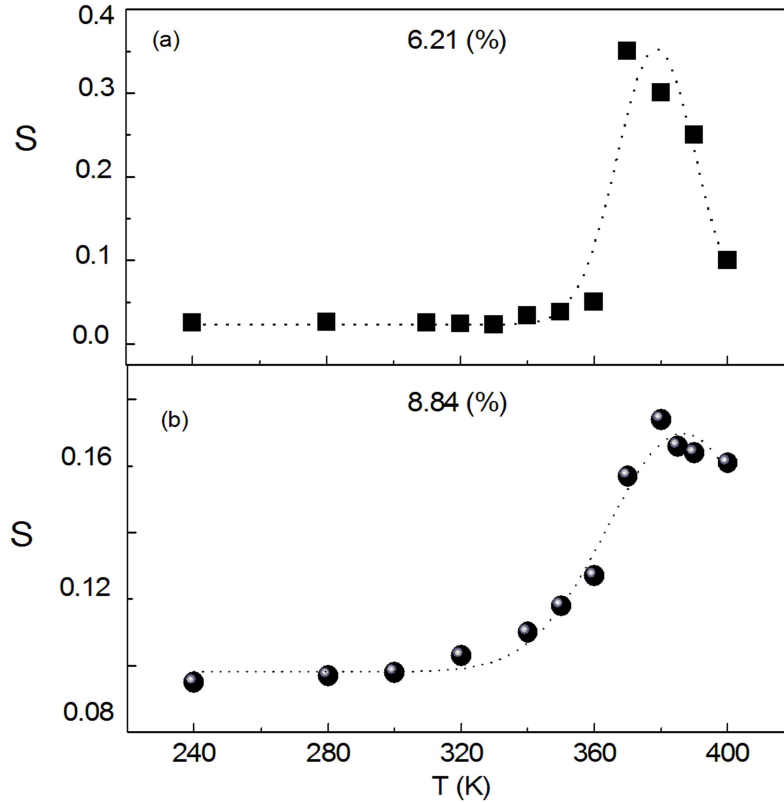


FIG. 7. Jonscher's exponent s versus temperature for concentrations above the percolation threshold, (a) 6.21 % and (b) 8.84 %.

In addition, Fig. 8 illustrates the $\ln(\sigma_{dc})$ dependence with the inverse of the temperature above $T_g \approx 360$ K, for composites with composition below and above the percolation threshold. Above the percolation threshold ϕ_C (Fig. 8b), a change in the slope of the $\ln(\sigma_{dc})$ versus $1000/T$ plot, around $T \approx 380$ K, is visible. As one can see, σ_{dc} increases exponentially with the temperature, indicating that the conductivity is thermally activated. The dependency was found to follow an Arrhenius behavior, as expressed by Eq. (3):

$$\sigma_{dc} = \sigma_0 \cdot \exp\left(\frac{-E_a}{k_B \cdot T}\right) \quad (3)$$

where σ_0 is a pre-exponential factor, E_a is the activation energy, k_B is the Boltzmann's constant and T is the temperature. The values of the activation energy for the various rGO concentrations below and above the percolation threshold were calculated and illustrated in Table 1.

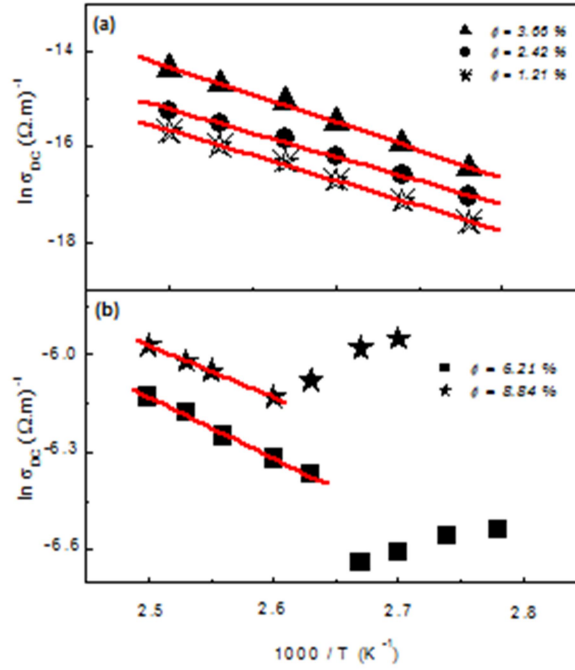


Fig. 8: Arrhenius plot of the dc conductivity *versus* $1000/T$ for concentrations of rGO particles below (a) and above (b) the percolation threshold. The solid lines are the least square linear fits to the Arrhenius relation.

Table 1. The activation energy for the various rGO concentrations below and above the percolation threshold $\phi_c \approx 4\%$, for the composite rGO/DGEBA.

Concentration (%)	1.21	2.42	3.66	6.21	8.48
$E_a (eV)$	1.02	0.93	0.88	0.08	0.015

As can be seen in this table, there is a decrease of the activation energy as the filler concentration increases; this behavior may be due to an increase of polarization energy and/or charge carrier density, leading to a decrease of the domain boundary potential of rGO into the epoxy polymer matrix.

Conclusion

We described the dc and ac electrical conductivities of percolative systems, synthesized by mixing rGO particles in an epoxy resin polymer, below and above the percolation threshold. The dc electrical conductivity is strongly dependent on the rGO content, indicating a percolating behavior with a percolation threshold around $\approx 4\%$. This relatively high value can be explained by the shape of the rGO particles and their tendency for agglomeration in the polymer matrix. The temperature dependence of the electrical conductivity obeys the Arrhenius law and indicates that there is a negative temperature coefficient in resistivity (NTCR) for concentrations below the percolation threshold $\phi \leq \phi_c$. Above the percolation threshold, $\phi \geq \phi_c$, three regions are observed: below 350 K, there is

an increase of the electrical conductivity with increasing temperature, from 360 to 380 K an opposite behavior is observed, indicating a positive temperature coefficient in resistivity (PTCR) effect and finally, above 380 K, the measurements indicate an NTCR effect. A comparison of the rGO/epoxy composites' PTCR effect with other different composites from our previous works indicates that the PTC intensity of the rGO/epoxy samples is significantly higher compared to those of the other polymeric materials. Finally, the ac electrical conductivity is both frequency and temperature dependent and follows the Jonscher's power law.

Acknowledgements

The authors acknowledge FCT-CNRST bilateral cooperation and FEDER by funds through the COMPETE 2020 Program and National Funds through FCT - Portuguese Foundation for Science and Technology under the project UID/CTM/50025/2013. Also B. Melo Acknowledges Fundação para a Ciência e Tecnologia (FCT) for the PhD grant (SFRH/BD/117487/2016).

References

- [1] Huang, Z.M., Zhang, Y.Z., Kotaki, M. and Ramakrishna, S., *Compos. Sci. Technol.*, 63 (2003) 2223.
- [2] Spitalsky, Z., Tasis, D., Papagelis, K. and Galiotis, C., *Prog. Mater. Sci.*, 35 (2010) 357.
- [3] Dang, Z.M., Wang, L., Yin, Y., Zhang, Q. and Lei, Q.Q., *Adv. Mater.*, 19 (2007) 852.
- [4] Novoselov, K.S., Geim, A.K., Morozov, S.V., Jiang, D., Zhang, Y., Dubonos, S.V., Grigorieva, I.V. and Firsov, A.A., *Science*, 306 (2004) 666.
- [5] Dongrui, W., Xiaoman, Z., Zha, J.W., Zhao, J., Dang, Z. and Guo, H.H., *Polymer*, 54 (2013) 1916.
- [6] Huang, X., Yin, Z., Wu, S., Qi, X., He, Q., Zhang, Q., Yan, Q., Boey, F. and Zhang, H., *Small*, 7 (14) (2011) 1876.
- [7] Tapan, D.K. and Smita, P., *Poly-Plastics Tech. Eng.*, 52 (2013) 319.
- [8] Galpaya, D., Wang, M., Liu, M., Motta, N., Waclawik, E. and Yan, C., *Graphene*, 1 (2012) 30.
- [9] Kuilla, T., Srivastava, S.K. and Bhowmick, A.K., *J. Appl. Polym. Sci.*, 111 (2009) 635.
- [10] Nioua, Y., El Bouazzaoui, S., Melo, B.M.G., Presas, P.R., Graca, M.P.F., Achour, M.E., Costa, L.C. and Brosseau, C., *J. Mater. Sci.*, 52 (2017) 13790.
- [11] Costa, L.C., Chakki, A., Achour, M.E. and Graca, M.P.F., *Physica B*, 406 (2011) 245.
- [12] Jun-Wei, Z., Wei-Kang, L., Rui-Jin, L., Jinbo, B. and Zhi-Min, D., *J. Mater. Chem. A*, 1 (2013) 843.
- [13] Min-Kang, S. and Soo, J.P., *Bull. Korean Chem. Soc.*, 30 (2009) 1337.
- [14] Shuaiguo, Z., Dandan, L., Pengfei, Z., Guojie, L., Kun, D., Guo, J., Guoqiang, Z., Chuntai, L., Changyu, S. and Zhanhu, G., *J. Mater. Chem. C*, 5 (2017) 8233.
- [15] <http://www.graphenea.com/collections/graphene-oxide/products/reduced-graphene-oxide-1-gram> [accessed on 01 December 2016].
- [16] Abazine, K., Anakiou, H., El Hasnaoui, M., Graça, M.P.F., Fonseca, M.A., Costa, L.C., Achour, M.E. and Oueriagli, A., *J. Compos. Mater.*, 50 (2016) 3282.
- [17] El Hasnaoui, M., Graça, M.P.F., Achour, M.E., Costa, L.C., Lahjomri, F., Outzourhit, A. and Oueriagli, A., *J. Mater. Environ. Sci.*, 2 (2011) 1.
- [18] Marsden, A.J., Papageorgiou, D.G., Valles, C., Liscio, A., Palermo, V., Bissett, M.A., Young, R.J. and Kinloch, I.A., *2D Materials*, 5 (2018) 1.
- [19] Costa, L.C., Henry, F., Valente, M.A., Mendiratta, S.K. and Sombra, A.S., *Eur. Polym. J.*, 38 (2002) 1495.
- [20] Kuilla, T., Bhadra, S., Yao, D., Kim, N.H., Bose, S. and Lee, J.H., *Prog. Poly. Sci.*, 35 (2010) 1350.
- [21] Singh, V., *Prog. Mater. Sci.*, 56 (2011) 1178.
- [22] Ma, P-C., Siddiqui, N.A. and Marom, G., *Compos., Part A: Appl. Sci. Manuf.*, 41 (2010) 1345.
- [23] Soo-Jin, P.H., Min-K, S. and Jae-Rock, L., *Carbon Science*, 2 (2001) 159.
- [24] Costa, L.C. and Henry, F., *J. Mater. Sci. Lett.*, 22 (2003) 699.
- [25] Boukheir, S.A., Len, A., Fūzi, J., Kenderesi, V., Achour, M.E., Éber, N., Costa, L.C., Oueriagli, A. and Outzourhit A., *Polymer Composites*, 50 (2017) 183.
- [26] Jun-Wei, Z., Dong-Hong, W., Yu, Y., Yun-Hui, W., Robert, K., Lib, Y. and Zhi-Min, D., *RSC. Adv.*, 7 (2017) 11338.
- [27] Jonscher, A.K., *J. Mater. Sci.*, 13 (1978) 553.
- [28] Jonscher, A.K., *Nature*, 267 (1977) 673.
- [29] Momin, H. K., *Adv. Mat. Lett.*, 5 (2014) 384.

Analysis of the Various Effects of Coating W Tips with Dielectric Epoxylite 478 Resin or UPR-4 Resin Coatings under Similar Operational Conditions

A. Al Soud^a, A. Knápek^b and M. S. Mousa^a

^a *Surface Physics and Materials Technology Lab, Department of Physics, Mutah University, Al-Karak 61710, Jordan.*

^b *Institute of Scientific Instruments of the CAS, Královopolská 147, 612 64 Brno, Czech Republic.*

Doi : <https://doi.org/10.47011/13.3.2>

Received on: 28/11/2019;

Accepted on: 10/4/2020

Abstract: The objective of this work is to study the differences that occur in behavior and properties of the emitted electron beam from tungsten (W) tips before and after coating these tips with a thin layer of a good proven dielectric material. Core metallic tips have been prepared from a polycrystalline (99.995% purity) tungsten (W) wire. Analysis has been carried out for clean W emitters before and after coating these tips with two differences types of epoxy resins; namely: (Epoxylite 478 and UPR-4). For critical comparison and analysis, several tungsten tips with various apex- radii (very sharp) have been prepared with the use of electrochemical etching techniques. The tips have been coated by dielectric thin films of various thicknesses. Their characteristics have been recorded before and after the process of coating. These measurements have included the current-voltage (I-V) characteristics, Fowler-Nordheim (F-N) plots, visible light microscope (VLM) image and scanning electron microscope (SEM) micrographs to measure the influence of the Epoxylite resin coating's thickness on the tips after coating. Special distributions have been recorded from the phosphorescent screen of a field electron emission microscope as well. Comparing the two sets of composite systems tested under similar conditions has provided several advantages. Recording highly interesting phenomena has produced a wide opportunity to develop a new type of emitter that includes the most beneficial features of both types.

Keywords: Cold field emission, Epoxylite 478, Epoxylite UPR-4..

Introduction

Field electron emission (FEE) is a process of electron emission from the surface of metals into vacuum due to an intense applied external electric field $E > 10^9$ V/m [1]. The emitter is usually formed into a tiny tip, which has an apex radius ranging from several nanometers to micrometers. When preparing very sharp field emitters, it is essential to use a metal with the possibly highest quality. In this work,

experiments have used polycrystalline Tungsten from high-purity tungsten wires. Due to the favorable properties of those Polycrystalline Tungsten emitters, such as the highest melting point (3650 K) of all the pure metals, the second-highest of all over the periodic table after carbon, high hardness (strength), work function (4.5 eV) and heat resistance at high temperature [2], this type of emitter sources has been widely used in this field research. Within this work, tungsten

micrometers with different apex radii ranging from 100-150 nm have been prepared and coated with a thin layer of various types of epoxy resins (EpoxyLite 478 resins or EpoxyLite UPR-4 resins), where the thickness of epoxy layer range is 40-70 nm by using electron microscopes to extract the tip's profile and thickness of epoxy layer (i.e., apex radii). The emission images were directly photographed from the phosphor screen of the field electron microscope (FEM), using a digital camera. The current-voltage (I-V) measurements and Fowler–Nordheim (F-N) plots have been carried out under vacuum (UHV) conditions with a base pressure of about 10^{-7} Pa.

Experimental Techniques

The tungsten emitters have been prepared by electrolytic etching. A 0.1mm tungsten wire is immersed into an electrolyte 2 molar (NaOH) solution, where the emitter was placed in a stainless steel conductive cylinder. The anode (emitter) and the cathode (steel cylinder) have been immersed into the (NaOH) solution and connected to a DC power source (12 V). The time taken to etch is around 5 minutes and when immersing approx. (0.6-0.8) cm of tungsten wire into NaOH solution, the etching current started at approx. 4 μ A and its value is decreased as the wire becomes thinner with time and continued until the bottom part of the wire is dropped off. There were many requirements needed to be followed to prepare very sharp tips [5]: 1) sufficient surface wettability of the etched wire. 2) sufficient chemical clarity of the used chemicals. 3) accurate depth when immersing the wire. 4) etching source capable of disconnecting the etch current in a very short time. 5) sufficient immunity to mechanical vibrations. Fig. 1 shows the experimental setup to electrical etching and coating. When the bottom part drops off, the resistance of the etching circuit suddenly increases and then, the DC voltage source is quickly switched off. At large, the switch-off time in the etching system greatly affects the sharpness of the tip. Then, the W wire has been carefully pulled from the solution, where the tip was immediately cleaned by carefully dipping it into alcohol and distilled water for a few seconds, respectively. Besides, the tip has been placed in the ultrasonic bath for 15 minutes to clean it from the oxide layers formed on the tip surface [6].

To coat the emitter with a 60-nm thick epoxy layer (using commercial resins marked: EpoxyLite 478 resins and EpoxyLite UPR-4 resins), the tip has to be immersed 4 times into the resin very slowly and vertically as follows: the sample holder that keeps the sample in a vertical position is mounted on a trolley that moves vertically and lowers into a flask of epoxy resin and the tip while a 90° angle between the surface of the epoxy resin and the tip is maintained [7]. To ensure an even distribution of resin on the surface of the tip and stabilize the epoxy resin on tip surface, the coated tip is transferred into a furnace and subjected to 30-minute curing at 373 K to drive off the solvent, followed by thirty minutes at 453 K to complete the curing of the resin [2,7].

Then, the composite emitter is mounted in a standard field emission microscope (FEM) with an emitter screen distance of 1 cm [5, 7-9]. The emission images have been directly photographed from a phosphor screen coated by tin oxide layers. All experiments have been performed under a very low pressure $\sim 10^{-7}$ Pa, which is the ultra-high vacuum (UHV) that requires to be baked at temperatures about 453 K for 12 hours [2,10]. Before adding the liquid nitrogen to the trap, the radius of each emitter's apex is determined from an image taken in a 30 kV SEM at magnifications up to 1000 X.

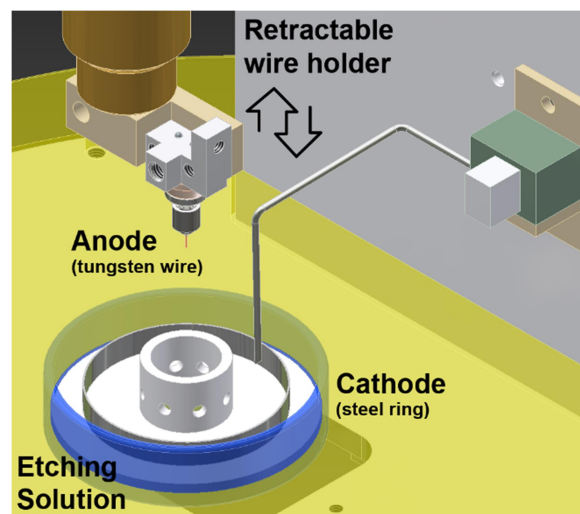


FIG. 1. The set-up of the electrolytic etching process.

Results and Discussion

The prepared tungsten micro emitters have apex radii from 100 nm to 130 nm. Presented results include VLM and SEM images of emitter's apex, I-V characteristics, as well as F-N type plots of the field emission characteristics.

Fig. 2A shows the VLM image for uncoated emitter type 1, which has an approximately hemispherical apex. The measured tip radius is 120 nm. Fig. 2B shows the VLM image for uncoated emitter type 2, which has an approximately hemispherical apex. The measured radius is 110 nm. Fig. 3 shows the emission current pattern for uncoated emitter type 1. Fig. 4 shows the emission pattern for the uncoated emitter type 2. The FEM images

(emission current pattern) primarily consist of multi bright spots for the uncoated emitter type 1. The duration time among the obtained images is approx. 15 minutes, as shown in Fig. 5. The FEM images (emission current pattern) primarily consist of multi bright spots for uncoated emitter type 2. The duration time between obtaining the next images is 15 minutes, as shown in Fig. 6. I-V characteristics and FN plots for the uncoated emitters are shown in Fig. 7 A, B.

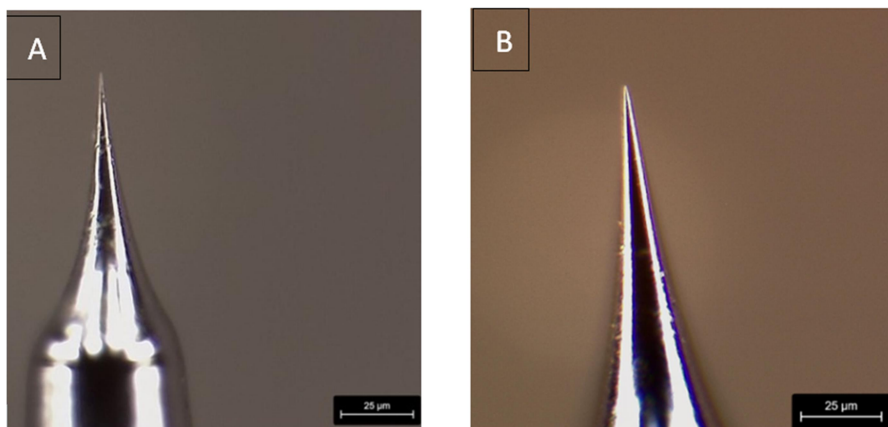


FIG. 2. A) Uncoated emitter type 1, while presenting in a visible light microscope image (X 2500). B) Uncoated emitter Type 2, while presenting in a visible light microscope image (X 2500).

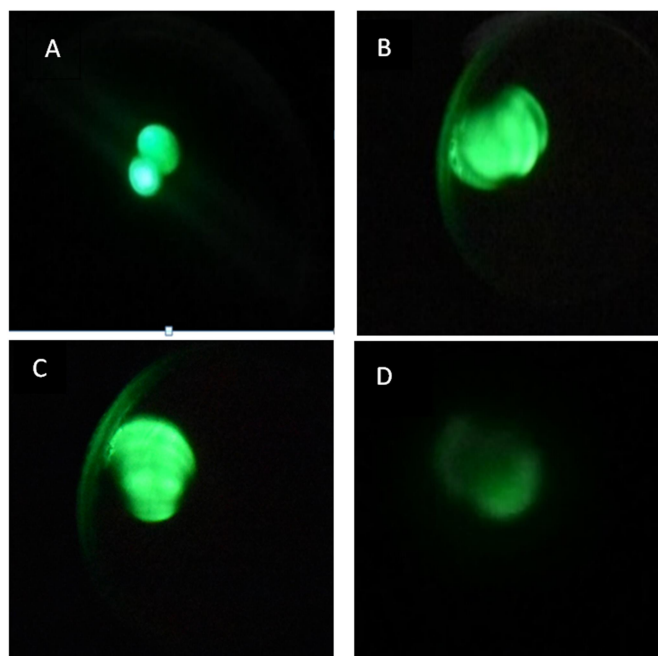


FIG. 3. Electron emission pattern for uncoated emitter type 1. A) Emission current 1.3 μA , applied voltage 1600 V. B) Emission current 0.8 μA , applied voltage 1400 V. C) Emission current 0.6 μA , applied voltage 1200 V. D) Emission current 0.4 μA , applied voltage 1100 V.

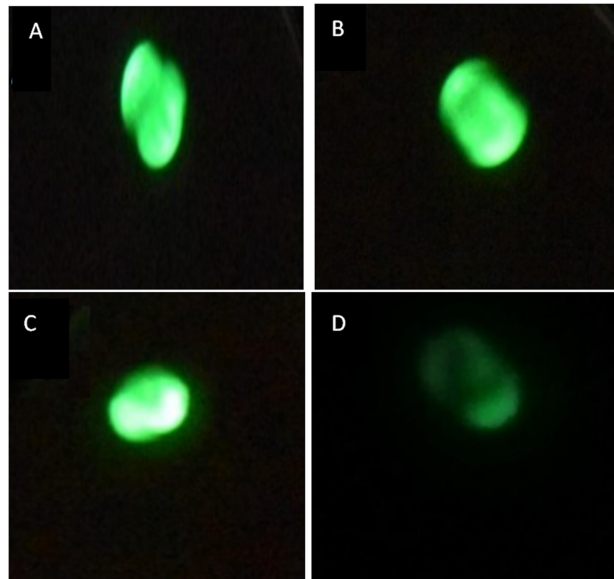


FIG. 4. Electron emission pattern for uncoated emitter type 2. A) Emission current $1.5 \mu\text{A}$, applied voltage 1600 V. B) Emission current $1.2 \mu\text{A}$, applied voltage 1400 V. C) Emission current $0.7 \mu\text{A}$, applied voltage 1200 V. D) Emission current $0.3 \mu\text{A}$, applied voltage 1100 V.

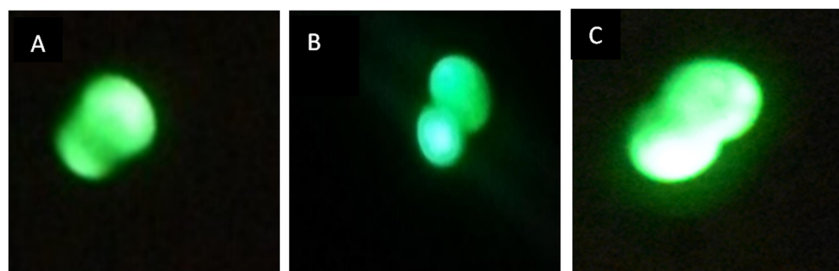


FIG. 5. The stability structure pattern for uncoated emitter type 1, at emission current $2 \mu\text{A}$, applied voltage 1900 V. The duration time between obtaining the next images is 15 minutes.

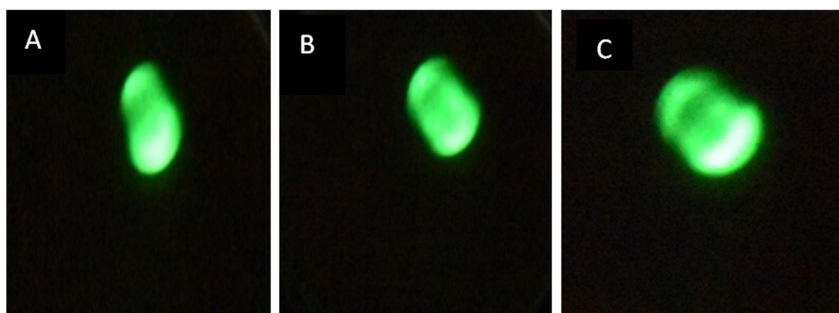


FIG. 6. The stability structure pattern for uncoated emitter type 2, at emission current $3 \mu\text{A}$, applied voltage 1900 V. The duration time between obtaining the next images is 15 minutes.

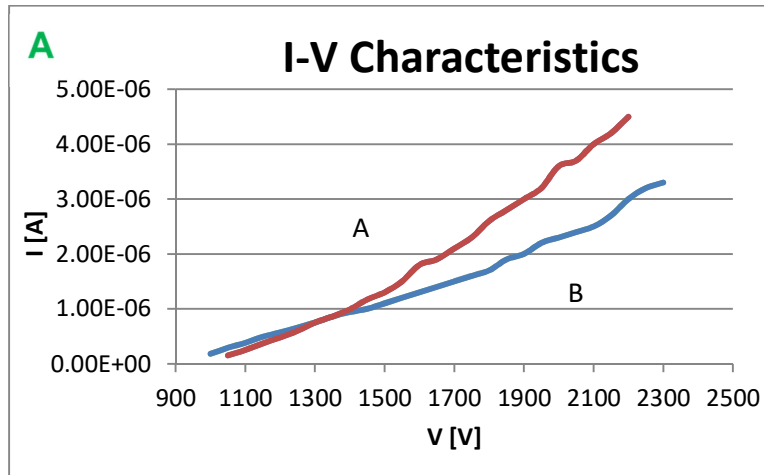


FIG. 7. A. I–V characteristics for uncoated emitters, curve A for uncoated W- emitter type 1 of tip radius 120 nm. Curve B for uncoated W- emitter type 2 of tip radius 110 nm.

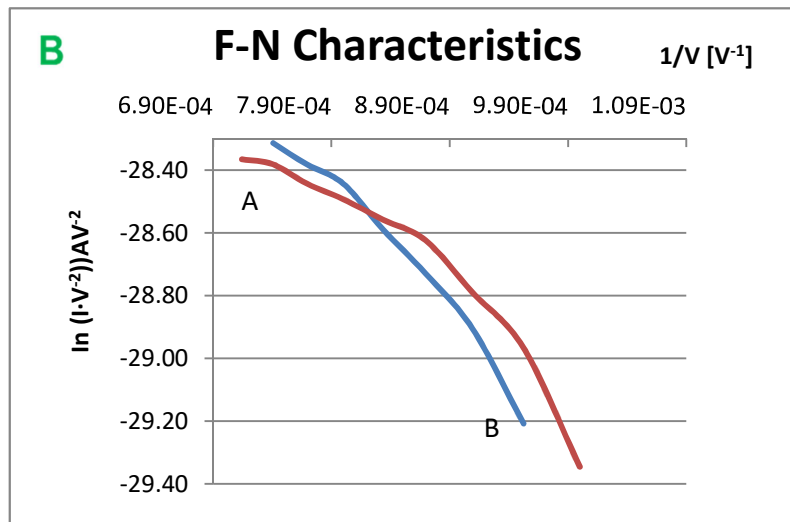


FIG. 7. B. F-N characteristics for uncoated W- emitters. Curve A for emitter type 1. Curve B for emitter type 2.

The comparison of similarity of slope for the emitters in the I-V and F-N plots (as shown in Fig. 7 A, B) shows the extent of similarity of the radius of the tips together. This has helped study the electron emission after coating the emitters with two various types of epoxy (UPR- 4 resin and Epoxylite 478 resin) under similar operational conditions, such as the thickness of the risen layer, the baking temperature and vacuum.

Fig. 8A shows the SEM image for emitter type 1 after being coated with Epoxylite UPR-4 resin, which has an approximately hemispherical apex. The tip radius was 120 nm and the Epoxylite UPR- 4 resin layer was uniformly distributed on a tip apex with a thickness of 60 nm. Fig. 8B shows the SEM image for emitter type 2 after being coated with Epoxylite 478

resin, which has an approximately hemispherical apex. The measurement radius was 110 nm and the Epoxylite 478 resin layer was uniformly distributed apex with a thickness of 60 nm. Fig. 9 shows the images for electron emission pattern for emitter type 1 after being coated with a 60-nm thick layer of Epoxylite UPR-4 resin, while Fig. 10 shows the images for electron emission pattern for emitter type 2 after being coated with a 60-nm thick layer of Epoxylite 478 resin. The images have been taken for the emission patterns at the switch-on voltage and when the voltage was regularly decreased. The FEM images primarily consist of a single bright spot for emitter type 1, as shown in Fig. 11. The FEM images primarily consist of a single bright spot for emitter type 2, as shown in Fig. 12.

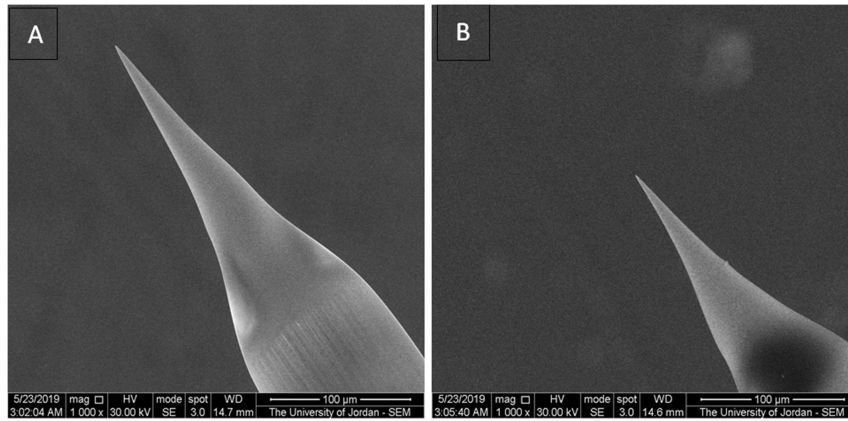


FIG. 8. A) SEM image at magnification (X 1000) for emitter type 1 after being coated with Epoxylite UPR- 4 resin. The measurement radius was 120 nm and the Epoxylite UPR- 4 resin layer was uniformly distributed tip apex with a thickness of 60 nm. B) SEM image at magnification (X 1000) for emitter type 2 after being coated with Epoxylite 478 resin. The measurement radius is 110 nm and the Epoxylite 478 resin layer was uniformly distributed tip apex with a thickness of 60 nm.

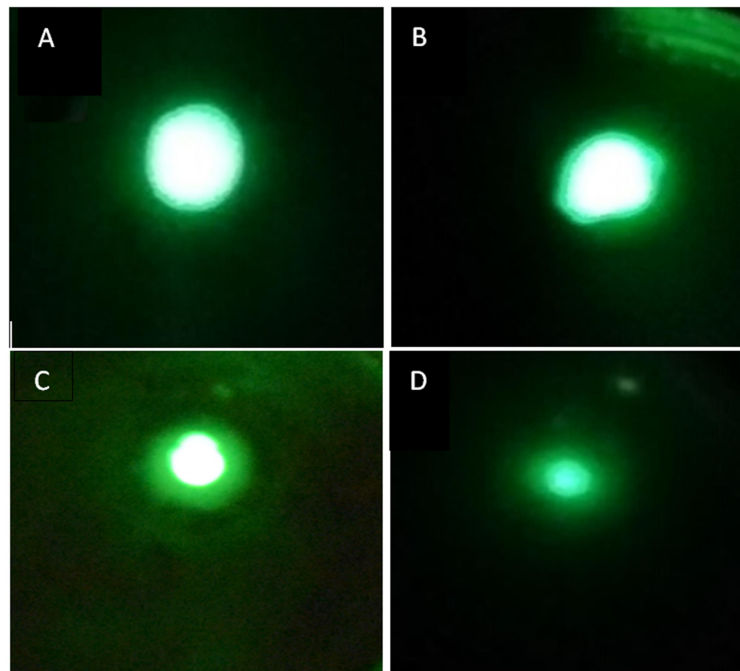


FIG. 9. Electron emission pattern for emitter type 1 after being coated with a 60-nm thick layer of Epoxylite UPR- 4 resin: A) emission current 2 μA , applied switch-on voltage 1250 V. B) emission current 1.7 μA , applied voltage 1150 V. C) emission current 1 μA , applied voltage 850 V. D) emission current 0.5 μA , applied voltage 650 V.

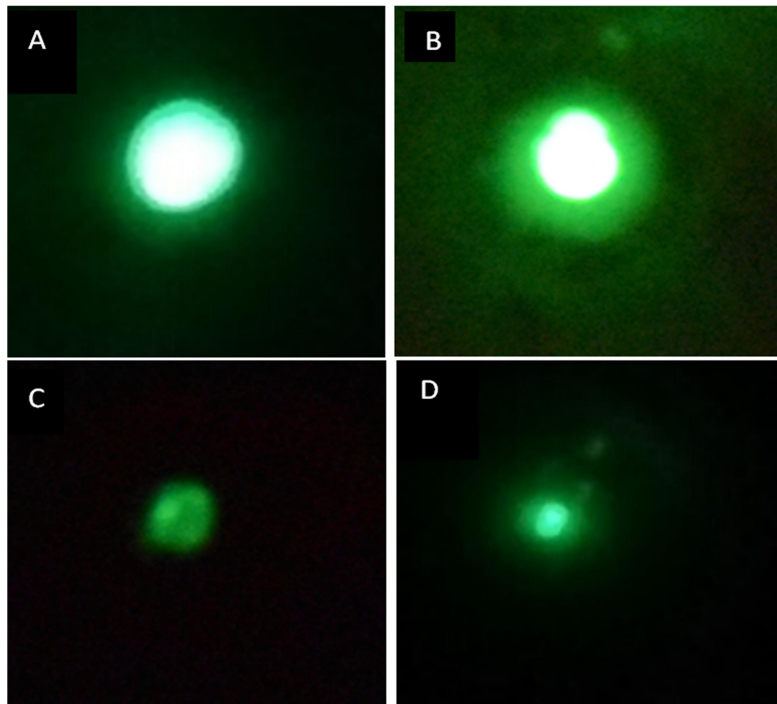


FIG. 10. Electron emission pattern for emitter type 1 after being coated with a 60-nm thick layer of Epoxylite 478 resin: A) emission current $2.3 \mu\text{A}$, applied switch-on voltage 1150 V. B) emission current $2 \mu\text{A}$, applied voltage 1050 V. C) emission current $1.8 \mu\text{A}$, applied voltage 800 V. D) emission current $0.5 \mu\text{A}$, applied voltage 650 V.

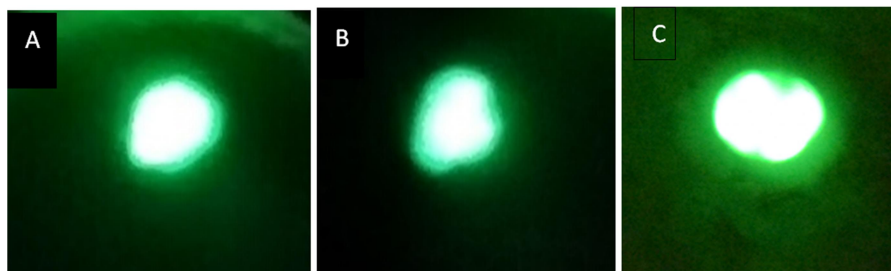


FIG. 11. The stability structure pattern for emitter type 1 after being coated with a 60-nm thick layer of Epoxylite UPR-4 resin at emission current $1.7 \mu\text{A}$ and applied voltage 1100 V. The duration time between obtaining images is 15 minutes.

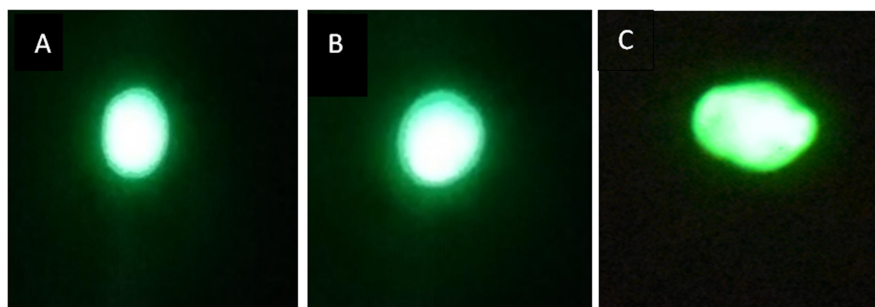


FIG. 12. The stability structure pattern for emitter type 2 after being coated with a 60-nm thick layer of Epoxylite 478 resin at emission current $2.2 \mu\text{A}$ and applied voltage 1100 V. The duration time between obtaining images is 15 minutes.

From the comparison of the emission current patterns, emission current stability structure patterns and SEM images showing the tip geometry and surface, it is concluded that emitter type 2 coated with a 60-nm thick layer of

Epoxylite 478 resin has a higher emission current and is more stable compared to emitter type 1 coated with a 60-nm thick layer of Epoxylite UPR-4 resin.

Fig. 13 shows I-V characteristics for the emitters being coated with an epoxy thin layer. For emitter type 1 coated with a 60-nm thick layer of Epoxylite UPR- 4 resin, the switch-on phenomenon occurs at $V_{SW} = 1250$ V and the emission current $I_{SW} = 3.2\mu\text{A}$, by decreasing the voltage of the line region of F-N plot that extends down to $V_{SAT} = 800$ V with an emission current $I_{SAT} = 1.12 \mu\text{A}$, by decreasing the voltage of the emission current that vanishes at $V_{TH} = 550$ V with an emission current $I_{TH} = 46.7$ PA.

For emitter type 2 coated with a 60-nm thick layer of Epoxylite 478 resin, the switch-on phenomenon occurs at $V_{SW} = 1150$ V and the emission current $I_{SW} = 3.3 \mu\text{A}$, by decreasing the voltage of the line region of F-N plot that extends down to $V_{SAT} = 600$ V, with an emission current $I_{SAT} = 1.08 \mu\text{A}$, by decreasing the voltage of the emission current that vanishes at $V_{TH} = 400$ V, with an emission current $I_{TH} = 22.3$ PA. The F-N plots for the two emitters after being coated are as shown in Fig. 14.

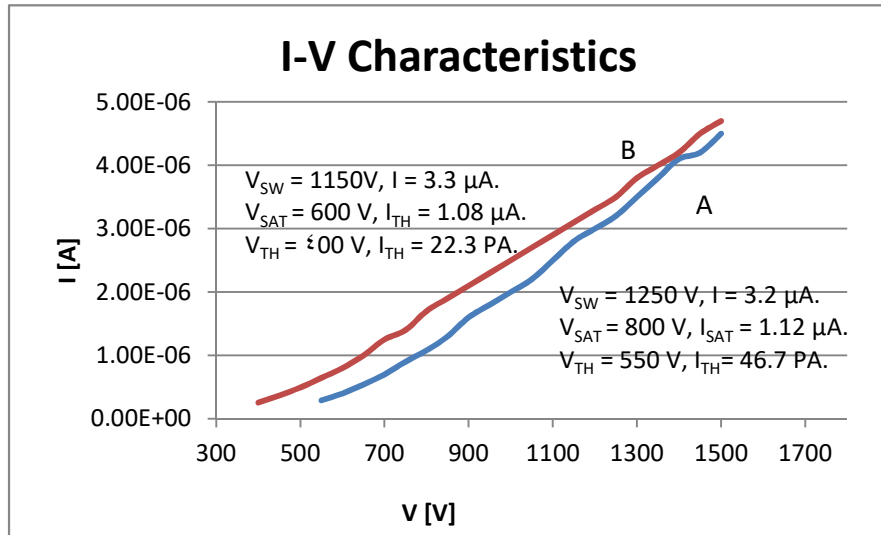


FIG. 13. Curve A is the I-V characteristics for emitter type 1 after being coated with a 60-nm thick layer of Epoxylite UPR- 4 resin. B) The I-V characteristics for emitter type 2 after being coated with a 60-nm thick layer of Epoxylite 478 resin.

From a practical point of view, the results highlighted that the switch-on voltage and threshold voltage for emitter type 2 were significantly lower than the switch-on voltage and threshold voltage for emitter type 1. Likewise, the emission current from emitter type

2 was greater than that from emitter type 1. Besides, based on the comparison of the F-N plots, it turns out that emitter type 2 leads to a decrease in the slope of these plots more than the decrease in the slope for emitter type 1 [2, 14].

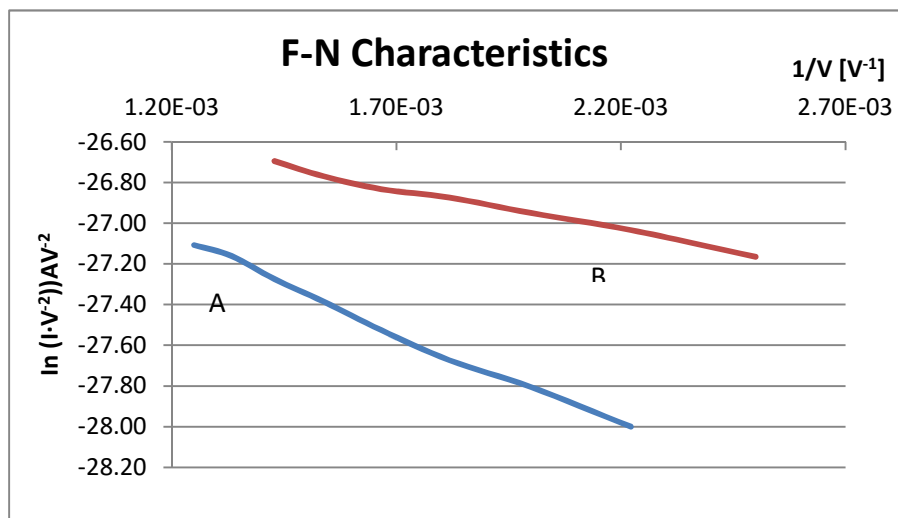


FIG. 14. Curve A shows the Fowler-Nordheim plots of emitter type 1(Epoxylite UPR- 4 resin). Curve B shows the Fowler-Nordheim plots of emitter type 2 (Epoxylite 478 resin).

Conclusion

In a nutshell, in composite emitters consisting of clean tungsten tips coated with various types of epoxy resins, the field emission characteristics of a tungsten electron source have been intrinsically changed by coating the tips with a thin layer of epoxy resins. This is in line with the results obtained from similar studies [2, 5, 15]. This change in characteristics varies depending on the type of epoxy resins used in coating the tungsten tips. More importantly, this is evident

by comparing the effects of epoxy resins used in this work (Epoxylite 478 resin and UPR-4 resin).

Acknowledgments

The authors would like to thank the Deanship of Academic Research at Mu'tah University for supporting this work through research project number 241/19/120.

The research infrastructure was funded by the Czech Academy of Sciences (project RVO: 68081731).

References

- [1] Forbes, R.G., Deane, J.H., Hamid, N. and Sim, H.S., *Journal of Vacuum Science & Technology*, 22 (2004) 1222.
- [2] Mousa, M.S., Latham, R.V., *Le Journal de Physique Colloques*, 47 (1986) 139.
- [3] Alnawasreh, S., Mousa, M.S. and Al-Rabadi, A.N., *Jordan J. Phys.*, 8 (2) (2015) 95.
- [4] Knápek, A., Sýkora, J., Chlumská, J. and Sobola, D., *Microelectronic Engineering*, 173 (2017) 42.
- [5] Sergeev, E., Knapek, A., Grmela, L. and Šikula, J., *International Conference on Noise and Fluctuations (ICNF)*, (2013) 1-4.
- [6] Al-Qudah, A.M., Mousa, M.S. and Fishcher, A., *IOP Conf. Series: Materials Science and Engineering*, 92 (2015) 12.
- [7] Al-Qudah, A.M. and Mousa, M.S., *Applied Microscopy*, 3 (2016) 30.
- [8] Latham, R.V. and Salim, M.A., *Journal of Physics E: Scientific Instruments*, 2 (1987) 181.
- [9] Meza, J.M., Lubin, C., Thoyer, F., Rosales, K.V., Espinoza, A.G., Martin, F. and Cousty J., *Carbon*, 8 (2015) 363.
- [10] Madanat, M.A., Mousa, M.S., Al-Rabadi, A.N. and Fischer, A., *Jordan J. Phys.*, 8 (2) (2015) 79.
- [11] Zhou, W., Wang, Z.L., Eds., "Scanning Microscopy for Nanotechnology", (Springer, 2007).
- [12] FEI Company, "An Introduction to Electron Microscopy", (2010).
- [13] Mousa, M.S., *Surface and Interface Analysis*, 39 (2007) 102.
- [14] Mayer, A., Mousa, M.S. and Vigneron, J.P., *Ultramicroscopy*, 89 (2001) 95.
- [15] Al-Qudah, A.M., Alnawasreh, S.S., Madanat, M.A., Trzaska, O., Matykiewicz, D., Alrawshdeh, S.S., Haggmann, M.J. and Mousa, M.S., *Jordan J. Phys.*, 11 (1) (2018) 59.

Electrical Properties in Large Frequency and Temperature Ranges of $\text{Sr}_{0.6}\text{Ca}_{0.4}\text{TiO}_3$ Ceramics

H. Ait Laasri^{a,b}, A. Tachafine^a, D. Fasquelle^a, N. Tentillier^a,
M. Elaatmani^b, L. C. Costa^c and J. -C. Carru^a

^a *Unité de Dynamique et Structure des Matériaux Moléculaires, Université du Littoral - Côte d'Opale, 50 rue Ferdinand Buisson, 62228 Calais, France.*

^b *Unité de Dynamique et Structure des Matériaux Moléculaires, Université du Littoral - Côte d'Opale, 50 rue Ferdinand Buisson, 62228 Calais, France.*

^c *13N and Physics Department, University of Aveiro, Campus Universitário de Santiago 3810-193 Aveiro, Portugal.*

Doi : <https://doi.org/10.47011/13.3.3>

Received on: 08/08/2019;

Accepted on: 12/12/2019

Abstract: Lead-free $\text{Sr}_{0.6}\text{Ca}_{0.4}\text{TiO}_3$ (SCT) ceramic was prepared by the solid state reaction route. X-Ray diffraction technique showed the phase purity and identified the orthorhombic perovskite structure of the material. Scanning Electronic Microscopy observation evidenced homogeneous morphology and dense microstructure for the ceramic. The dielectric and conductivity properties of the sample were studied using complex impedance measurement technique in a wide range of frequencies and temperatures: from 100 Hz to 1.8 GHz and from 25°C to 550°C. The ceramic exhibits a stable dielectric permittivity and low dielectric losses in frequency and temperature up to 200°C. This is very interesting in view of developing high-quality lead-free ceramic capacitors for applications requiring high temperatures; for example, in cars. The increase in dielectric permittivity for temperatures higher than 200°C may be related to oxygen vacancies that are heat-activated in the material. Dielectric losses show the existence of a dielectric relaxation at low temperatures and low frequencies. Conductivity measurement investigated at high temperatures show on one hand high AC conductivity values attributed to the high temperature jumping process and on the other hand two electrical conductivity mechanisms above 400° C in the material.

Keywords: Strontium calcium titanate, Ceramic, Structure, Dielectric properties, Conductivity.

Introduction

Due to the multiplication of standards and norms of telecommunication systems and in the era of miniaturization, an important need for frequency tunable components and multifunctional devices appears [1-4]. Many solutions can be considered, among which is the introduction of new materials and/or new structures able to modify the properties of the

devices constituted thereof. In order to do so, we must use materials presenting low losses and high dielectric permittivity stable in frequency and temperature [5]. Most electronic components contain lead-based materials, because of their interesting electric and ferroelectric properties. Among them are pure PbTiO_3 or doped $(\text{Pb,Zr})\text{TiO}_3$ [6-7]. For environmental reasons, as

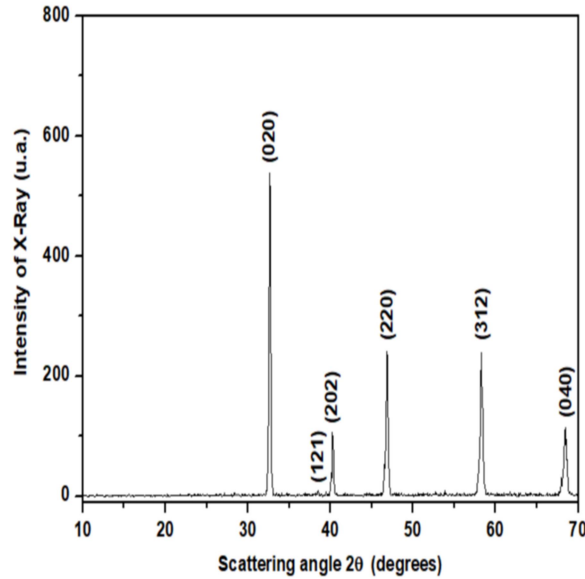
evidenced by the legislation passed by the European Union in this effect [8-9], all research turned toward the environment-friendly materials. It is now necessary to replace Pb-based materials with lead-free materials [10]. Barium titanate (BaTiO_3) material has good dielectric properties which make it the most used base material to elaborate high dielectric permittivity capacitors [11]. However, the variations of its dielectric permittivity with temperature are too important for practical applications [12]. The strontium titanate (SrTiO_3), which is another simple perovskite ABO_3 ferroelectric material, displays a paraelectric behavior with cubic symmetry at room temperature [13]. Additionally, this material presents high dielectric permittivity and low dielectric losses at high frequency [14], which gives advantages for electrical applications. To improve the electrical properties of SrTiO_3 ceramics, it is possible to substitute A-sites with another divalent cation, such as Ba^{2+} , Mg^{2+} , Ce^{2+} or Ca^{2+} [15-20]. In particular, the $\text{Sr}_{1-x}\text{Ca}_x\text{TiO}_3$ solid solution undergoes phase transition and exhibits different structures and behaviors, depending on the composition of calcium. It shows a ferroelectric behavior for the composition range $0.0018 < x \leq 0.016$, a relaxor one for $0.016 < x \leq 0.12$ and an anti-ferroelectric one for $0.12 < x \leq 0.4$ such as for example around 185 K for $x=0.25$ [21-22]. Recent studies conducted at low frequencies have shown that it is possible to increase the dielectric constant value of the SrTiO_3 ceramic by doping with low calcium rates from 2% to 4% [23] or decreasing it for rates higher than 12% [24]. In the present work, we report on the structural and dielectric properties of strontium calcium titanate ($\text{Sr}_{1-x}\text{Ca}_x\text{TiO}_3$) ceramics in which strontium is substituted by a high rate of calcium, which is 40% to obtain lead-free ferroelectric materials with improved properties for electronic radiofrequencies and microwave applications. In fact, the lowest losses have been measured on high rates of calcium [25-26]. We have studied this bulk material both at room temperature in a large frequency range from 100 Hz to 1.8 GHz and in a large temperature range from room temperature to 510°C to evaluate its possible use in high-temperature and/or high-frequency environments. The measurement of complex impedance spectroscopy was used for dielectric characterization.

Experimental

Ceramic samples with 3 mm of diameter and 3 mm of thickness were prepared by the conventional solid-state reaction method. $\text{Sr}_{0.6}\text{Ca}_{0.4}\text{TiO}_3$ samples (SCT) were prepared using stoichiometric proportions of high-purity powders of strontium carbonate (SrCO_3) (Fluka, 98%), calcium carbonate (CaCO_3) (Fluka, 98%), and titanium oxide (TiO_2) (Prolabo, 99%). Appropriate quantities of these precursors were then weighed, thoroughly mixed and pestled in an agate mortar and subsequently calcined at 1250°C in alumina crucibles under an air atmosphere for 15 hours. After cooling, the obtained powder was ground and then pressed under a load of 0.5 ton into pellets of 3-mm diameter and 3-mm thickness. The pellets were subsequently sintered at 1400°C for 5 hours in air. X-ray diffraction (XRD) analysis was performed at room temperature on the powdered samples, in a Philips X'PERT system, with a $\text{K}\alpha$ radiation ($\lambda=1.54056 \text{ \AA}$) at 40 kV and 30 mA, with a step of 0.05° and a time per step of 1 second. Microstructures were examined by Scanning Electronic Microscopy (SEM). Silver-paint electrodes were deposited on the samples for electrical measurements. Temperature and frequency dependences of the dielectric permittivity and loss-tangent of the ceramics were investigated from 80 K to 800 K and from 20 Hz to 1 MHz using an Agilent 4284A LCR meter.

Results and Discussion

Fig. 1 shows the XRD patterns of the SCT powder at room temperature. All the peaks of the XRD diagrams were indexed to the pure perovskite phase. The peaks are intense and very narrow, showing good crystallinity of the samples. No peaks were detected which could be assigned to secondary phases or unreacted oxides. The observed peaks are characteristic of an orthorhombic structure [22] according to International Center Diffraction Data (ICDD) files Ref. 01-089-8032. The lattice parameters are calculated using the unit-cell refinement software Celref [27]. The (a, b, c) dimensions and unit cell volume values are respectively: 5.4960 \AA , 5.4881 \AA , 7.7418 \AA and 233.51 \AA^3 . The average crystallite size calculated by the Scherrer's Eq. (1) is about 42 nm.

FIG. 1. XRD patterns of Sr_{0.6}Ca_{0.4}TiO₃ powders.

$$D = \frac{k\lambda}{\beta \cos \theta} ; \text{ where:} \quad (1)$$

β : Peak width at half maximum height (FWHM) (rad);

θ : Bragg diffraction angle;

λ : X-ray wavelength (1.5406 Å);

k : Dimensionless shape factor (0.9).

Fig. 2 shows the SEM microphotograph of the SCT ceramic. The microphotograph shows a homogeneous microstructure and well-developed grain morphologies. The average grain size is estimated using the MagniSci software and is about 2 μm which is about 45 times the average crystallite size. The average grain boundary size is about 0.05 μm . The compactness of the SCT ceramic is about 93%.

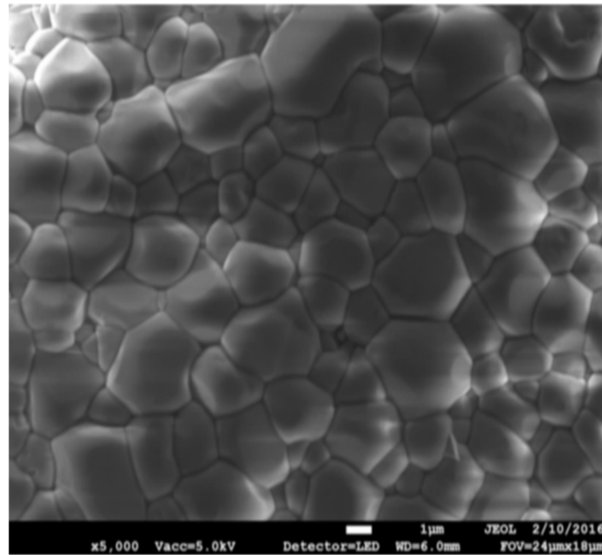
FIG. 2. SEM microphotograph of the Sr_{0.6}Ca_{0.4}TiO₃ ceramic.

Fig. 3 presents the frequency dependence of the dielectric permittivity ϵ' of SCT ceramic from 100 Hz to 1 GHz at room temperature. The dielectric permittivity shows a good stability all over the frequency range ($\epsilon' \approx 200$). This is an advantage for high-frequency components. This

ϵ' value is lower than that reported for low calcium rates ($x = 0.02$ and $\epsilon' \approx 310$) [23]. In fact, doping with Ca rates higher than 12% decreases the dielectric permittivity value, as shown in recent studies [24].

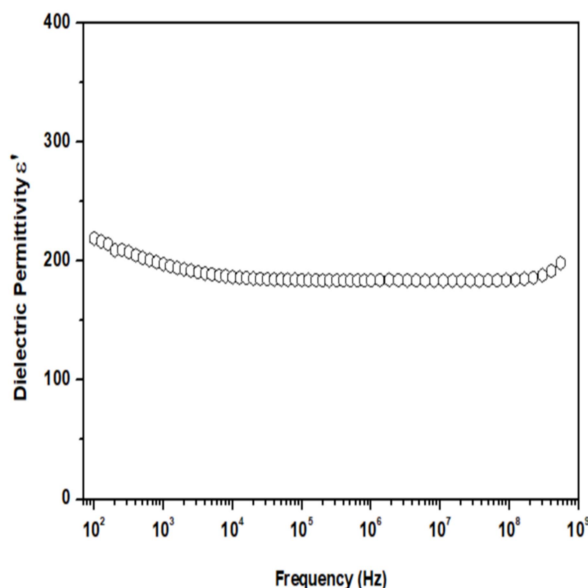


FIG. 3. Dielectric permittivity (ϵ') of the $\text{Sr}_{0.6}\text{Ca}_{0.4}\text{TiO}_3$ ceramic in frequency at room temperature.

The frequency dependence of the dielectric loss tangent ($\text{tg}\delta$) of SCT ceramic from 100 Hz to 1 GHz at room temperature is shown in Fig. 4. The dielectric loss tangent decreases from 100 Hz to 1 MHz down to $3 \cdot 10^{-4}$ due to space-charge polarization losses and increases from 10 MHz to 1 GHz up to $6 \cdot 10^{-2}$ due to intrinsic losses [28]. These $\text{tg}\delta$ values are of interest for

radiofrequency and microwave applications, especially as the dielectric permittivity of the ceramic is stable over the whole frequency range. It was not possible to collect accurate data from 1 MHz to 12 MHz, because the pellet resistance was too high and definitely out of the measurement range for the HP4291A.

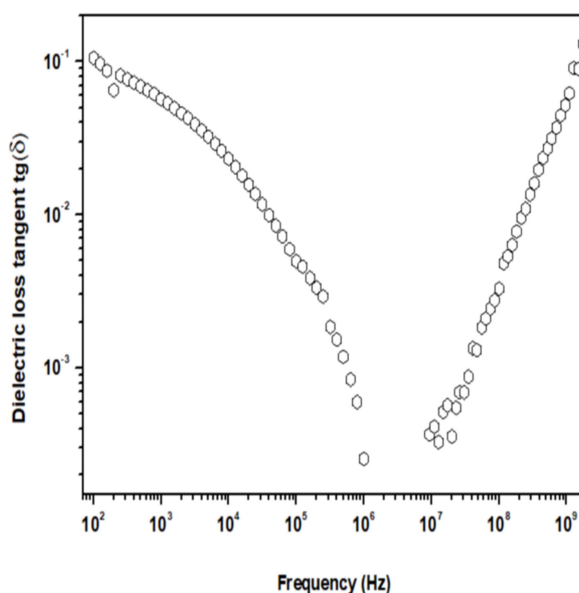


FIG. 4. Dielectric loss tangent ($\text{tg}\delta$) of the $\text{Sr}_{0.6}\text{Ca}_{0.4}\text{TiO}_3$ ceramic in frequency at room temperature.

Fig. 5 shows the temperature dependence of the dielectric permittivity of SCT ceramic from room temperature to 510°C at different frequencies from 100 Hz to 1 MHz. The dielectric permittivity is constant ($\epsilon' = 200$) in temperature up to 200°C for all the frequencies

and no phase transition is observed. This stability of the dielectric permittivity in frequency and temperature up to 200°C is very interesting and shows that SCT could be used in ceramic capacitors applied to high-temperature environments, such as the automotive or military

field for example [29]. The dielectric permittivity is stable over a temperature range which is all the more so as the frequency increases. Indeed, it is almost stable from room temperature to about 300°C for $f = 1$ kHz, to about 375°C for $f = 10$ kHz and above 500°C for $f = 1$ MHz. For each temperature, there is therefore a threshold frequency F_T , since at this frequency, the dielectric permittivity starts to rise at this temperature. It can be noted that above 450°C , a peak can be seen clearly for example at

1 GHz and about 500°C with $\epsilon' \approx 4000$. Its origin may be a relaxation, but more probably an extrinsic effect of Maxwell-Wagner interfacial polarization between the grains (semiconductors) and the grain boundaries (electrical insulators). The maximal amplitude of the peak decreases as the measurement frequency increases. At a given ϵ' , for example 1000 , it is observed that the frequency increases as the temperature increases, which means that the Maxwell-Wagner polarization is thermally activated [30].

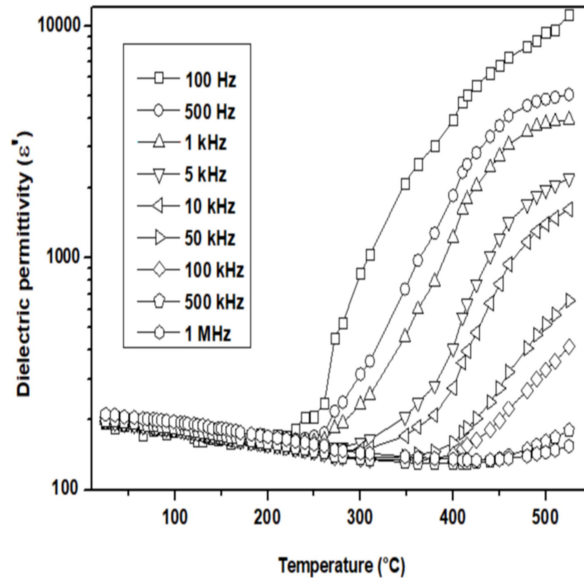


FIG. 5. Dielectric permittivity (ϵ') of the $\text{Sr}_{0.6}\text{Ca}_{0.4}\text{TiO}_3$ ceramic in frequency and temperature.

The temperature dependence of the threshold frequency is shown in Fig. 6. The threshold frequency increases with increasing temperature. The calculated activation energy (1.74 eV)

shows that the increase in dielectric permittivity with temperature may be related to oxygen vacancies that are heat-activated in the material [31].

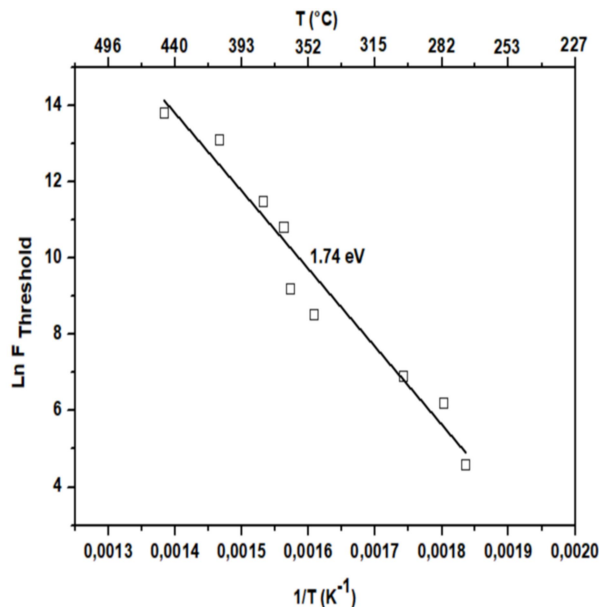


FIG. 6. Threshold frequency (F_T) of the $\text{Sr}_{0.6}\text{Ca}_{0.4}\text{TiO}_3$ ceramic in temperature.

The temperature dependence of the dielectric losses of SCT ceramic from room temperature to 510°C at different frequencies from 100 Hz to 1 MHz (Fig. 7) shows that the dielectric losses remain smaller than 10 up to 200°C from 100 Hz to 1 MHz. The minimum ϵ'' value obtained is 10^{-2} at 10 kHz and 100°C. These low values are very interesting for the development of high-quality factor lead-free ceramic capacitors for applications requiring high temperatures. For frequencies lower than 1 MHz, ϵ'' shows a

minimum around 100°C, which could indicate the existence of dielectric relaxation at low temperatures and low frequencies. Fig. 4 illustrates $\text{tg}\delta$ as a function of frequency. The sharp increase in dielectric losses above about 200°C may be attributed to impurities and thermally activated charge carriers and possible high electrical conductivity at these temperatures in the material [32].

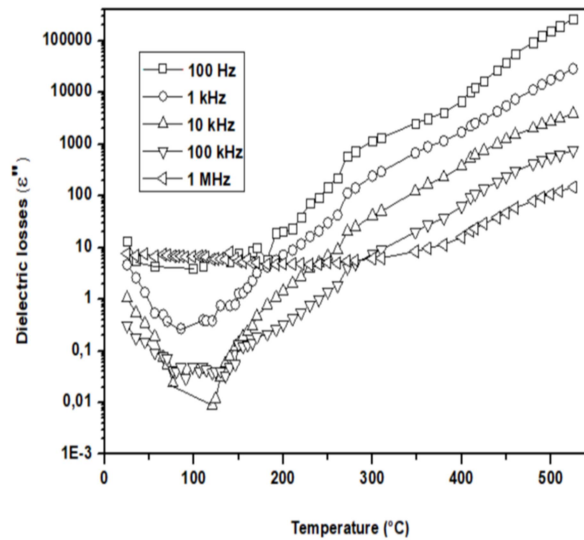


FIG. 7: Dielectric losses (ϵ'') of the $\text{Sr}_{0.6}\text{Ca}_{0.4}\text{TiO}_3$ ceramic in frequency and temperature.

Fig. 8 presents the frequency dependences of dielectric permittivity and dielectric losses at 450°C from 100 Hz to 1 MHz. The dielectric permittivity ϵ' decreases significantly as the measuring frequency increases. This is due to charging mechanisms at the electrodes [33]. Indeed, at low frequencies, ions have enough time to accumulate at the interface of the conductive regions, but at high frequency, they

cannot accumulate at the interface and therefore cannot be polarized. Dielectric losses ϵ'' decrease as the measurement frequency increases, like ϵ' . This frequency effect at high temperature on dielectric losses is attributed to the formation of a space charge region at the electrode-sample interface (contribution on ϵ'), explained in terms of oxygen vacancies diffusion [34].

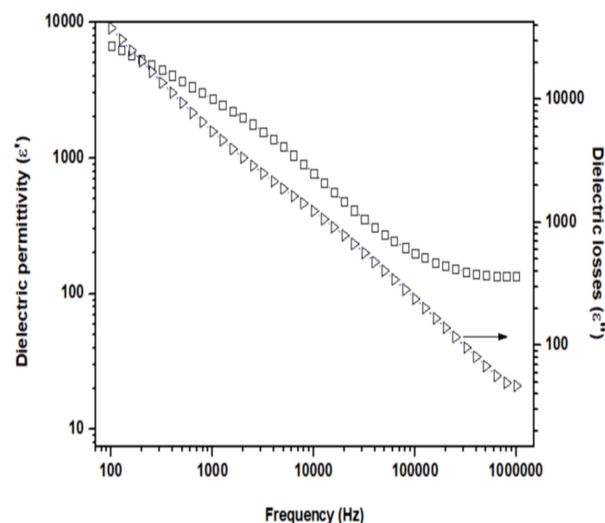


FIG. 8: Dielectric permittivity (ϵ') and dielectric losses (ϵ'') of the $\text{Sr}_{0.6}\text{Ca}_{0.4}\text{TiO}_3$ ceramic in frequency at 450°C.

Electrical conductivity makes it possible to explain the phenomenon of ion transport in the material. The real part of the electrical conductivity σ' of a material is given by the formula: $\sigma' = \omega \cdot \epsilon_0 \cdot \epsilon''$

According to Jonscher, the origin of the evolution of the conductivity as a function of frequency is due to ionic relaxation in the material [35]. The temperature dependence of

the conductivity of the SCT ceramic is shown in Fig. 9, from room temperature to 510°C and at different frequencies from 100 Hz to 1 MHz. At a given frequency, the conductivity has the same temperature-dependent appearance as the dielectric losses (Fig. 7), which shows that the dielectric losses are also due to the electrical conductivity in the material.

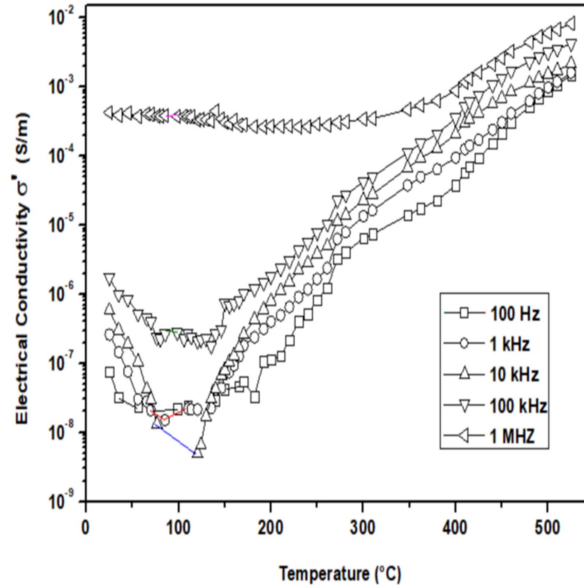


FIG. 9. Conductivity (σ') of the $\text{Sr}_{0.6}\text{Ca}_{0.4}\text{TiO}_3$ ceramic in frequency and temperature.

Fig. 10 shows the Arrhenius plots of $\ln \sigma'$ versus $1/T$ for the ceramic at different frequencies: from 100 Hz to 1 MHz. The conductivity σ' increases strongly with temperature from 127°C for frequencies between 100 Hz and 100 kHz and from 400°C for 1 MHz.

This variation is attributed to the charge carriers hopping due to the high temperature jumping process [36]. At 1 MHz, σ' is constant up to 300°C with a value of about 3×10^{-4} S/m. Above 400°C , the conductivity is thermally activated with the Arrhenius formula (2).

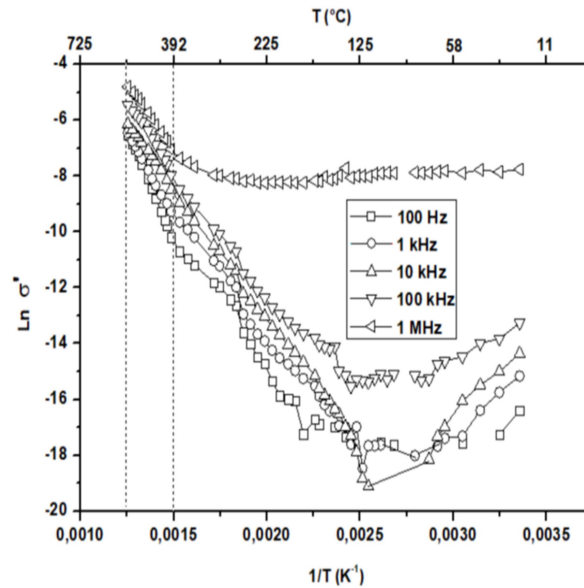


FIG. 10. Conductivity (σ') of the $\text{Sr}_{0.6}\text{Ca}_{0.4}\text{TiO}_3$ ceramic in frequency and temperature.

$$\sigma_{AC} = \sigma_0 e^{\frac{-E_a}{k_B T}} \quad (2)$$

Fig. 11 shows the Arrhenius plots of $\ln \sigma'$ from 400°C to 510°C and at different frequencies from 100 Hz to 1 MHz. The calculated activation energy E_a decreases with the increase of frequency: from 1.38 eV at 100 Hz to 0.86 eV at 5 kHz. For frequencies higher than 5 kHz, the activation energy increases

slightly until 0.93 eV at 100 kHz and then decreases to 0.84 eV at 1 MHz. The activation energy is due to the movement of the charge carriers and to jumps of oxygen vacancies as well as to structural defects at high temperatures [36-37]. The values obtained show that the activation energy is due to the clustering and dissociating processes of the oxygen vacancies [38].

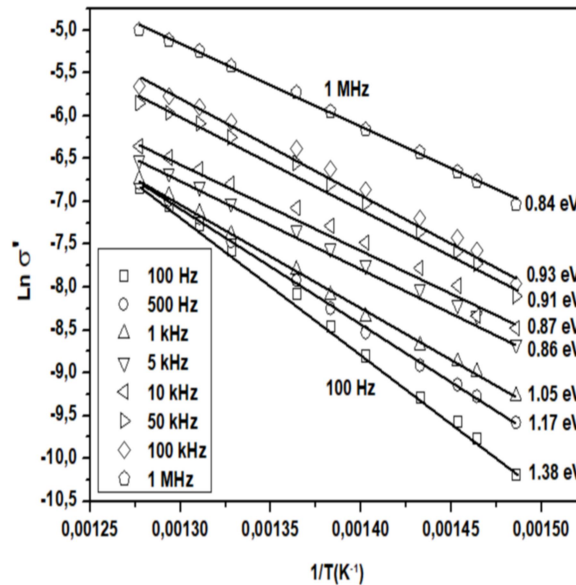


FIG. 11. Arrhenius plots of the conductivity of the $\text{Sr}_{0.6}\text{Ca}_{0.4}\text{TiO}_3$ ceramic from 400°C to 510°C given for frequencies ranging from 100 Hz to 1 MHz.

Fig. 12 shows the frequency dependence from 100 Hz to 1 MHz of the conductivity activation energy E_a . All E_a values have been extracted from Fig. 11, where the temperature ranges from 400°C to 510°C. This curve shows two distinct regions: The first in low frequency from 100 Hz to 5 kHz and the second in medium frequency from 5 kHz to 1 MHz. In the first region, the activation energy decreases significantly with the increase of frequency, while in the second, it increases slightly. The low frequency region could first concern continuous conductivity and then grain boundaries. In fact, at low frequency, the continuous conductivity is sensitive to long-range ion transport usually determined by much higher activation energies [39]. In addition, in grain boundaries, the activation energy is higher

than that in grains due to potential barriers in grain boundaries. The second region could mainly concern oxygen vacancies in the ceramic grains. The activation energy is lower in this region due to short-range ordering of oxygen vacancies [40]. The respective contributions of grains and grain boundaries to the electrical conductivity of the ceramic, at low frequency for grain boundaries and at high frequency for grains, are proven by complex impedance measurement results obtained otherwise [41]. The slight increase in activation energy at high frequency may be due to the creation of charge carriers, such as the formation of doubly-ionized oxygen vacancies [36, 42-47].

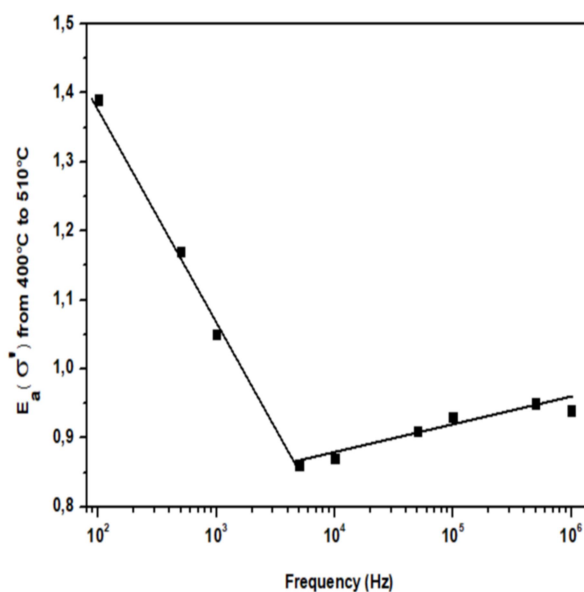


FIG. 12. Conductivity activation energy (E_a) of the Sr_{0.6}Ca_{0.4}TiO₃ ceramic as a function of frequency. All E_a values are related to temperatures ranging from 400 to 510°C.

Conclusion

Sr_{0.6}Ca_{0.4}TiO₃ ceramic was prepared using the solid-state reaction route. XRD analysis revealed an orthorhombic perovskite structure of the material. The ceramic presents homogeneous morphology and dense microstructure. The ceramic exhibits stable dielectric permittivity and low dielectric losses in a wide frequency range from 100 Hz to 1.8 GHz and at temperatures up to 200°C, which shows that the ceramic is a good candidate for the development of monolithic ceramic capacitors dedicated to

high-frequency lead-free components and/or to extremely high-temperature environments. Increasing the temperature beyond 200°C resulted in an increase of the oxygen vacancy concentration and thermally activated charge carriers, which led to an increase of both the dielectric permittivity and dielectric losses. The evolution of the conductivity activation energy as a function of frequency above 400°C can be linked to the existence of two conduction mechanisms in the material.

References

- [1] Outzourhit, A. and Trefny, J.U., *J. Mater. Res. Soc.*, 10 (1995) 1411.
- [2] Jeon, J.H., *J. Eur. Ceram. Soc.*, 24 (2004) 1045.
- [3] Burgnies, L., Vélú, G., Blary, K., Carru, J.-C. and Lippens, D., *Electronic Letters*, 43 (21) (2007) 1151.
- [4] Wu, L., Chen, Y.-C., Chen, L.-J., Chou, Y.-P. and Tsai, Y.-T., *Jpn. J. Appl. Phys.*, 38 (1999) 5612.
- [5] Jacob, M.V., *Int. J. Mod. Phys. B*, 23 (2009) 3649.
- [6] Gonçalves, M.D. et al., *Ceram. Int.*, 42 (2016) 14423.
- [7] Aboubaker, S. et al., *Int. J. Hydrog. Energy*, 42 (2017) 19504.
- [8] Panda, P.K., *J. Mater. Sci.*, 44 (2009) 5049.
- [9] Guo, H., Shimizu, H. and Randall, C.A., *J. Appl. Phys.*, 118 (2015) 174107.
- [10] Puli, V.S. et al., *J. Phys. Chem. Solids*, 74 (2013) 466.
- [11] Cross, L.E., *Mater. Chem. Phys.*, 43 (1996) 108.
- [12] Reymond, V., PhD Thesis, Université de Bordeaux I (2004), France.
- [13] Wang, Z., Cao, M., Song, Z., Li, G., Hu, W., Hao, H. and Liu, H., *Ceram. Int.*, 40 (9) (A) (2014) 14127.

- [14] Xie, J. et al., *Ceram. Int.*, 42 (2016) 12796.
- [15] Wang, R., Inaguma, Y. and Itoh, M., *Mater. Res. Bull.*, 36 (2001) 1693.
- [16] Tkach, A., Vilarinho, P.M. and Kholkin, A., *Appl. Phys. A*, 79 (2004) 2013.
- [17] Ranson, P. et al., *J. Raman Spectrosc.*, 36 (2005) 898.
- [18] Zhanga, L., Yaoa, Z., Lanaganc, M.T., Haoa, H., Xiea, J., Xua, Q., Yuan, M., Sarkarat, M., Caoa, M. and Liua, H., *Journal of the European Ceramic Society*, 38 (2018) 2534.
- [19] Qi, J., Cao, M., Chen, Y., He, Z., Tao, C., Hao, H., Yao, Z. and Liu, H., *Journal of Alloys and Compounds*, 772 (2019) 1105.
- [20] Zhang, L., Hao, H., Zhang, S., Lanagan, M.T., Yao, Z., Xu, Q., Xie, J., Zhou, J., Cao, M. and Liu, H., *Journal of the European Ceramic Society*, 100 (2017) 4638.
- [21] Mishra, S.K., Ranjan, R. and Pandey, D., *J. Appl. Phys.*, 91 (7) (2002) 4447.
- [22] Anwar, S. and Lalla, N.P., *J. Solid State Chem.*, 181 (2008) 997.
- [23] Zhang, G.F. et al., *J. Mater. Sci. Mater. Electron.*, 26 (2015) 2726.
- [24] Ranjan, R. and Pandey, D., *J. Phys.: Condens. Mater.*, 13 (2001) 423.
- [25] Anwar, S. and Lalla, N.P., *Appl. Phys. Lett.*, 92 (2008) 212901.
- [26] Duan, S. et al., *J. Mater. Sci. Mater. Electron.*, 27 (2016) 6318.
- [27] <http://www.ccp14.ac.uk/tutorial/lmgp/celref.htm>
- [28] Tagantsev, A.K., Sherman, V.O., Astafiev, K.F., Venkatesh, J. and Setter, N., *Journal of Electroceramics*, 11 (2003) 5.
- [29] Ait Laasri, H., Fasquelle, D., Tachafine, A., Tentillier, N., Costa, L.C., Elaati, M., Outzourhit, A. and Carru J.-C., *Functional Materials Letters*, 11 (5) (2018) 1850005.
- [30] Maxwell, J., "A Treatise on Electricity and Magnetism". (Cambridge University Press, 1873).
- [31] Ang, C. and Yu, Z., *Phys. Rev. B*, 62 (2000) 228.
- [32] Sahoo, S., Mahapatra, P.K., Choudhary, R.N.P. and Nandagoswamy, M.L., *J. Mater. Sci.: Mater. Electron.*, 26 (2015) 6572.
- [33] Om, P.N. et al., *Indian. J. Pure Appl. Phys.*, 48 (2010) 57.
- [34] Mariappan, C.R. and Govindaraj, G., *Mater. Sci. Eng., B*, 94 (2002) 82.
- [35] Dhak, P., Dhak, D., Das, M. and Pramanik, P., *J. Mater. Sci.: Mater. Electron.*, 22 (2011) 1750.
- [36] Liu, L., Huang, Y., Su, C., Fang, L., Wu, M., Hu, C. and Fan, H., *Appl. Phys. A*, 104 (2011) 1047.
- [37] Rout, J., Parida, B.N., Das, P.R. and Choudhary, R.N.P., *J. Electron. Mater.*, 43 (2014) 732.
- [38] Wang, C.C., Lei, C.M., Wang, G.J., Sun, X.H., Li, T., Huang, S.G., Wang, H. and Li, Y.D., *J. Appl. Phys.*, 113 (2013) 094103.
- [39] Dunst, A., Epp, V., Hanzu, I., Freunberger, S.A. and Wilkening, M., *Energy Environ. Sci.*, 7 (2014) 2739.
- [40] McCammon, C.A., Becerro, A.I., Langenhorst, F., Angel, R.J., Marion, S. and Seifert, S., *J. Phys.: Condens. Matter*, 12 (2000) 2969.
- [41] Tachafine, A., Ait Laasri, H., Carru, J.C. and Fasquelle, D., to be published.
- [42] Verdier, C., Morrison, F.D., Lupascu, D.C. and Scott, J.F., *J. Appl. Phys.*, 97 (2005) 024107.
- [43] Yoo, H.I., Song, C.R. and Lee, D.K., *J. Electroceram.*, 8 (2002) 5.
- [44] Smyth, D.M., *J. Electroceram.*, 11 (2003) 89.
- [45] Moos, R., Menesklou, W. and Härdtl, K.H., *Appl. Phys. A*, 61 (1995) 389.
- [46] Moos, R. and Härdtl, K.H., *J. Appl. Phys.*, 80 (1996) 393.
- [47] Maglione, M. and Belkaoui, M., *Phys. Rev. B*, 45 (1992) 202.

Microstructure and Dielectric Properties of BaFe₁₂O₁₉ Hexaferrite Nanoparticles: Effect of Cobalt Addition and Calcination Temperature

H. Shehabi^a, M. Rekyb^b, R. Sayed Hassan^c and R. Awad^a

^a Department of Physics, Faculty of Science, Beirut Arab University, Beirut, Lebanon.

^b Department of Physics, Faculty of Science, Alexandria University, Alexandria, Egypt.

^b Department of Physics, Faculty of Science, Lebanese University, Beirut, Lebanon.

Doi : <https://doi.org/10.47011/13.3.4>

Received on: 08/08/2019;

Accepted on: 12/1/2020

Abstract: M-type Barium Hexaferrite (BaFe₁₂O₁₉) is a promising compound for technological applications because of its high permeability, high saturation magnetization and excellent dielectric properties. In this study, the microstructure and dielectric properties of Co_xBaFe₁₂O₁₉ Hexaferrite were investigated. The co-precipitation method was employed to prepare Co_xBaFe₁₂O₁₉ nanoparticles, with x = 0, 0.04, 0.06 and 0.1 wt. %, at two different calcination temperatures (900°C and 950°C). The microstructure of the samples was examined through X-ray powder diffraction (XRD) and transmission electron microscopy (TEM). The hexagonal structure of the prepared samples was confirmed from XRD results. TEM images reveal the formation of agglomerated nanoparticles with different size distribution. The dielectric properties of the samples were studied through HIOKI 3532-50 LCR-Hi TESTER as a function of frequency (100 kHz–3MHz) and temperature (25 °C–500°C). The effects of Co addition, frequency and temperature on the dielectric constants (ϵ' and ϵ''), loss tangent ($\tan \delta$) and ac conductivity (σ_{ac}) have been explained on the basis of hopping of electrons between Fe²⁺ and Fe³⁺ ions.

Keywords: BaFe₁₂O₁₉ Hexaferrite, Co-precipitation method, XRD, Dielectric properties.

Introduction

Hexaferrites form a wide category of ferromagnetic oxide materials that crystallize in complex hexagonal structure with space group P63/mmc [1]. There are six types of Hexaferrites, where the M-type Barium Hexaferrite “BaFe₁₂O₁₉” is the most important type both scientifically and technologically because of its various applications and amazing properties. Scientifically, BaFe₁₂O₁₉ has an excellent chemical stability and corrosion resistivity [2]. Technologically, BaFe₁₂O₁₉ can be used to manufacture permanent magnets and microwave absorbing devices. Also, it is used in

many applications in computer data storage, magneto-optic recording, disc drivers and video recorders [3, 4]. Ferromagnetic oxides have dielectric properties that are used in many microwave applications [5]. The high electrical resistivity of ferrites coupled with their low magnetic losses is critical in maintaining low insertion loss in microwave devices. Any electro-electronic device requests in its composition a permanent magnet. Barium Hexaferrite (BaFe₁₂O₁₉) has been used as a material that presents properties strongly related to the microstructure and morphology. The decrease in the size of the particle results in

advantages, such as high coercivity values, applicability in high frequency, low cost, great resistance to heat and high resistance to corrosion, in comparison to other materials that carry out the same function [6]. Barium Hexaferrite attracted many researchers to synthesis it by various techniques. Raghuram et al. [7] and Elbasuney et al. [8] synthesized $\text{BaFe}_{12}\text{O}_{19}$ by using a hydrothermal method. Moreover, sol-gel method [9-10], sonochemical approach [11], mechanically alloying method [12] and polymeric complex method (Pechini) [13] were previously reported for successful synthesis of $\text{BaFe}_{12}\text{O}_{19}$. However, in this study, co-precipitation method is used due to its simplicity, lower cost and flexibility [14]. Also, co-precipitation method controlled the size and the shape of the nanoparticles by adjusting the pH.

The present paper studies the effects of both Cobalt addition and calcination temperatures on the microstructure and the dielectric properties of barium Hexaferrite $\text{BaFe}_{12}\text{O}_{19}$. For that purpose, $\text{Co}_x\text{BaFe}_{12}\text{O}_{19}$ with $x = 0, 0.04, 0.06$ and 0.1 wt. % were synthesized by the co-precipitation method at different calcination temperatures (900°C and 950°C). Samples' microstructure characterization was performed through XRD and TEM techniques. The dielectric properties of the samples were studied using HIOKI 3532-50 LCR-Hi TESTER in frequency and temperature ranges of 100 kHz-3MHz and $25\text{-}500^\circ\text{C}$, respectively.

Experimental Technique

Synthesis by Co-precipitation Method

Barium Hexaferrite nanoparticles ($\text{BaFe}_{12}\text{O}_{19}$) added with x amount of Cobalt (Co), $0.00 \leq x$ (wt. %) ≤ 0.10 , were synthesized by co-precipitation method. An aqueous solution of Iron (III) chloride hexahydrate ($\text{FeCl}_3 \cdot 6\text{H}_2\text{O}$), Cobalt Chloride (CoCl_2) and Barium Chloride Dihydrate ($\text{BaCl}_2 \cdot 2\text{H}_2\text{O}$) was formed by dissolving these materials in suitable amounts of distilled water. Poly vinyl pyrrolidone (PVP) solution was prepared by dissolving 4g of this polymer in 100 mL distilled water and heated at 80°C for 15 minutes. The two aqueous solutions were mixed and kept under constant stirring by using a magnetic stirrer. Continuous addition of NaOH was done in a drop-wise manner until the pH became 13. The solution obtained was then maintained at a constant temperature of 60°C for

2 hours with constant stirring rate till $\text{Co}_x\text{BaFe}_{12}\text{O}_{19}$ nanoparticles were formed, which was visualized from the dark brown color of the mixture. After that, the mixture was left to cool down naturally for few minutes. The resultant brownish color product was washed continuously with distilled water in order to remove the residues, until the pH was 7 and then dried at 100°C for 18 hours in air. The dried ingots were then heated at different calcination temperatures (900°C and 950°C) for 2 hours.

Sample Characterization and Measurement

XRD patterns of $\text{Co}_x\text{BaFe}_{12}\text{O}_{19}$ were obtained by using Bruker D8 advanced power diffractometer with $20^\circ < 2\theta < 65^\circ$ range and Cu-K_α radiation ($\lambda = 1.54056 \text{ \AA}$). The surface morphology and particle size were examined using transmission electron microscopy (TEM) using Joel JEM-100Cx microscope at an accelerating voltage of 80 kV.

$\text{Co}_x\text{BaFe}_{12}\text{O}_{19}$ nanoparticles were pressed with a load of 13 tons and heated at 900°C and 950°C , the same as their calcination temperatures, for 2 hours. This process was carried out in order to provide more densification and less porosity, reducing the dielectric loss and allowing the storage of more energy. A very thin layer of silver paint was applied at the opposite surfaces of the formed pellets at room temperature. Silver paint was used because of its high conductivity and high melting point (i.e., above 500°C). Due to the low porosity formation and well compact pellets of investigated samples, there is a difficult possibility for diffusing the silver paint between the pore of compact samples. The coated pellet with silver paint was used in the HIOKI 3532-50 LCR HiTESTER in frequency and temperature ranges of 100 kHz-3MHz and 25°C - 500°C , respectively, where the parallel capacitance (C_p) and loss tangent ($\tan \delta$) were measured.

The following relations relate the real part of the dielectric constant (ϵ'), the imaginary part of the dielectric constant (ϵ'') and ac conductivity (σ_{ac}) to the parallel capacitance (C_p) and loss tangent ($\tan \delta$).

$$\epsilon' = \frac{C_p d}{\epsilon_0 A}, \quad (1)$$

$$\epsilon'' = \epsilon' \tan \delta, \quad (2)$$

$$\text{and } \sigma_{ac} = \epsilon_0 \omega \epsilon' \tan \delta, \quad (3)$$

where $\omega = 2 \pi f$ and f is the frequency of the applied ac field (Hz), d is the sample thickness ($d = 0.4$ cm), ϵ_0 is the permittivity of free space (8.85×10^{-12} F/m) and A is the area of the sample ($A = 5.3$ cm²).

Results and Discussion

Structural Analysis

Fig. 1 shows XRD patterns for Co_xBaFe₁₂O₁₉ nanoparticles, with $x = 0.00$ and 0.06 wt. %, prepared at calcination temperatures 900°C and 950°C . The observed peaks are well indexed by the hexagonal indices of BaFe₁₂O₁₉ (ICDD Card No-840757) with space group P63/mmc and in agreement with the Reitveld refinement shown in the inset of Fig. 1. These peaks correspond to the planes (006), (110), (112), (107), (114), (205), (206), (209), (004), (2011) and (220). Minor peak of α -Fe₂O₃ phase is also presented in the patterns indexed as (203) at $2\theta \approx 37^\circ$. Ding et al. [15] reported that, from Mössbauer spectra, α -Fe₂O₃ is usually associating the formation of

Barium Hexaferrite. The BaFe₁₂O₁₉ phase percentages are calculated and are listed in Table 1. It is clear that BaFe₁₂O₁₉ phase percentage is enhanced with increasing both the addition content x to 0.1 wt. % and the calcination temperature to 950°C . This means that increasing Co-addition and calcination temperature reduces the percentage of the secondary phases and increases the percentage of BaFe₁₂O₁₉ phase. This may be attributed to the interstitial diffusion of barium atoms into the cation vacancy of α -Fe₂O₃. Packiaraj et al. [16] reported similar results. They concluded that by increasing the calcination temperature, the intermediate phases, such as γ -Fe₂O₃, α -Fe₂O₃ and BaFe₂O₄, decreased whereas BaFe₁₂O₁₉ phase increased and appeared as a major phase at 950°C . Zhong et al. [17] reported about the fact that the appearance of α -Fe₂O₃ with orthorhombic hexahedron structure prevents the formation of BaFe₁₂O₁₉ hexagonal structure at low temperatures below 750°C .

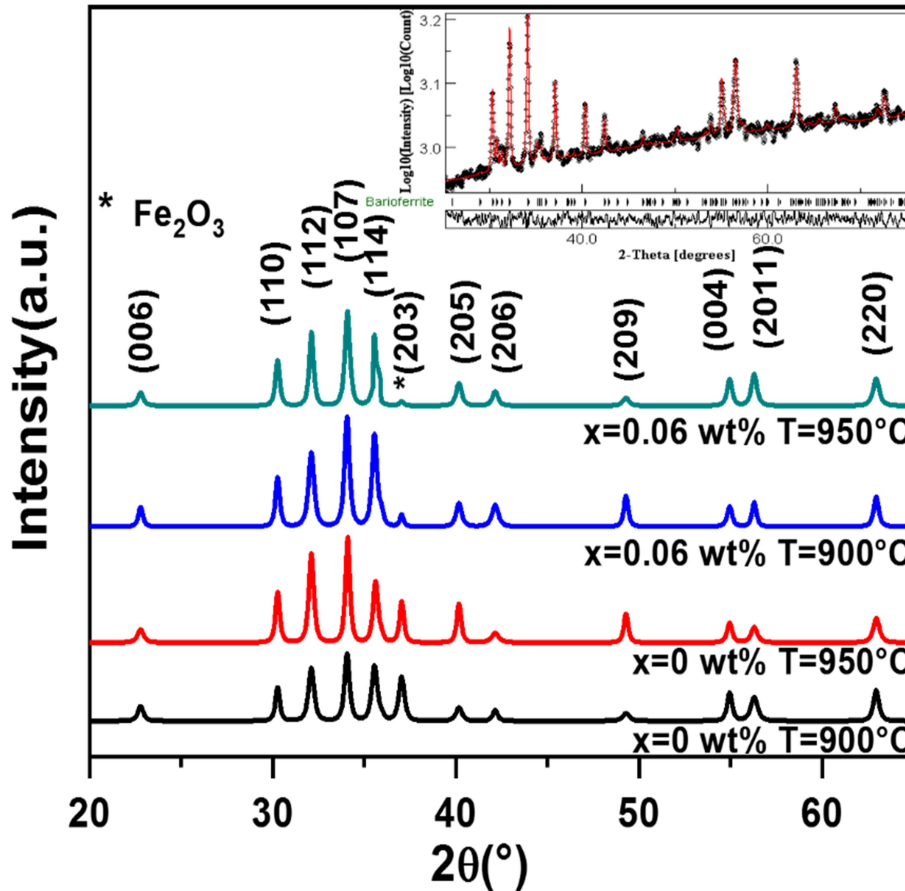


FIG. 1. XRD patterns for $x = 0.00$ and 0.06 wt. % at $T = 900^\circ\text{C}$ and 950°C with the inset of Reitveld refinement.

Lattice parameters (a and c) were calculated using MAUD program and unit cell volume V was calculated using equation $V = \frac{\sqrt{3}}{2} a^2 c$. The ratio c/a is constant for all prepared samples. The average crystallite size of the samples was calculated using Debye-Scherrer equation $D = \frac{S\lambda}{\beta_{hkl} \cos\theta}$, where D is the average crystallite size in nm, S is the shape factor which is equal to 0.9, λ is the wavelength of the X-ray radiation, β_{hkl} is the peak width at half-maximum intensity and θ is the peak position. The values of a, c, V and D at different calcination temperatures (T= 900°C and 950°C) for $\text{Co}_x\text{BaFe}_{12}\text{O}_{19}$ are listed in Table 1. As can be seen from Table 1, the values of a, c and V are slightly varied with either Cobalt addition or calcination temperatures. This indicates that Cobalt occupies only interstitial places in the Barium Hexaferrite matrix without entering the structure. Also, it is clear that the crystallite size D has unsystematic variation with

both x and T and that samples sintered at 950°C, except for x = 0.04 wt. % sample, have higher values of D in comparison with their counterparts sintered at 900°C. This result is consistent with the XRD peak width that becomes narrower with increasing calcination temperature to 950°C (see Fig. 1), which indicates that the average crystalline size of the prepared ferrites increased gradually. Kaur et al. [18] reported similar variations in crystallite size. The decrease in crystalline size may be attributed to smaller ionic radii of Co (0.625 Å) than Fe (0.63 Å) and Ba (1.11 Å), while the increase in crystalline size may be explained by cobalt ions being dissolved in $\text{BaFe}_{12}\text{O}_{19}$ grains and the excess of these ions being directed towards the grain boundaries, thus enhancing the liquid phase sintering. The value of c/a is almost constant and equal to 3.93, meaning that the crystal structure may be thought of as composed of planes of closely packed atoms.

TABLE 1. $\text{BaFe}_{12}\text{O}_{19}$ phase percentage, lattice parameters (a and c), unit cell volume (V), crystalline size (D) and grain size (D_{TEM}) of $\text{Co}_x\text{BaFe}_{12}\text{O}_{19}$ nanoparticles with ($0 \leq x \leq 0.10$) at calcination temperatures= 900°C and 950°C.

T (°C)	x (wt%)	$\text{BaFe}_{12}\text{O}_{19}$ (%)	a (Å)	c (Å)	c/a	V (Å ³)	D (nm)	D_{TEM} (nm)	I
900	0.00	90.36	5.87	23.14	3.93	692.6	51.5	80.29	1.55
	0.04	90.43	5.88	23.21	3.93	693.6	55.57	73.61	1.32
	0.06	90.83	5.87	23.16	3.94	696.9	51.42	74.56	1.45
	0.10	90.84	5.87	23.12	3.93	693.0	54.98	95.52	1.73
950	0.00	91.01	5.87	23.13	3.93	692.7	58.76	95.65	1.62
	0.04	91.02	5.87	23.13	3.93	693.3	52.02	69.82	1.34
	0.06	91.69	5.87	23.16	3.94	693.9	54.60	82.40	1.51
	0.10	91.72	5.87	23.12	3.93	692.0	57.54	164.51	2.85

TEM Investigation

The shape as well as the average particle size of pure and Cobalt-added $\text{Co}_x\text{BaFe}_{12}\text{O}_{19}$ nanoparticles were examined using TEM technique. Figs. 2a-d show TEM micrographs coupled with their Gaussian distribution of $\text{Co}_x\text{BaFe}_{12}\text{O}_{19}$ with x= 0.00 and x= 0.06 wt. %, at T = 900°C and T = 950°C, respectively. The average particle sizes D_{TEM} are calculated from the mean of the Gaussian distribution and are listed in Table 1. The average particle sizes for all the synthesized samples are in the range of 69-164 nm. Moreover, the particle sizes show nonlinear variation with Co-addition and increasing calcination temperature. This result is consistent with the behaviour of the average crystallite sizes D calculated from XRD analysis. It is clear from the micrographs that the samples

are mainly composed of agglomerated grains that form clusters of different sizes and shapes. In addition, it is clear that the sample morphology is changed to some extent to agglomerated hexagonal grains with increasing Co-addition and calcination temperature, as shown in Fig. 2d. Jurek et al. [19] observed hexagonal shaped particles for Barium Hexaferrite with diameter 50–70 nm. The crystallinity index (I) is investigated to check the crystallinity of the sample and is calculated by the following equation:

$$I = D_{\text{TEM}}/D_{\text{XRD}} \quad (4)$$

All the values obtained are listed in Table 1. They are found to be in the range of (1.32 -2.85). These values indicate that the samples are monocrystalline samples.

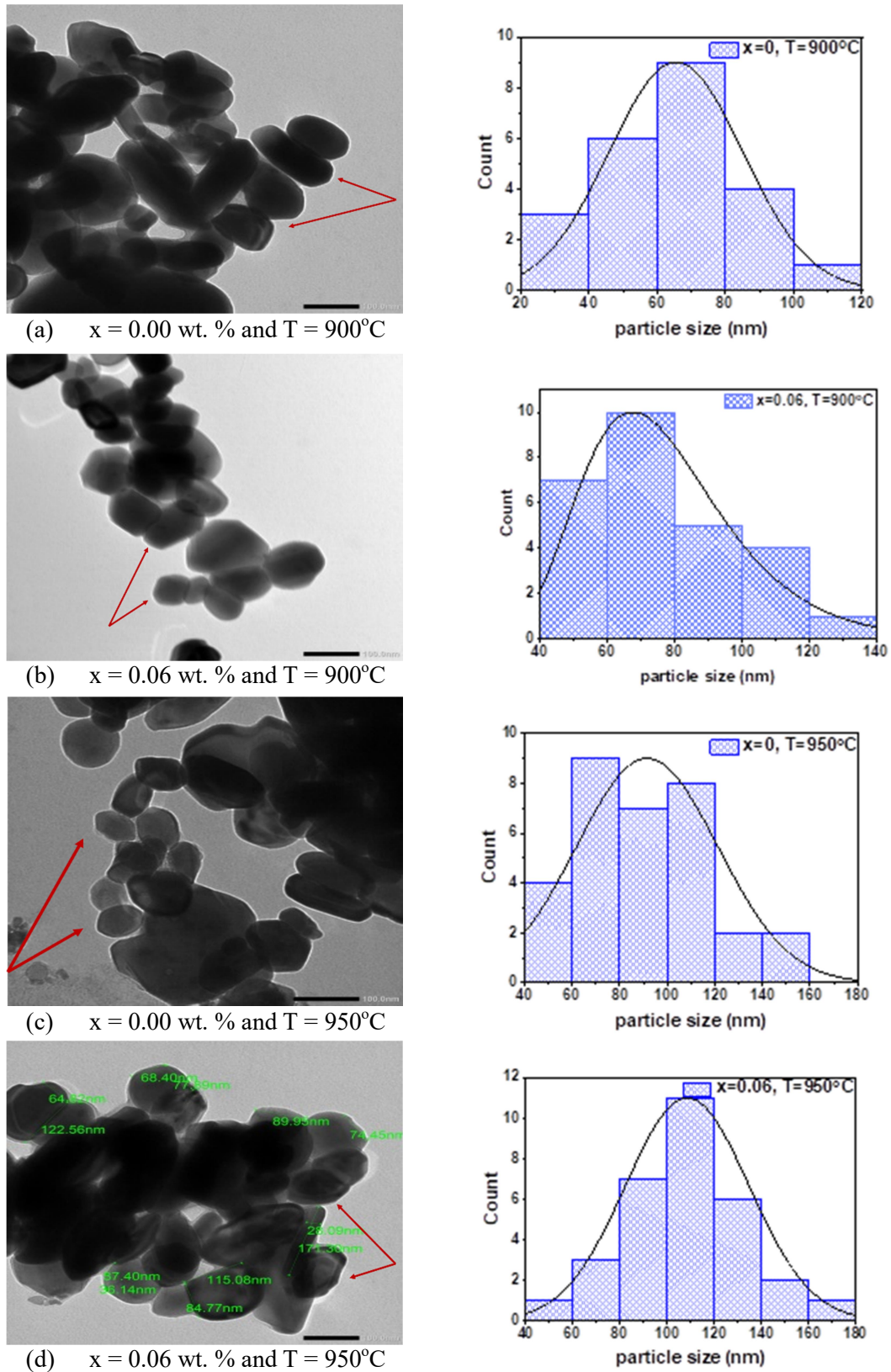


FIG. 2. TEM micrographs with 100 nm magnification scale and Gaussian distribution of $\text{Co}_x\text{BaFe}_{12}\text{O}_{19}$ with (a) $x = 0.00$ and at $T = 900^\circ\text{C}$, (b) $x = 0.06$ wt.% and at $T = 900^\circ\text{C}$, (c) $x = 0.00$ and at $T = 950^\circ\text{C}$ and (d) $x = 0.06$ wt.% and at $T = 950^\circ\text{C}$.

Dielectric Properties

Fig. 3(a) shows the variation of the real part of the dielectric constant (ϵ') with frequency (f) at fixed temperature $T=500^\circ\text{C}$ for $\text{Co}_x\text{BaFe}_{12}\text{O}_{19}$ (with $x = 0, 0.04, 0.06$ and 0.1 wt. %) samples calcined at 900°C and 950°C . The dielectric response can be visualized as; in the low frequency region (10^3 Hz) ϵ' has high values which decrease rapidly with increasing frequency followed by a plateau with lower values in the high frequency region (10^4 - 10^6 Hz). This behaviour can be explained on the basis of Koop's phenomenological theory and Maxwell Wagner theory [20]. This could be related to an electron hopping between Fe^{3+} and

Fe^{2+} ions. This will lead to the displacement of the ionic charges and is also responsible for interfacial polarization. Also, at low frequencies, the free charge carriers at grain boundaries or oxygen ion vacancies during the sintering process could have an effective contribution to interfacial polarization. Due to heat treatment, the structure of ferrite materials is supposed to be made of conducting grains separated by less conducting grain boundaries [21]. When hopping time is less than a half of the alternating field only, the electric field displaces the electrons, which leads to polarization. As a result, the dielectric constant will decrease at high frequency [22].

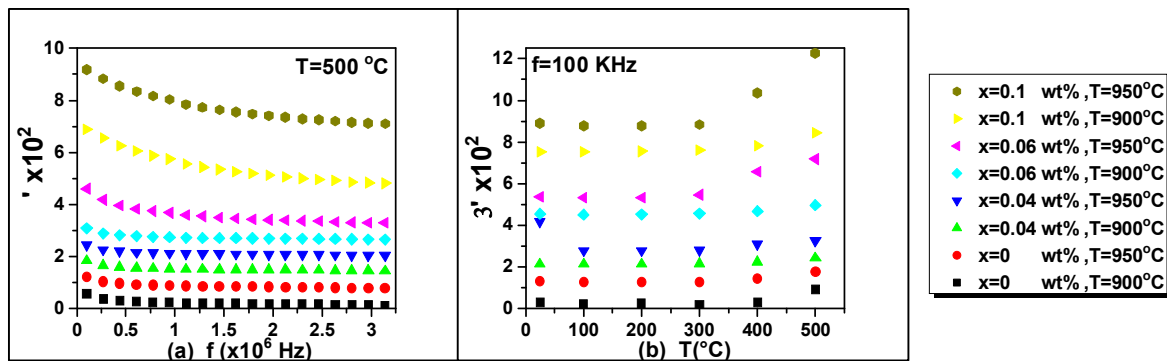


FIG. 3. The variation of ϵ' with (a) frequency at fixed temperature $T = 500^\circ\text{C}$ and (b) temperature at fixed frequency $f = 100$ kHz for $\text{Co}_x\text{BaFe}_{12}\text{O}_{19}$ calcined at 900°C and 950°C .

The variation of ϵ' with temperature at fixed frequency of 100 kHz for $\text{Co}_x\text{BaFe}_{12}\text{O}_{19}$ samples is shown in Fig. 3(b). It can be seen that ϵ' values show increment with increasing temperature from 25°C to 500°C . Finally, it is noted that ϵ' is strongly dependent on both Co-addition and calcination temperature, as it increases with increasing Co-addition from 0 to 0.1 wt. % and samples sintered at 950°C have higher values of ϵ' than those sintered at 900°C .

Fig. 4(a) displays the variation of the imaginary part of the dielectric constant (ϵ'') with frequency (f) at fixed temperature $T = 500^\circ\text{C}$ for $\text{Co}_x\text{BaFe}_{12}\text{O}_{19}$ (with $x = 0, 0.04, 0.06$ and 0.1 wt. %) samples calcined at 900°C and 950°C . It is clearly observed from Fig. 4(a) that the variation behavior of ϵ'' with frequency is very similar to the variation of ϵ' with f . Similarly, ϵ'' is found to exhibit a sharp decrease in the low-frequency region, then as the frequency increases, ϵ'' is observed to decrease slowly until it becomes independent on frequency at high-frequency range. The high values of ϵ'' obtained for all samples at low

frequency can be also attributed to the microstructure characteristics and morphological parameters, such as density, porosity, grain boundary sizes and other crystalline defects [23, 24], which results in space-charge polarization increment and consequently enhancement in the values of ϵ'' . However, further decrease in ϵ'' values with the increase in frequency is explained by the idea that any species contributing to polarization is found to show lagging behind the applied field as frequency becomes higher and higher.

Fig. 4(b) displays the variation of the imaginary part of the dielectric constant ϵ'' with temperature at fixed frequency $f = 100$ kHz. It is clearly observed from the figure that ϵ'' increases with increasing temperature. This result can be explained by dipolar and interfacial polarizations, but it is more noticeable in the interfacial polarization, where hoping of more electrons takes place under the thermal effect. This result was confirmed by Maxwell Wagner model [25].

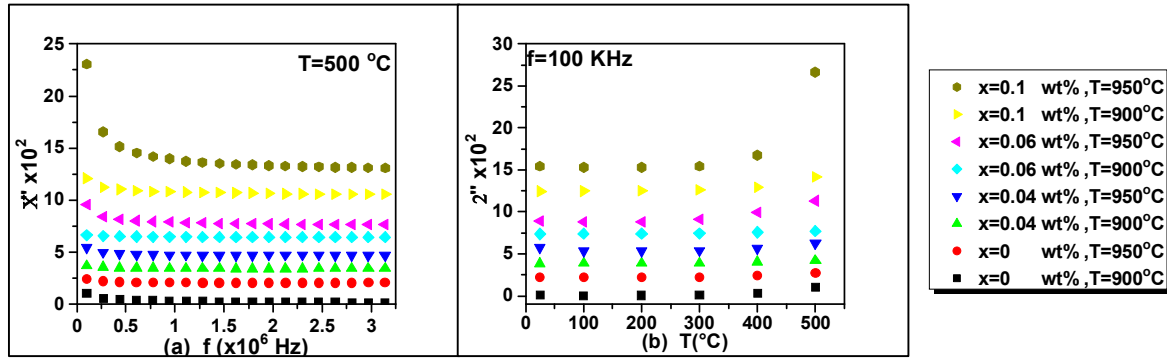


FIG. 4. The variation of ϵ'' with (a) frequency at fixed temperature $T = 500^\circ\text{C}$ and (b) temperature at fixed frequency $f = 100\text{ kHz}$ for $\text{Co}_x\text{BaFe}_{12}\text{O}_{19}$ calcined at 900°C and 950°C .

The behavior of dielectric loss ($\tan \delta$) with frequency at fixed temperature $T = 500^\circ\text{C}$ for $\text{Co}_x\text{BaFe}_{12}\text{O}_{19}$ (with $x = 0, 0.04, 0.06$ and 0.1 wt. %) samples calcined at 900°C and 950°C is shown in Fig. 5(a). It is clear that after reaching a maximum value, dielectric loss $\tan \delta$ decreases with increasing frequency. The high dielectric constant is a result of hopping, where the loss tangent behavior can similarly be explained on this basis. When the hopping is nearly equal to that of the externally applied electric field, maximum of loss tangent could be observed.

After reaching the maximum, hopping time becomes more than the applied signal, which causes a decrease in loss tangent.

The dielectric loss ($\tan \delta$) as a function of temperature is represented in Fig. 5(b), where the dielectric loss ($\tan \delta$) increases with increasing calcination temperature. The dipole orientation increases as the temperature increases and as a result, the dipole losses increase. This means that more electrons and space charge polarizations were manifesting at higher temperatures [25].

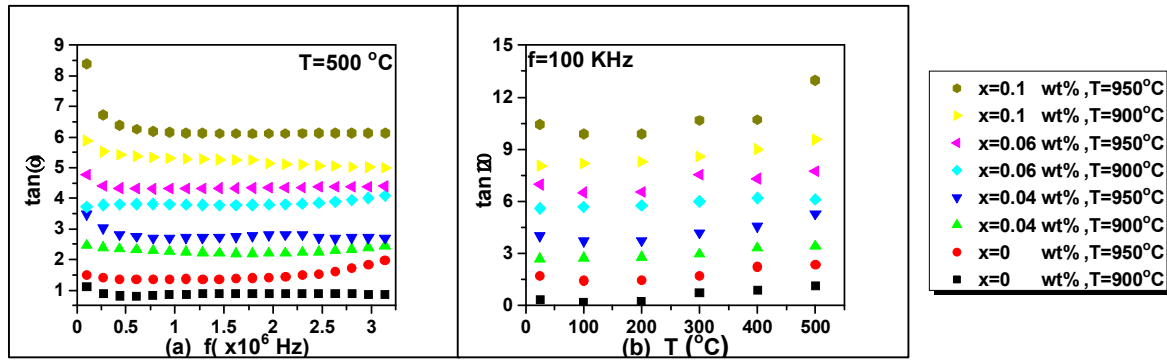


FIG. 5. The variation of $\tan \delta$ with (a) frequency at fixed temperature $T = 500^\circ\text{C}$ and (b) temperature at fixed frequency $f = 100\text{ kHz}$ for $\text{Co}_x\text{BaFe}_{12}\text{O}_{19}$ calcined at 900°C and 950°C .

The ac conductivity (σ_{ac}) dependence on frequency at fixed temperature $T = 500^\circ\text{C}$ for $\text{Co}_x\text{BaFe}_{12}\text{O}_{19}$ (with $x = 0, 0.04, 0.06$ and 0.1 wt. %) samples calcined at 900°C and 950°C is recorded in Fig. 6(a). The results show that σ_{ac} exhibits an increasing trend with the increase in the applied ac field frequency. The increase in conductivity is due to the increase in the charge carriers as the applied frequency increases [26]. Similar increasing trends were reported for several ferrites [27-28]. At lower frequencies, the poor-conducting grain boundaries are active and hence the exchange between Fe^{2+} and Fe^{3+}

ions is low and this explains the low values of σ_{ac} obtained at low frequency. However, as the frequency increases, the conductive grains become more active than the grain boundaries causing an increase in the exchange between Fe^{2+} and Fe^{3+} ions and therefore an increase in the conduction [20] and consequently in the σ_{ac} values. It is clear from Fig. 6(b) of σ_{ac} versus temperature at $f = 100\text{ kHz}$ that the temperature greatly affects the ac conductivity, σ_{ac} . At high temperature, the charge carriers are thermally activated; so their velocity increases, leading to an increase in conductivity.

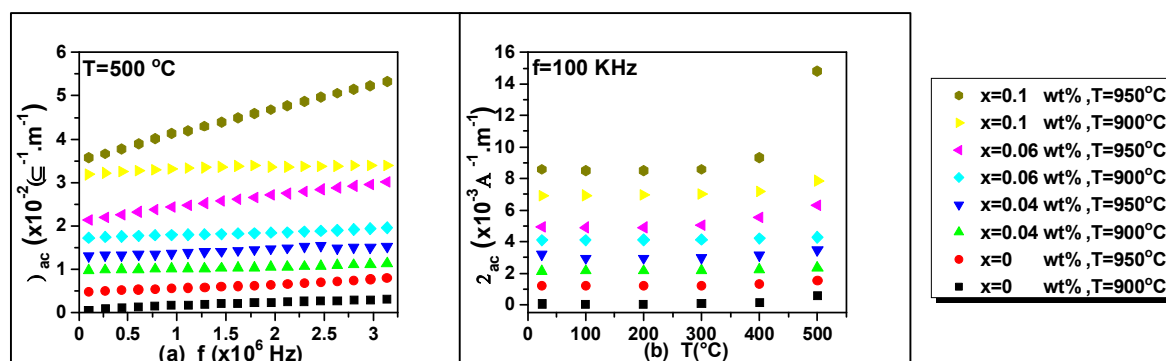


FIG. 6. The variation of σ_{ac} with (a) frequency at fixed temperature $T = 500^\circ\text{C}$ and (b) temperature at fixed frequency $f = 100 \text{ kHz}$ for $\text{Co}_x\text{BaFe}_{12}\text{O}_{19}$ calcined at 900°C and 950°C .

Conclusion

Chemical co-precipitation method was successfully utilized to prepare nanoparticles of $\text{Co}_x\text{BaFe}_{12}\text{O}_{19}$, with $x = 0, 0.04, 0.06$ and 0.1 wt. \% . The effects of Cobalt addition and calcination temperature (900°C and 950°C) on the microstructure, morphology and dielectric properties of the synthesized samples were investigated. XRD results revealed the hexagonal structure of the prepared samples and indicated enhancement in the phase formation of $\text{BaFe}_{12}\text{O}_{19}$ and reduction of Fe_2O_3 phase with increasing both the Co-addition and calcination temperature. Moreover, the lattice parameters (a and c) and unit cell volume (V) were almost unchanged with either Cobalt addition or calcination temperatures. By the use of Debye–Scherrer equation, the crystallite size was varied from $51\text{--}58 \text{ nm}$. Samples morphology was studied through TEM technique. TEM micrographs clarified that the samples are mainly composed of agglomerated grains that form hexagonal-shaped particles. The behaviours of the dielectric constants (ϵ' and ϵ''), loss tangent ($\tan \delta$) and ac conductivity (σ_{ac}) have

been explained on the basis of hopping of electrons between Fe^{2+} and Fe^{3+} ions. Moreover, the Co-addition and the calcination temperature elevation lead to higher dielectric constants (11.9×10^2 at $T=500^\circ\text{C}$ and $f=100 \text{ kHz}$) and enhanced ac conductivities ($15.1 \times 10^{-3} \text{ A}^{-1}\text{m}^{-1}$) for samples calcined at 950°C . As a conclusion, the dielectric properties are highly dependent on the hexagonal structure of the $\text{Co}_x\text{BaFe}_{12}\text{O}_{19}$ and the exchange between $\text{Fe}^{2+}\text{--}\text{Fe}^{3+}$ ions. In addition, it is noted that as the calcination temperature increases, the crystallite size increases with an enhancement in both real and imaginary dielectric constants, $\tan \delta$ and ac conductivity.

Acknowledgement

This work was performed in the materials science lab, Physics Department, Faculty of Science, Beirut Arab University, Beirut, Lebanon; in cooperation with Physics Department, Alexandria University, Alexandria, Egypt and Physics Department, Lebanese University, Beirut, Lebanon.

References

- [1] Kaur, T., Kaur, B., Bhat, B.H., Kumar, S. and Srivastava, A.K., *Physica B: Condensed Matter*, 456 (2015) 206.
- [2] Martirosyan, K.S., Galstyan, E., Hossain, S.M., Wang, Y.J. and Litvinov, D., *Mater. Sci. Eng. B*, 176 (2011) 8.
- [3] Pullar, R.C., *Prog. Mater. Sci.*, 57 (2012) 1191.
- [4] Rashad, M.M. and Ibarhim, I.A., *J. Supercond. Nov. Magn.*, 26 (2013) 1639.
- [5] Mallick, K.K., Shepherd, P. and Green, R.J., *Journal of the European Ceramic Society*, 27 (2007) 2045.
- [6] Pereira, F.M.M., Santos, M.R.P., Sohn, R.S.T.M., Almeida, J.S., Medeiros, A.M.L., Costa, M.M. and Sombra, A.S.B., *Journal of Materials Science: Materials in Electronics*, 20 (2009) 408.
- [7] Raghuram, N., Rao, T.S. and Babu Naidu, K.C., *Materials Science in Semiconductor Processing*, 94 (2019) 136.

- [8] Elbasuney, S., Gobara, M. and Yehia, M., *Journal of Inorganic and Organometallic Polymers and Materials*, 29 (2019) 721.
- [9] Almessiere, M.A., Slimani, Y., Tashkandi, N.A., Baykal, A., Saraç, M.F., Trukhanov, A.V., ... and Özçelik, B., *Ceramics International*, 45 (2019) 1691.
- [10] Zhuravlev, V.A., Itin, V.I., Minin, R.V., Lopushnyak, Y.M., Svetlichnyi, V.A., Lapin, I.N., ... and Lilenko, I.Y., *Journal of Alloys and Compounds*, 771 (2019) 686.
- [11] Sadaqat, A., Almessiere, M., Slimani, Y., Guner, S., Sertkol, M., Albetran, H., ... and Ercan, I., *Ceramics International*, 45 (2019) 22538.
- [12] Manafi, S.A., Jougehhdoust, S., Kiahosseini, S.R. and Farahbakhsh, I., *Journal of the Australian Ceramic Society*, 55 (2019) 371.
- [13] Urbano-Peña, M.A., Palomares-Sánchez, S.A., Betancourt, I., Pérez-Juache, T.J. and Ruiz, F., *Applied Physics A*, 125 (2019) 711.
- [14] Hu, S.L., Liu, J., Yu, H.Y. and Liu, Z.W., *Journal of Magnetism and Magnetic Materials*, 473 (2019) 79.
- [15] Ding, J., Yang, H., Miao, W.F., McCormick, P.G. and Street, R., *Journal of Alloys and Compounds*, 221 (1995) 70.
- [16] Packiaraj, G., Panchal, N. and Jotania, R.B. *International Journal of Systems Biology*, 2 (2010) 5.
- [17] Zhong, W., Ding, W., Jiang, Y., Zhang, N., Zhang, J., Du, Y. and Yan, Q., *Journal of the American Ceramic Society*, 80 (1997) 3258.
- [18] Qiu, J., Zhang, Q., Gu, M. and Shen, H., *Journal of Applied Physics*, 98 (2005) 103905.
- [19] Ziełńska-Jurek, A., Bielan, Z., Dudziak, S., Wolak, I., Sobczak, Z., Klimczuk, T. and Hupka, J., *Catalysts*, 7 (2017) 360.
- [20] Singh, A., Narang, S.B., Singh, K., Pandey, O.P. and Kotnala, R.K., *J. Ceram. Process. Res.*, 11 (2010) 241.
- [21] Ali, I., Islam, M.U., Awan, M.S. and Ahmad, M., *J. Electron. Mater.*, 43 (2014) 512.
- [22] Narang, S.B. and Hudhara, I.S., *J. Ceram. Process. Res.*, 7 (2006) 113.
- [23] Ali, I., Islam, M.U., Awan, M.S. and Ahmad, M., *J. Mater. Eng. Perform.*, 22 (2013) 2104.
- [24] Hajalilou, A., Kamari, H.M. and Shameli, K., *Journal of Alloys and Compounds*, 708 (2017) 813.
- [25] Mansour, S.F. and Abdo, M.A., *Journal of Magnetism and Magnetic Materials*, 428 (2017) 300.
- [26] Hankare, P.P., Sankpal, U.B., Patil, R.P., Jadhav, A.V., Garadkar, K.M. and Chougule, B.K., *Journal of Magnetism and Magnetic Materials*, 323 (2011) 389.
- [27] Melagiriappa, E., Jayanna, H.S. and Chougule, B.K., *Materials Chemistry and Physics*, 112 (2008) 68.
- [28] El-Ata, A.A., El-Nimr, M.K., Attia, S.M., El-Kony, D. and Al-Hammadi, A.H., *Journal of Magnetism and Magnetic Materials*, 297 (2006) 33.

Dielectric Properties of $Y_3Fe_5O_{12}$ (YIG) Prepared at Different Molarities of NaOH

B. Assi, Z. Bitar, W. Malaeb and R. Awad

Physics Department, Faculty of Science, Beirut Arab University, Beirut, Lebanon.

Doi : <https://doi.org/10.47011/13.3.5>

Received on: 08/08/2019;

Accepted on: 23/02/2020

Abstract: In this study, Yttrium Iron Garnet ($Y_3Fe_5O_{12}$) (YIG) powders were synthesized *via* co-precipitation method, followed by calcining the precipitates at 1100°C. The garnets produced were obtained from aqueous iron and yttrium chloride mixtures using different molarities of NaOH (M=2, 3, 4 and 5) at pH=12. The phase formation and crystallography were investigated using X-ray diffraction (XRD), the morphology was investigated using transmission electron microscopy (TEM) and the dielectric properties were measured using an impedance analyzer in the frequency range 0.5 - 5MHz, in a temperature range 22 - 350°C. X-ray diffraction peaks showed the formation of cubic YIG with lattice parameter varying between 12.334 and 12.339 Å. The grain size, measured from TEM images, decreased with the increase of the molarity of NaOH. Plots of the real part of the dielectric constant ϵ' , the imaginary part of the dielectric constant ϵ'' , loss tangent $\tan \delta$ and ac conductivity σ_{ac} as functions of frequency and temperature, respectively, were obtained. It was observed that the highest values of the dielectric constant were obtained in the 2M sample.

Keywords: Dielectric properties, Yttrium Iron Garnet (YIG), Co-precipitation method, NaOH molarity.

Introduction

Yttrium Iron Garnet ($Y_3Fe_5O_{12}$) (YIG) belongs to a class of magnetic oxides which is the garnets. It has 160 unit cells in 3 different sites that are octahedral, dodecahedral and tetrahedral. The importance of YIG resides in the fact that it is of technological significance due to its various properties. It possesses the highest quality factor in the microwave regime, the smallest linewidth in magnetic resonance among the magnetic materials, controllable high saturation magnetization, large Faraday rotation and low propagation loss [1-2]. These, in addition to other properties, have made it a basis for many high-technology devices, such as telecommunication devices, lasers, phase shifters, sensors and oscillators [3]. Specifically, the dielectric properties of YIG, such as its low dielectric loss tangent in the microwave region,

have grabbed a lot of attention and made it possible for the YIG to be used in electronic devices as tunable microwave devices. For this reason, the manipulation of dielectric properties of YIG under various conditions in different ranges has been a major research topic recently. For instance, Ramesh et al. [4] studied the effect of the sintering temperature on the magnetic and dielectric properties of YIG, while Ahmad et al. [5] mentioned that doping YIG by samarium (Sm) has an effect on its dielectric permittivity. Several techniques have been used to prepare YIG powders, including sol-gel [6], Pechini method [7], metallo-organic decomposition [8] and chemical co-precipitation [9]. These top-down techniques are all capable of producing YIG samples; however, the Pechini method results in the production of large-sized particles

and the metallo-organic YIG has a high percentage of impurities. In our work, coprecipitation is chosen to prepare YIG based on a variety of parameters that can be studied, as well as on cheap cost and simplicity. The aim of this work is to investigate the dielectric properties of YIG prepared using different molarities of NaOH during the titration process to reach pH = 12, as there are no reports yet of a similar study.

Experimental

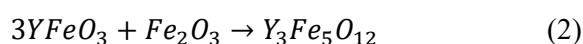
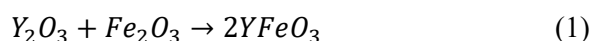
Polycrystalline Yttrium Iron Garnet (YIG) samples were synthesized using the coprecipitation method. $YCl_3 \cdot 6H_2O$ and $FeCl_3 \cdot 6H_2O$ were weighed in a stoichiometric ratio Y:Fe = 3:5 and dissolved in de-ionized water to form an aqueous solution of chlorides. This solution was titrated drop-wise with stirred NaOH solutions of different molarities (2, 3, 4 and 5M) to reach pH = 12. Then it was heated at 90°C for 4 hours with constant-speed stirring. The obtained mixtures were then washed with distilled water followed by drying for 18 hours at 100°C. Subsequently, the dried precipitates were ground and moved to a tube furnace to be calcinated at 1100°C for 2 hours.

The phase formation and crystallography were studied using X-ray powder diffraction (XRD) and the morphology was studied using Transmission Electron Microscopy (TEM). The dielectric studies were carried out by an LCR meter in the frequency range 0.5 - 5MHz, in the temperature range 22 - 350°C.

Results and Discussion

Structural Analysis of YIG

Fig. 1 shows XRD patterns of YIG powders prepared at different molarities of NaOH (2, 3, 4 and 5M). The diffraction peaks of the $Y_3Fe_5O_{12}$ (JCPDS: 21-1450) [10] phase indicate that YIG crystallized into a cubic structure with space group $Ia3d^5$. The XRD patterns showed the existence of a second phase; the Yttrium Iron Perovskite ($YFeO_3$) (JCPDS: 39-1489) [11]. From the XRD results, the garnet formation can be described as follows [12]:



The reason behind the existence of $YFeO_3$ could be shown in the equations of formation above. The formation of $YFeO_3$ takes place before the formation of the YIG phase and its existence after calcination is attributed to the fact that the samples were calcinated at a temperature below 1300°C [13]. The lowest intensity of the peak (121) corresponding to $YFeO_3$ was observed in the 3M sample. The values of the lattice parameter (a) were calculated by indexing the XRD patterns and using the equation $a = d_{hkl} \sqrt{h^2 + k^2 + l^2}$, where d_{hkl} is the lattice spacing and h , k and l are the Miller indices. It is shown in Table 1 that the increase of the molarity showed a slight effect on the lattice parameter, where its value varied between 12.334 and 12.339 Å.

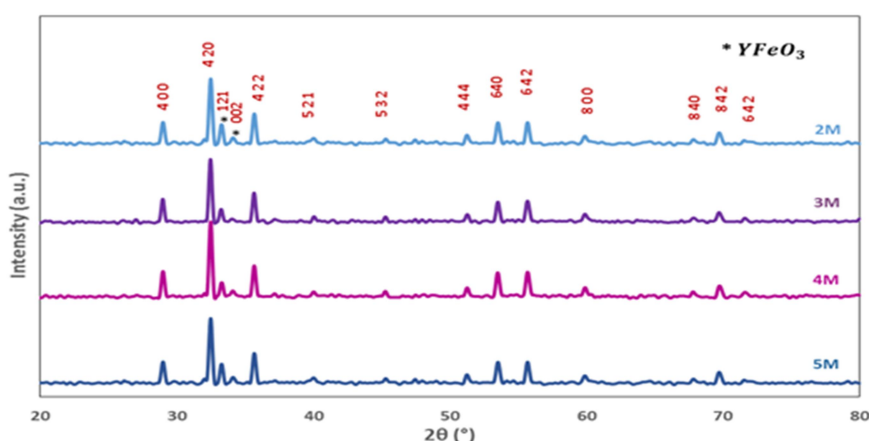


FIG. 1. XRD patterns of YIG powders prepared at different molarities of NaOH.

Fig. 2 shows the TEM photographs of the YIG samples prepared with 2, 3 and 5M of NaOH. The particles show an irregular shape

which could be resolved by increasing the temperature of calcination, whereas the agglomeration shown could be due to the piling

up of a few nanocrystals on the large-sized grains [14]. The average grain size of the particles obtained from TEM photographs

decreases from 163.42 nm to 91.09 nm as the molarity increases from 2M to 5M, as shown in Table 1.

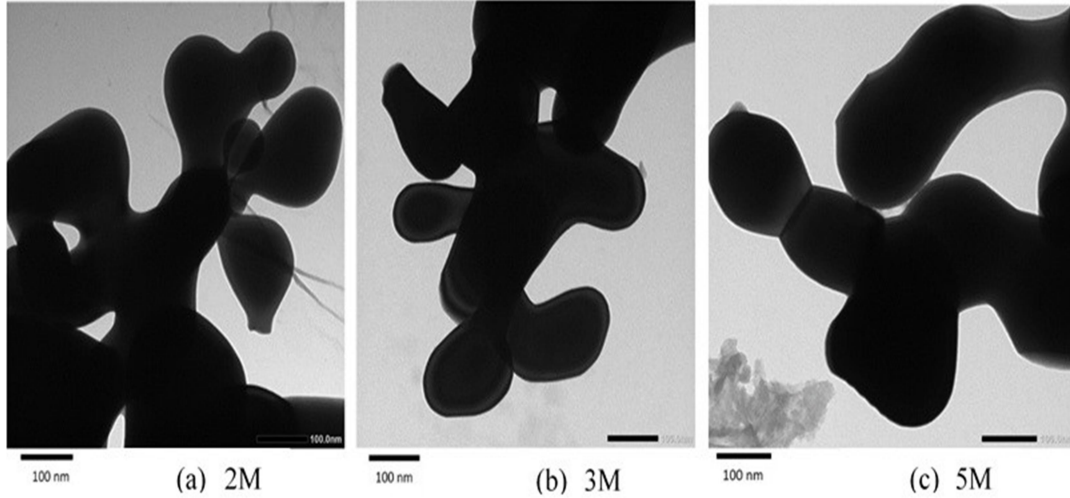


FIG. 2. TEM photographs of the YIG powders prepared with 2, 3 and 5M of NaOH.

TABLE 1. The lattice parameter (\AA) and the grain size (nm) of the YIG powders prepared with 2, 3, 4 and 5M NaOH.

Sample	Lattice parameter (\AA)	Grain size (nm)
2M	12.339	163.42
3M	12.338	107.47
4M	12.335	-
5M	12.334	91.09

Dielectric Studies of YIG

The real (ϵ') and imaginary (ϵ'') parts of the dielectric constant and the ac conductivity σ_{ac} were calculated from the dielectric measurements using the following equations:

$$\epsilon' = Cd/A\epsilon_0 \quad (3)$$

$$\epsilon'' = \tan \delta \cdot \epsilon' \quad (4)$$

$$\sigma_{ac} = \epsilon'' \cdot \omega \cdot \epsilon_0 \quad (5)$$

where d is the sample disc thickness, A is the electrode area, C is the capacitance, ϵ_0 is the empty space permittivity, $\tan \delta$ is the dielectric loss measured by the instrument and ω is the angular frequency. The dimensions of the used pellets of the prepared samples are $d = 2.2 \pm 0.1$ mm and $A = 1.249 \times 10^{-4} \text{ m}^2$.

Figs. 3 (a) and 4 (a) show, respectively, the influence of frequency on the real (ϵ') and imaginary (ϵ'') parts of the dielectric constant. The highest values of both constants are obtained in the 2M sample, where the grain size is the largest. The effect of grain size on the dielectric constants can be explained by its effect on the population of domains and the movement of domain walls [15]. Both dielectric constants increase when the frequency increases. The dielectric constants arise from the polarization and movement of dipole orientation. This dipole orientation takes time, but as the frequency increases, the response time becomes comparable to the period of the field, thus the dielectric constants increase. A peak is observed in all the samples, which can be attributed to the occurrence of resonance, where the frequency of the applied electric field happens to be the same as the frequency of dipole orientation [16].

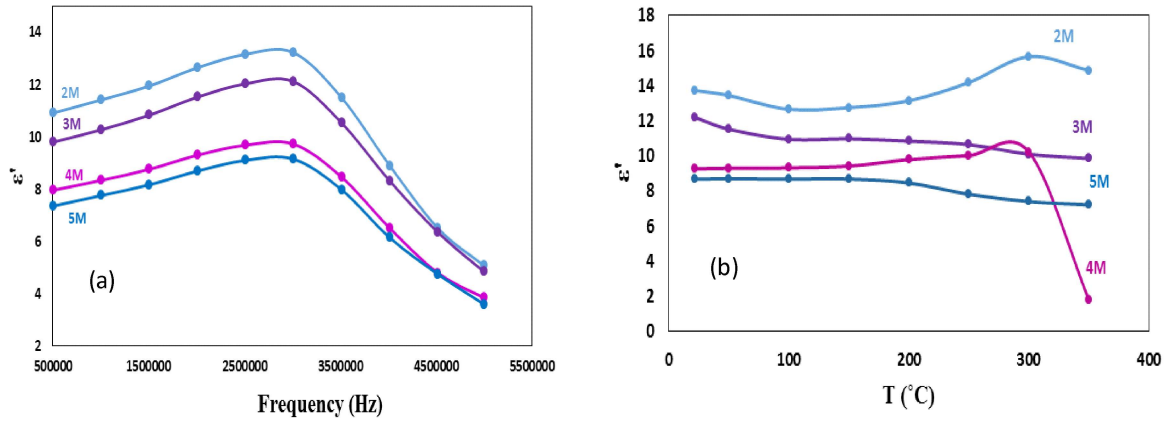


FIG. 3. Variation of the real part ϵ' of the dielectric constant of the YIG samples (a) as a function of frequency at room temperature and (b) as a function of temperature at 2 MHz.

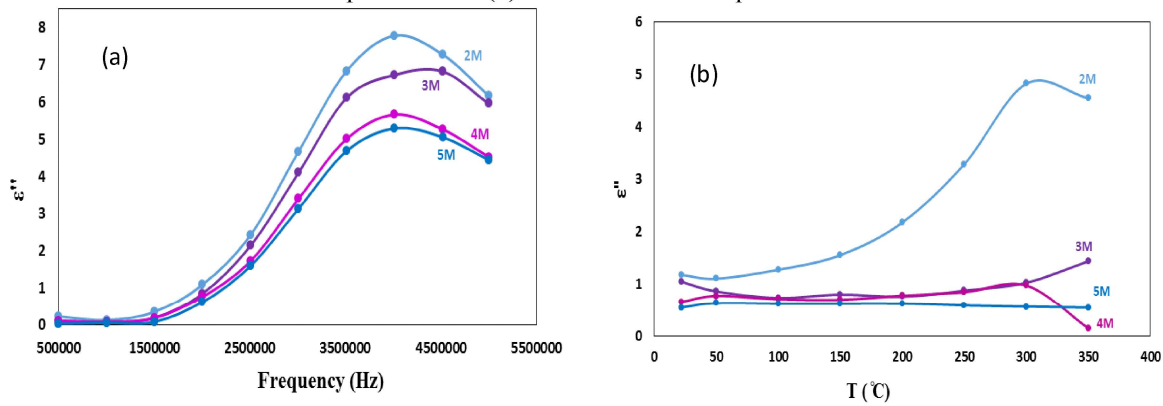


FIG. 4. Variation of the imaginary part ϵ'' of the dielectric constant of the YIG samples (a) as a function of frequency at room temperature and (b) as a function of temperature at 2 MHz.

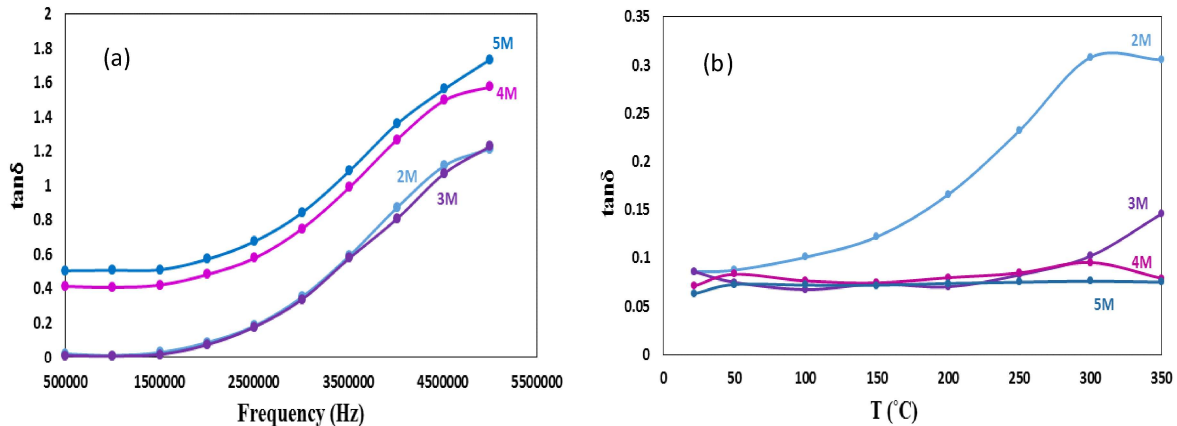


FIG. 5. Variation of the dielectric loss tangent $\tan \delta$ (a) as a function of frequency at room temperature and (b) as a function of temperature at 2 MHz.

The increase of the temperature facilitates the segmental mobility, thus easing the dielectric polarization and increases the dielectric constants [10], as shown in Figs. 3 (b) and 4 (b). The peaks obtained are explained by Bunget et al. [17], where at a certain temperature, the decrease in relaxation polarization overcomes the increase in the number of polarons, so that the dielectric constants begin to decrease.

In Fig. 5 (a), it is obvious that the loss tangent increases with the increase of frequency and the lowest values are obtained in the 2M and 3M samples. This is caused by the presence of leakage loss aside with the polarization loss [18]; whereas the increase of the loss tangent with the increase of temperature, as shown in Fig. 5 (b), is attributed to the perturbation in the phonon system caused by the applied electric field, where the energy transferred to the phonon is dissipated in the form of heat [19].

The impact of the frequency on the ac conductivity is shown in Fig. 6 (a). The ac conductivity increases with the increase of frequency and this increase is the largest in the 2M sample. This lift is an indicator of the presence of small polaron conduction. On the other hand, the increase of the ac conductivity with temperature shown in Fig. 6 (b) could be attributed to the increase of the number of polarons with temperature [18] and the peak

obtained might be a result of the flipping of conduction mechanisms at a certain temperature. The irregular behavior of the dielectric parameters above the temperature of 300°C for samples at molarities 2M and 4M of NaOH can be attributed to the ferroelectric behavior of these samples. This behavior can be explained by the existence of the yttrium iron perovskite ($YFeO_3$), where a ferroelectric phase transition can take place at high temperatures [20].

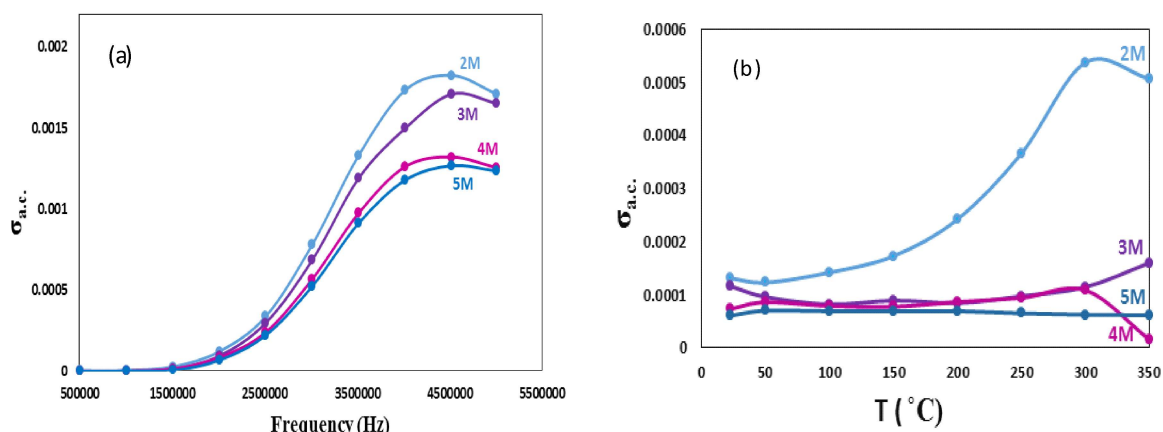


FIG. 6. Variation of the ac conductivity σ_{ac} (a) as a function of frequency at room temperature and (b) as a function of temperature at 2 MHz.

Conclusion

In this work, we prepared YIG powders by co-precipitation method from chlorides of Iron and Yttrium. Dielectric properties of the prepared samples were studied over a wide range of frequencies and temperatures for different values of molarity of NaOH ($M=2, 3, 4$ and 5). The change in the behavior of the dielectric constants as a function of frequency and temperature can be interpreted in terms of polarization and segmental mobility, respectively, while the variation of the ac conductivity can be interpreted in terms of polaron conduction. It can be seen that the highest dielectric constants and highest ac

conductivity values were obtained for the 2M sample. The dielectric properties of YIG can be manipulated by changing the molarity of NaOH, making it suitable for a wider range of applications, such as bio-antennas.

Acknowledgement

Most of this work was done in the Materials Science Laboratory, Physics Department, Faculty of Science, Beirut Arab University, Beirut, Lebanon; in collaboration with the Physics Department, Lebanese University, Beirut, Lebanon.

References

- [1] Mergen, A. and Qureshi, A., *J. Alloy Compd.*, 478 (2009) 741.
- [2] Tsay, C., Lin, C., Liu, K., Lin, I., Hu, L. and Yeh, T., *J. Magn. Magn. Mater.*, 239 (2002) 490.
- [3] Wang, C., Liang, X., Zhang, Y., Zhu, Y., Qin, J., Gao, Y., Peng, B., Sun, N. and Bi, L., *Phys. Rev. B*, 96 (2017) 224403.
- [4] Ramesh, T., Rao, G., Suneetha, T., Shinde, R., Rajendar, V., Murthy, S. and Kumar, S., *Springer Science+Business Media*, 31 (2017) 1899.
- [5] Ahmad, H., Rejab, N., Ahmad, Z., Ain, M., Othman, M., Faiz, W. and Ali, W., *AIP Conf. Proc.*, 2068 (2019).

- [6] Jang, M., Roh, I., Park, J., Kang, C., Choi, W., Baek, S., Park, S., Yoo, J. and Lee, K., *J. Alloy Compd.*, 711 (2017) 693.
- [7] Barron-Lopez, J., Hernandez-Cruz, L., De-Jesus, F., Bolarin-Miro, A., Alvarez, G. and Montiel, H., *J. Phys.: Conf. Ser.*, 1221 (2019) 012017.
- [8] Hosseinzadeh, S., Elahi, P., Behboudnia, M., Sheikhi, M. and Mohseni, S., *Mod. Phys. Lett. B*, 33 (2019) 1950100.
- [9] Hosseinzadeh, S., Behboudnia, M., Jamilpanah, L., Sheikhi, M., Mohajerani, E., Tian, K., Tiwari, A., Elahi, P. and Mohseni, S., *J. Magn. Magn. Mater.*, 476 (2019) 355.
- [10] Qureshi, A., Mergen, A. and Bekir, A., *J. Phys.: Conf. Ser.*, 153 (2009) 012061.
- [11] Mergen, A. and Qureshi, A., *J. Alloy Compd.*, 478 (2009) 741.
- [12] Praveena, K., Sdhana, K., Srinath, S. and Murthy, S., *Mater. Res. Innov.*, 18 (1) (2014) 69.
- [13] Wan, A., Mohamadarif, O., Mohd, A., Norazharuddin, A. and Zainal, A., *J. Eur. Ceram. Soc.*, 33 (2013) 1317.
- [14] Wei, Z., Cuijing, G., Rongjin, J., Caixiang, F. and Yanwei, Z., *Mater. Chem. Phys.*, 125 (2011) 646.
- [15] Venkata, M., Leng, F., Wen-Chin, L. and Budaraju, M., *J. Adv. Ceram.*, 4 (2013) 46.
- [16] Singh, A., Goel, T., Mendiratta, R., Thakur, O. and Prakash, C., *J. Appl. Phys.*, 91 (2002) 6626.
- [17] Bunget, I. and Popescu, M., "Physics of Solid Dielectrics", (Elsevier, Amsterdam, 1984).
- [18] Lin, Y., Yang, H., Zhu and Wang, F., *J. Optoelectron. Adv. M.*, 4 (2010) 509.
- [19] Zhao, H., Zhou, J., Bai, Y., Gui, Z. and Li, L., *J. Magn. Magn. Mater.*, 280 (2004) 208.
- [20] Mingya, S., Chenyang, Z., Tingsong, Z., Lin, Y., Lei, G., Hongming, Y. and Shouhua, F., *App. Phys. Lett.*, 102 (2013) 062903.

Effect of the Polyamide Type on the Physical Properties of Layered Polyaniline Composite Films

D. Mezdour^a and M. Tabellout^b

^a *Laboratoire D'études des Matériaux, Mohamed Seddik Benyahia University, Jijel 18000, Algeria.*

^b *Institut des Molécules et Matériaux du Mans, Le Mans Université, Le Mans 72085, France.*

Doi : <https://doi.org/10.47011/13.3.6>

Received on: 08/08/2019;

Accepted on: 12/12/2019

Abstract: The present work deals with the investigation of the dielectric properties of layered polyamide/polyaniline films and their correlation to the microstructure. A thin polyaniline (PANI) layer was polymerized in the subsurface of polyamide films. The dielectric relaxation spectroscopy was used to compare the electrical behaviour of flexible polyamide 6 (PA6) and polyamide 12 (PA12) surfaces loaded with PANI nanoparticles, while the roughness was investigated by the contact angle technique. Relatively high dielectric constants were recorded for PA12/PANI films compared to PA6/PANI ones due to the hydrophobic nature of the PA12 matrix. This also explained the wettability enhancement observed for PA12/PANI films up to 12 wt.% of aniline absorbed concentration, while PA6/PANI films needed no more than 9 wt.% to reach maximum wettability. This behavior was in good correlation with the microstructure of the films. SEM micrographs showed uniform surfaces for both films formed above these respective concentrations, where wettability started to decrease. The films of PA/PANI seemed to be good candidates as dielectric layers in flexible electronics.

Keywords: Polymer, Polyamide, Polyaniline, Dielectric constant, Optical gap.

PACS: 78.20.-ei, 78.20.-c, 68.60.-p, 82.35.Lr.

Introduction

Conducting polymers have received considerable attention in the fields of both nanoscience and nanotechnology [1,2]. Compared to metals, intrinsically conducting polymers are light and flexible and can not only reflect, but also absorb, electromagnetic radiations.

Polyaniline (PANI) has attracted considerable interest as an air-stable conducting polymer. Its reversible redox behavior is useful for supercapacitor, gas sensor, pH sensor and fuel cell applications. Frequency-dependent conductivity of PANI is involved in

electromagnetic interference (EMI) shielding application. PANI is also used as an antistatic coating and corrosion inhibitor, due to its high chemical stability, nontoxicity, good process ability and stable intrinsic redox state derived from the imine groups of the PANI chain. It is possible to tune structures of PANI within a wide domain of shape, size and crystal structure.

Incorporation of conducting polymer into a host polymer substrate forming a blend, composite or inter-penetrated bulk network has been widely used in a manner to combine

electrical conductivity with desirable physical properties of polymers [3,4].

At present, a renewed interest is directed to thermoplastic polymers which present a liquid phase at high temperature. They soften by heating and yield solid materials after cooling, allowing recycling. Considering annual volume production, the number of different polymers and variety of applications, the polyamide family is the most important one [5]. Polyamide (PA), commonly known as Nylon, is the largest engineering thermoplastic material. It finds major usage in several application segments, which the three notable ones are: automobile, electronic and packaging applications.

Many research studies have been reported on Polyamide/polyaniline systems. These composite materials find applications in various fields as antistatic films [6,7], membranes [8,9], nanowires for MEMs [10], ammonia sensors [11, 12], anti-corrosion coatings [13,14], wave absorbers [15], among many others. Few works were dedicated to polyamide 12/PANI composites.

In this study, flexible polyamide 6 (PA6) - and polyamide 12 (PA12) - based films are compared in terms of dielectric permittivity, wettability, microstructure and optical properties in order to identify their potential uses in flexible electronics.

Experimental Part

Depending on the swelling time of polyamide films in aniline, different concentrations of polyaniline were obtained by oxidative

polymerization in the subsurface using an aqueous solution of ammonium persulphate and hydrochloric acid. The obtained green films were then rinsed in n-Hexane to remove the by-products and dried at 65 °C for 24 h.

The dielectric properties were investigated by dielectric relaxation spectroscopy using a Novoconcontrol broadband dielectric spectrometer over a wide range of frequencies (from 0.1 to 10^6 Hz). The roughness of the surface was investigated by the contact angle technique based on the measurement of the contact angle formed by a drop of water on the surface of the samples. The morphology was examined by SEM microscopy. UV-vis spectroscopy was used to study the optical properties of the films.

Results and Discussion

Dielectric Properties

Fig. 1 shows a comparison between PA6 and PA12 composite films in terms of dielectric constant. At room temperature, the dielectric constant increases with increasing PANI. It doesn't exceed 60 at 0.1 Hz for the PA6 composite film obtained with 10 wt. % of aniline (Fig.1-a). It reaches values up to $2 \cdot 10^5$ at 0.1 Hz for the PA12 composite film obtained with 12.68 wt. % of aniline (Fig.1-b). At 0.1 Hz, a high value of about 4000 was also registered at 30 °C for a PA6 based film obtained with 4 wt. % of aniline, as can be seen in Fig. 2. However, this result is not observed for higher concentrations or other temperatures.

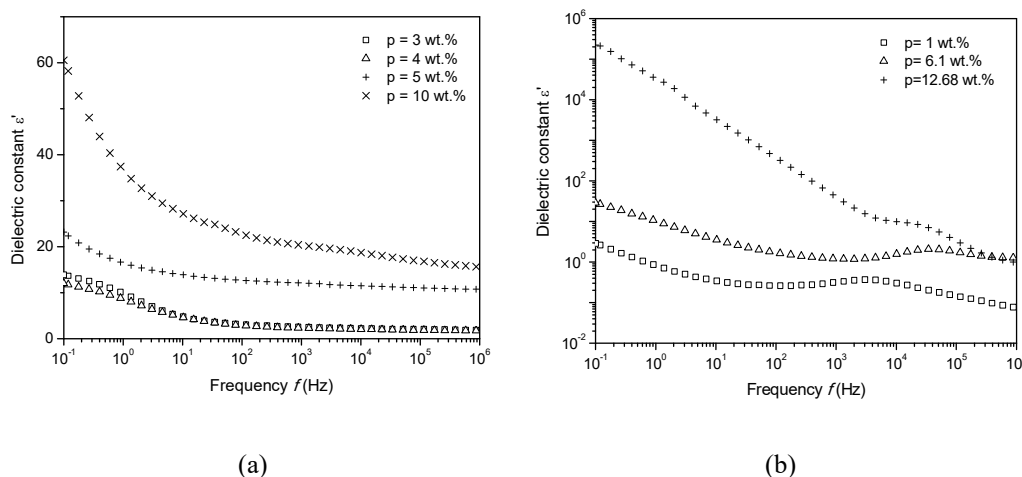


FIG. 1. Log plot of dielectric constant ϵ' versus frequency for PA6 (a) and PA12 (b) composite films.

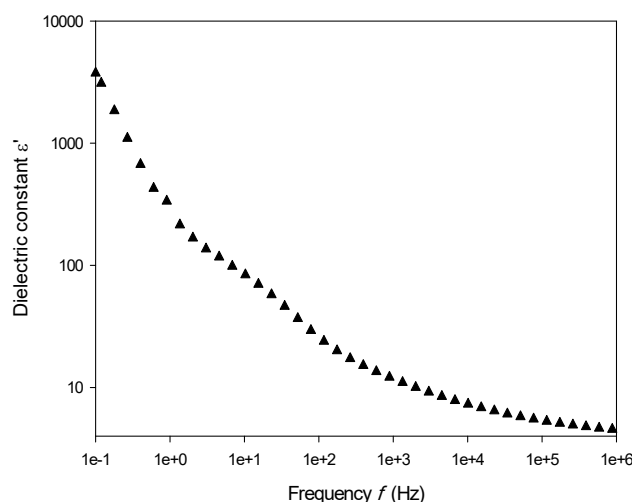


FIG. 2. Log plot *versus* frequency of dielectric constant ϵ' at 30 °C for a PA6 film made with 4 wt. % of aniline.

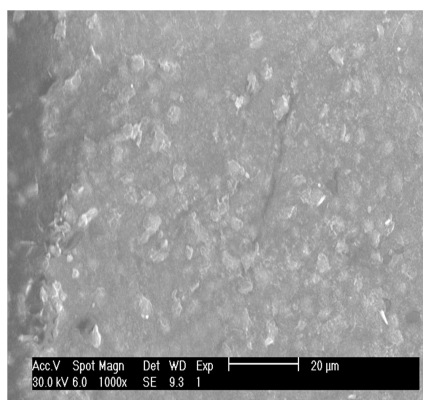
A first theory attributed the high permittivity at low frequency to the polarization of counterion carriers associated with the fixed surface charge of particles [16,17], whereas later work linked it rather to the polarization of the double electric layer by electro kinetic processes [18]. The higher value of permittivity observed for PA12 is ascribed to its hydrophobic nature which prevents aniline from infiltrating, thus from becoming polymerized uniformly and clustering, hence causing the existence of a larger number of minicapacitors consisting of insulating PA12 and dispersed conductive particles of PANI than in PA6 composites.

Morphology

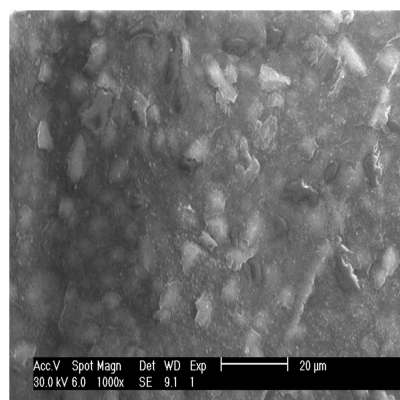
It should be noted that the polymerization process in PA12 films lasts longer. Indeed, the green color, characteristic of polyaniline formation appears for longer polymerization times reflecting their poor processing. This is

confirmed by SEM micrographs of PA12 films containing different concentrations of PANI. The images are not as clear as those of PA6 films, probably because of the low surface conductivity of PA12 films.

Fig. 3 shows the morphology of the composite films as a function of PANI concentration. It is clear that structure is related to matrix type. While the PA6 films exhibit a granular structure, the PA12 films show an interpenetrating fibrous network. The PA6 surface shows well dispersed small particles of PANI with irregular shape at 9 wt. % (Fig. 3-a). The size of these particles increases at 10 wt. %, leading to a totally covered surface (Fig. 3-b). One can observe the conductive pathways meandering through the insulating PA12 matrix for both concentrations (c, d). However, at 10 wt. % of aniline, the PA12 structure is clearly porous.



(a)



(b)

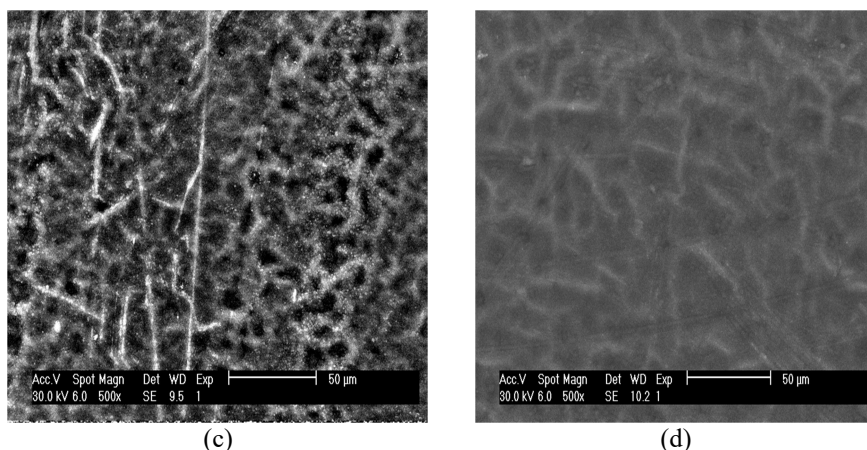


FIG. 3. SEM micrographs of PA6- (a, b) and PA12- (c, d) based composites made with different concentrations of aniline: (a) 9 wt. %, (b) 10 wt. % and (d) 12.68 wt. %.

Wettability

The contact angle measurements made on PA6 and PA12 films gave the curves in Fig. 4. Despite fluctuations in the measurement method, the contact angle for the PA6-Water system (Fig. 4-a) decreased with the increase in aniline concentration up to 9 wt. %, reflecting an improvement in film wettability. This is due to surface roughness that increases with the growth of PANI clusters. Beyond this concentration, the contact angle increases with increasing aniline concentrations. Indeed, the roughness of the

films decreases due to the surface uniformity verified by the SEM images showing surfaces totally covered by PANI. For PA12 films (Fig. 4-b), through angle fluctuations, it is possible to detect a gradual decrease in the contact angle *versus* the aniline concentration up to an approximate value of 12 wt. %. This concentration, from which the contact angle begins to increase, corresponds to the quantity required to cover the surface film by PANI, as shown in Fig. 3-d.

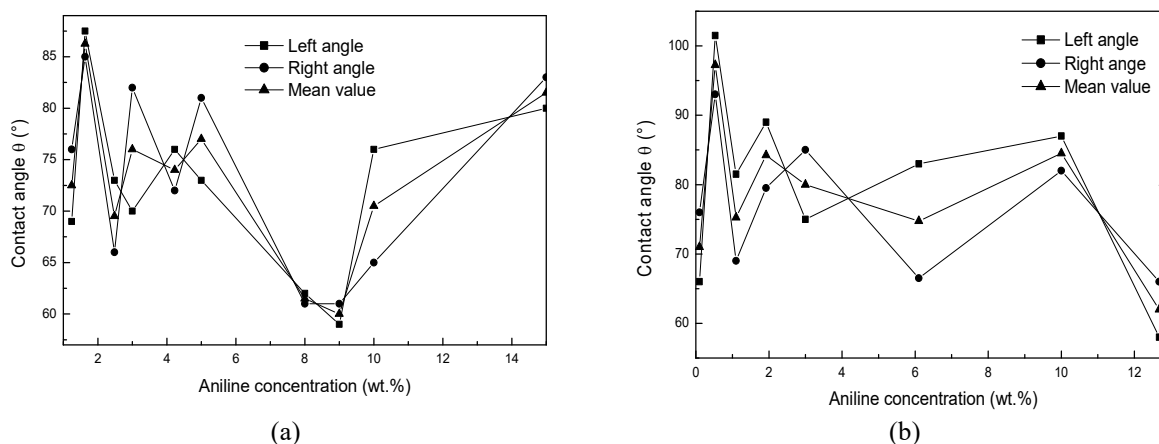


FIG. 4. Contact angles formed by a drop of water on the surface of PA composite films *versus* the initial aniline content: (a) PA6, (b) PA12.

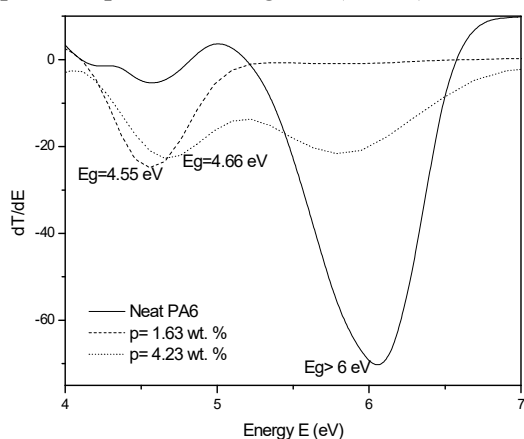
$$\text{Mean.value} = \frac{\text{Left} + \text{Right}}{2}, \text{ where Left and Right refer to left and right contact angle, respectively.}$$

A similar study was conducted on composite films of Nafion/carbon nanotubes [19]. The authors observed a decrease of the contact angle with the decrease of the Nafion content (increase in the carbon nanotubes content). Beyond a certain concentration of Nafion, hydrophobicity

increases again. This phenomenon was explained in terms of air cavities (due to the surface roughness). The wettability of the films was controlled by simply varying the content ratio of Nafion to Carbon nanotubes. This is in good agreement with our observations.

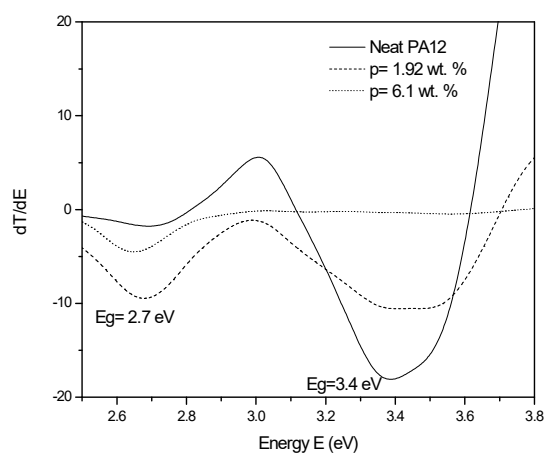
Optical Properties

The optical gap of the films was deduced from the transmittance spectra obtained by the UV-vis spectroscopy technique. A more appropriate procedure for determination of bandgap while dealing with nanomaterials involves the derivative of the transmission with respect to photon energies (dT/dE). In the



(a)

derivative method, as the photon energy approaches that of bandgap, the derivative should exhibit a minimum (spike toward negative infinity at $E = E_g$). The plot of the transmittance derivative *versus* energy for both types of films is illustrated in Fig. 5. Comparable and relatively low concentrations of aniline were investigated.



(b)

FIG. 5. Evolution of the optical gap E_g *versus* aniline concentration for the PA6 (a) and PA12 (b) composite films.

As illustrated in Fig. 5-a, the characteristic peak of PA6 located at 6 eV and corresponding to the gap energy E_g , disappears to the benefit of an increasing peak, related to PANI and located at 4.55 eV for 4.23 wt. %. The decrease of E_g is due to the growth of PANI clusters in the subsurface of the films. Increasing PANI concentration in PA12 films (Fig. 5-b) leads to a slight decrease of E_g compared to the PA6 matrix case. However, determined E_g values are lower, revealing better semi-conductive properties comparable to Pure PANI (2.7 eV) [20].

Conclusion

In this study, physical properties of bi-layered films of Polyamide and PANI are investigated regarding matrix type. A thin polyaniline (PANI) layer was polymerized in the subsurface of polyamide films using ammonium persulphate as an oxidant and hydrochloric acid as a dopant.

A novocontrol broadband spectrometer was used to investigate the dielectric properties of the prepared samples. High values of dielectric constant are obtained for both PA12 and PA6 composites, but at a low extent for PA6 composites, allowing their use as high-k dielectrics at low frequency.

Through contact angle measurements, it has been shown that the wettability of the films is affected by the growing size of PANI clusters. Better wettability is observed for PA12-based films. This is probably due to the hydrophobic nature of PA12 which delays the polymerization of aniline and PANI cluster growth. This property is interesting in multilayer devices, such as OLEDs or PV cells. A good correlation is found between wettability and microstructure through the surface roughness related to cluster size.

PA12 composites also show better semi-conductive properties than PA6 ones. Their optical gap is equal to the known gap of PANI (2.7 eV). This is also ascribed to hydrophobicity of the PA12 matrix, where PANI is confined in a thinner surface layer, facilitating its identification.

Based on the above observations, we conclude that the matrix type strongly affects the physical properties of the resulting composite and plays a major role in determining the proper application. With higher carbon atom number, the PA12 matrix seems to offer high potential in optoelectronic applications.

References

- [1] MacDiarmid, A.G., *Synth. Met.*, 125 (2002) 11.
- [2] Heeger, A.J., *Synth. Met.*, 125 (2002) 23.
- [3] Andreatta, A., Heeger, A.J. and Smith, P., *Polym. Commun.*, 31 (1990) 275.
- [4] Im, S.S. and Byun, S.W., *J. Appl. Polym. Sci.*, 51 (1994) 1221.
- [5] Guerin, B., *Techniques de l'Ingénieur*, (1994) a3360.
- [6] Araujo, J., Adamo, C.B. and De Paoli, M.A., *Chem. Eng. J.*, 174 (1) (2011) 425-31.
- [7] Yadav, R., Tirumali, M., Wang, X., Naebe, M. and Kandasubramanian, B., *Defence Technology*, 16 (1) (2020) 107.
- [8] Banimahd Keivani, M., Aghaie, M., Ansari, R., Zarel, K. and Aghaie, H., *J. Phys. & Theo. Chem.*, I.A.U. Iran, 3(4) (2007) 263.
- [9] Fazullin, D.D., Mavrin, G.V., Shaikhiev, I.G. and Haritonova, E.A., *Petrol. Chem.*, 56 (5) (2016) 454.
- [10] Hong, K.H. and Kang, T.J., *J. Appl. Polym. Sci.*, 99 (3) (2006) 1277.
- [11] Hong, K.H., Oh, K.W. and Kang, T.J., *J. Appl. Polym. Sci.*, 92 (1) (2004) 37.
- [12] Gao, L., Yin, C., Luo, Y. and Duan, G., *Nanomaterials*, 9 (4) (2019) 493.
- [13] Ansari, R. and Alikhani, A.H., *J.C.T. Research*, 6 (2) (2009) 221.
- [14] Kausar, A., *Polymer-Plastics Technology and Materials*, 59 (6) (2020) 658.
- [15] Joseph, N., Varghese, J. and Sebastian, M.T., *Polymer Journal*, 49 (2017) 391.
- [16] Schwan, H.P., Schwarz, G., Maczuz, J. and Pauly, H., *J. Phys. Chem.*, 66 (1962) 2626.
- [17] Schwarz, G., *J. Phys. Chem.*, 66 (1962) 2636.
- [18] Dukhin, S.S., Shilov, V.N., "Dielectric Phenomena and the Double Layer in Disperse Systems and Polyelectrolytes", (John Wiley and Sons, New York, 1974).
- [19] Luo, C., Zuo, X., Wang, L., Wang, E., Song, S., Wang, J., Wang, J., Fan, C. and Cao, Y., *Nano Lett.*, 8 (12) (2008) 4454.
- [20] Sharma, I.D., Saini, P.K. and Sharma, V.K., *Indian J. Eng. Mater. Sci.*, 20 (2013) 145.

Graphene and Related 2D Materials for Desalination: A Review of Recent Patents

M.W. Aqra^a and A.A. Ramanathan^b

^a *Technical Support Dept., National Center for Research and Development, Amman-11941, Jordan.*

^b *The University of Jordan, Amman-11942, Jordan.*

Doi : <https://doi.org/10.47011/13.3.7>

Received on: 08/08/2019;

Accepted on: 12/03/2020

Abstract: The growing population and energy demand, coupled with the depleting fresh water resources resulted in great progress in sea water desalination (SWD) technologies. Nanopores of 2D materials, like graphene and its structural analogs, are the latest innovations in membrane technology for SWD. The performance of these novel atomically thin nanopores, as seen from various experimental and theoretical studies, is highly encouraging with reports of water permeability 2-3 orders of magnitude greater than the conventional reverse osmosis (RO). The potential for high efficiency and the low energy requirements of these nanopores for desalination led to tremendous efforts in fabrication and commercialization. We present here a review of the very recent patents associated with the preparation of these nanopores, the process and the efficiency of SWD.

Keywords: 2D nanopores, Graphene, Membrane, Patents, Desalination.

Introduction

It is expected that by 2030, more than 15% of the world population will be forced to turn to seawater to meet their needs for fresh or brackish water. At present, around 150 countries rely on desalination and around 80 million m³ of drinking water is being produced daily by more than 17,000 desalination plants, with 50% of them utilizing sea water as the source [1]. The desalination process needs to be perfected and made more energy-efficient, cost effective, environment friendly and sustainable [2-5]. The rapid and innovative advancements in nanotechnology during the past decade and the quick strides taken in nanoscale fabrication have given rise to the discovery of nanopores of atomically thin membranes of graphene and other 2D materials that can filter molecules and selectively transport ions in nano-channels for various applications in energy, sensing, medicine and desalination [6-10].

Nano-filtration (NF) and reverse osmosis (RO) that use filters are limited by the low permeability of the filters. Even though today RO is the most established method and the efficiency of RO is thrice what it was two decades ago, it is a slow diffusion process whereas nanopores use a sieving method and fast water transport in an efficient manner with high rates of salt rejection [11-18]. For efficient desalination, a membrane must demonstrate a high salt rejection rate along with a high water flux. Highly permeable membranes can be achieved by engineering the right pore size, chemical functionalities and other surface characteristics [13-15, 19-20]. Nanoporous graphene (NPG) has a separation rate of two-three orders of magnitude higher than diffusive RO, as shown by the molecular dynamics (MD) studies [13, 14]. In addition, the experimental study of [15] for single-layer graphene shows

almost 100% salt rejection and rapid water fluxes in the order of 10^6 g/m² s at 40°C. Moreover, since the desalination process with nanopores does not require high pressures like RO, the energy used is very much less and makes them extremely cost effective, especially as we know that in RO, the high energy consumption accounts for half the total cost of operation. These results confirm NPG as a desalination device with a very high potential. Further, first principles' studies of Molybdenum disulphide (MoS₂) give 70% higher water fluxes than NPG and allow for strain tuning of the membrane [15, 16]. Again, simulation studies of boron nitride (BN) show higher efficiency than NPG and superior water flow and salt rejection performance [11, 12, 17]. The insights obtained by theoretical findings regards the optimum pore size, functionality and material design must be translated into practice for fabrication and manufacture of optimal desalination devices. The recent years have seen several innovative techniques of nanoporous membrane preparation and patents in the various processes, methods and materials for desalination.

Water is a scarce resource and SWD is the most sustainable and attractive option for water management. In this context, the past decade has seen a tremendous increase in research on the use of nanopores of 2D materials, like graphene and transition metal dichalcogenides, for energy-efficient desalination technologies. Now, as this novel technology is ripe for commercial implementation, it is important to bring to the attention of the scientific community the recent patents on this valuable desalination technology. In addition to being energy-efficient, nanopores offer water permeability 2-3 orders of magnitude greater than the conventional reverse osmosis. Since this is a rapidly developing field with exciting new scientific findings, the focus of the

present review article is on the recent (since 5 years) patents in this new and exciting field of graphene and related 2D material nanopores. The immense possibilities and success in water desalination using this novel technology is highlighted with some interesting patents and discussions of the various aspects concerning the preparation, process and fabrication of nanoporous optimal desalination devices. The paper is organized under the headings: Introduction, Structure of Nanopores and Patents Therein, Process, Performance and Effectiveness of Nanopores and Challenges and Outlook.

Structure of Nanopores and Patents Therein

Patents [21-23] deal with various ways of making nanoporous membranes of graphene and related 2D materials. In the patent [21], graphene separation membrane with a plurality of grain boundaries on a polymer support has been prepared for separation of ions in water (desalination) and in gases. The polymer support may include polysulfone, polyethersulfone, polyimide, polyamide, polyetherimide, polyacrylonitrile, polyethylene, polycarbonate, polytetrafluoroethylene, polypropylene or polyvinylidene fluoride. The separation membranes can be based on graphene or transition metal dichalcogenides (TMDs); for example, MoS₂, NbS₂, NbSe₂, TaS₂, ... etc. and other 2D materials, like BN. The graphene membrane may be made by a variety of methods, like liquid phase method, vapor phase method, polymer method and other methods that can grow the grain boundaries, as shown in Fig. 1(a). The pore size and spacing in the grain boundaries and the channels can be different in the layers to increase the separation selectivity of particular substances, as seen in Fig. 1(b).

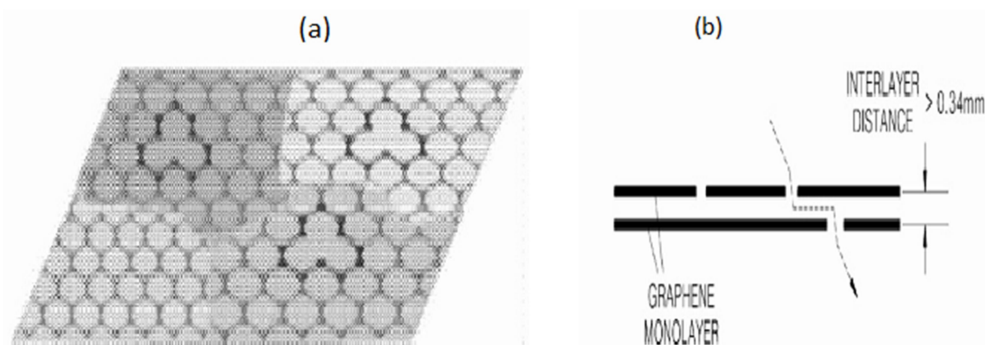


FIG. 1. Schematic illustration of different forms of grain boundaries and pores in (a) graphene layer (b) cross-section of a bilayer [21].

The pores can have a width of about 0.335 nm to 100 nm. The pore size and channels can be controlled by adjustments to the graphene growth rate or by changing the carbon supply source to methane or hydrocarbon-based organic polymers. These pores can be made so small as

to selectively pass only water molecules and block the hydrated salt ions in desalination. In addition to pores arising from grain boundaries, fine pores could be formed on the graphene membrane as a result of defects near 5- or 7-membered rings, as depicted in Fig. 2.

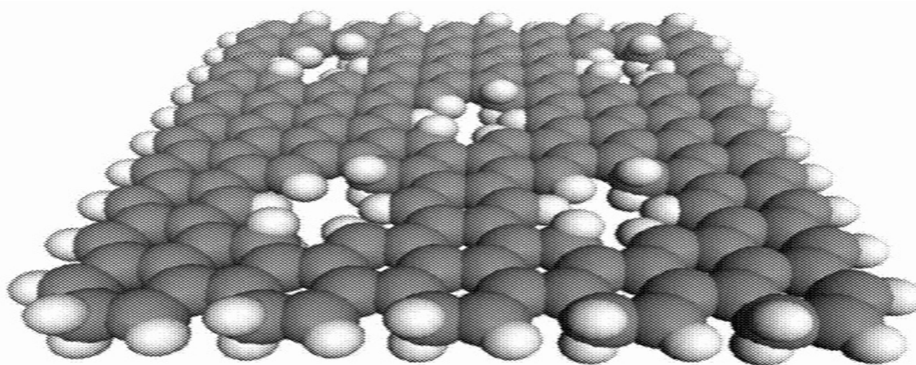


FIG. 2. Schematic illustration of structure of graphene monolayer including defects [21].

The procedure and description above of forming nanopores [21] is not exclusive to graphene, but also applies to the other 2D materials; for example, MoS_2 and BN.

It is difficult to remove and transfer atomically thin layers of 2D materials containing nanopores from the growth substrate, as this can give rise to tear and conformity problems. This issue is addressed by Sinsabaugh et al. (2015).

The process involves manipulation of the 2D materials, such as graphene, by first providing a support layer while it is still adhered to the growth substrate, then, second releasing the substrate from the 2D material, resulting in a 2D material attached to the support layer. Fig. 3 illustrates this 3-step process; the operations of forming and depositing a support layer and removal of the substrate.

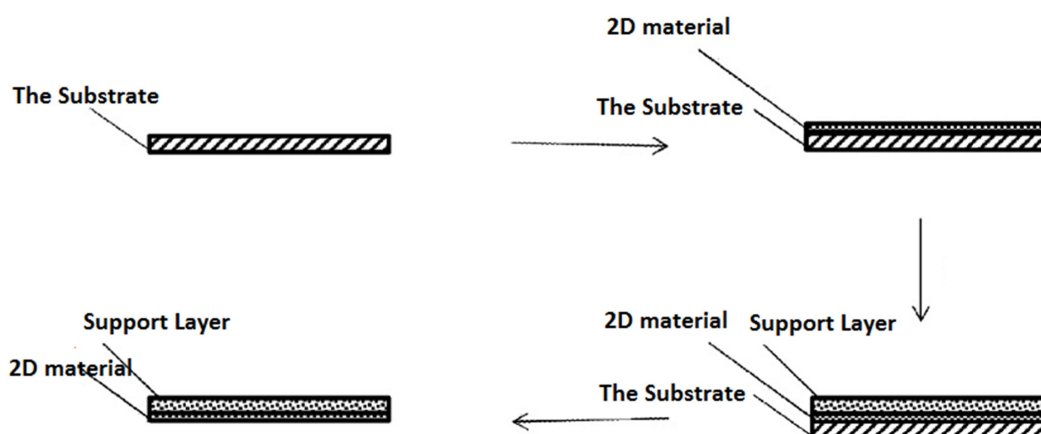


FIG. 3. Schematic illustration of the process of formation on substrate, deposition of support layer and removal of substrate [22].

The substrate can be a metal, like Cu or Ni, and the removal of the substrate is achieved by etching with a suitable etchant, like ammonium persulphate. The method uses a non-sacrificial porous support layer that can contain a plurality of pores with a pore size gradient in some embodiments. Such an embodiment has a smaller pore size in the supporting layer close to

the 2D material surface compared to the opposite end. This feature can be achieved by electro-spinning of fibres with a density that is higher near the 2D material surface and lower further away from the 2D surface. Various chemical and physical techniques for perforating graphene or the 2D material can be employed, like particle bombardment, chemical oxidation, lithographic

patterning or a combination of these [24]. This can be done while it is adhered to the growth substrate or after removal of growth substrate and while it is attached to the supporting layer.

The most recent invention is that of Stoltenburg et al. (2017). The method consists of making a composite film of an atomically thin material (such as graphene) and a polymer layer; bombarding the same to create a plurality of pores in at least the graphene layer. The atomically thin material could be any of the following: a few layers of graphene, molybdenum disulfide, boron nitride, hexagonal

boron nitride, niobium diselenide, silicene or germanene. The best mode for the process of making and etching the nanoporous membrane and the execution of the invention is illustrated in Fig. 4. The composite film consists of an atomically thin layer of 2D material and a polymer film. A hot press manufacturing process could be used to make the composite film. The polymer film is polycarbonate with a thickness ranging from 25-250 microns. Materials, like polyester, polypropylene, polyimide, polymethyl methacrylate or polyvinylidene fluoride, could be used for the polymer film.

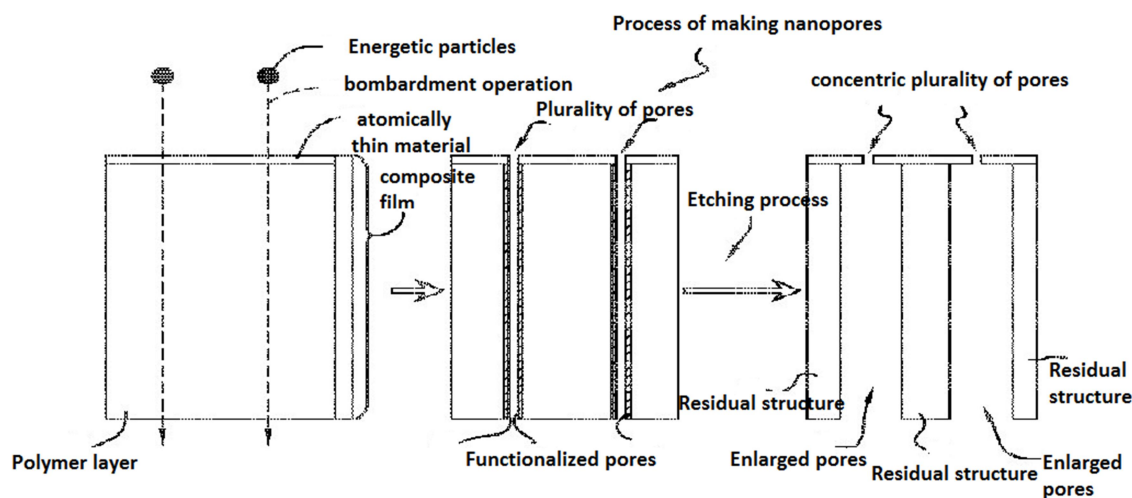


FIG. 4. A schematic diagram of a process for making a nanoporous membrane with an initially non-porous polymer film [23].

The energetic particles may be electrons, neutrons, ions, ion clusters or similar particles that are sufficiently energetic to traverse the composite film. Typical energies > 1 MeV/micron thickness are directed at the composite film during the bombardment operation. Another aspect is the selection of the energetic particles to form a plurality of pores in the composite film, such that the chemical nature of polymer layer is changed and the functionalizing of the pore occurs. Upon completion of the bombardment process, the composite film undergoes the etching process. The entire film is immersed in an appropriate etching fluid, which depends on the type of polymer film used. For polycarbonate, a solution of NaOH is used for a predetermined length of time. During the etching process, the etchant attacks the chemical functionalizing of the polymer film in the pores to remove the chemical functionalized area and form enlarged pores in the polymer film. Depending upon the extent of chemical functionalization and the

etching parameters, the pore size can be controlled and it may range from 10-1000 nm. A residual polymer structure is formed as a result of the etching process. The end results of the etching process provide a plurality of pores with a size ranging from 0.5 to 10 nm in graphene that are concentrically aligned with the enlarged pores. Thus, the nanoporous membrane (active layer) has a one-to-one mapping of the holes with the polymer layer (substrate). An alternate method of producing a nanoporous membrane is depicted in Fig. 5. The method is similar to the above described method, except that the polymer film is already porous with enlarged pores. The composite film (which consists of the atomically thin layer and polymer layer) is the same as the composite film in the previous method and has the same characteristics. The energetic particles during the bombarding process are selected such that there is no chemical functionalization of the polymer film and it is inert to pore enlargement. The process of bombardment creates a plurality of pores in graphene or other atomically thin

material that may or may not be concentric with the enlarged polymer pores. Further, it may form pores that extend partially into the polymer layer to create a cavity. The process may also create

pores that extend all the way through the graphene and the polymer layer, i.e., the composite layer.

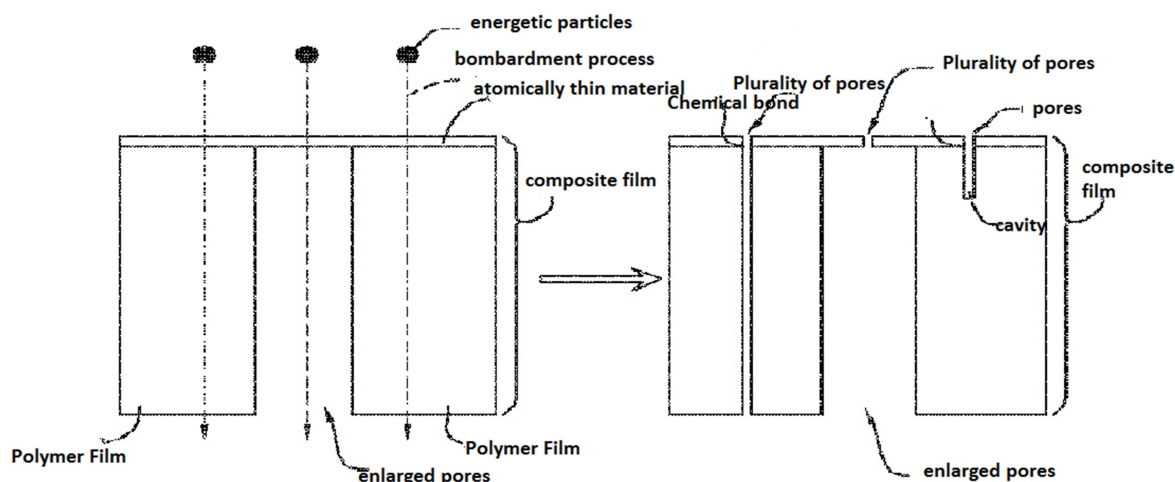


FIG. 5. Schematic diagram of a process for making a nanoporous membrane with an initially porous polymer film [23].

Furthermore, a chemical bond may be formed between the graphene and polymer layer that will secure it and strengthen the composite film and support the graphene membrane. As a result, there can be an alignment of the pores of size 0.5-10 nm with the enlarged pores to provide higher permeability. This method has the advantage that the particles for bombardment can be different from those needed to create tracks in the polymer film, thereby giving more flexibility in forming the composite film, whereas the advantage of the previous method (Fig. 4) allows for simultaneous creation of the holes in both graphene and the polymer film that are one – to – one and are concentric, thereby considerably increasing permeability of the composite film and manufacturability. Processing active layer (graphene) and support layer (polymer film) simultaneously is easier and more scalable. Having discussed the various types of nanopores and the patents involved in making these nanoporous membranes, the application to desalination will be discussed in the next section.

Process, Performance and Effectiveness of Nanopores and Patents

Several membrane- and pressure-driven technologies, like RO, NF, Ultrafiltration (UF) and Microfiltration (MF), are in use at present [3, 25, 26]. 19% of the world has RO installations [27] and it is the conventional method in use. RO requires high pressures and the energy consumption costs equal half the total cost; the desalination of 1 m³ of seawater requires 3.4 kWh of energy at 6.5 MPa [28, 29]. Seawater predominantly contains Na⁺ (Sodium) and Cl⁻ (Chlorine) ions and has an average salinity of 3.5% (35 g/L) of dissolved salts. Typical values of the various ions present in the Arabian Gulf seawater in ppm (parts per million) are shown in Table 1. Moderate amounts of SO₄²⁻, Mg²⁺, K⁺ and Ca²⁺ ions are also present. The table also shows the radii of the hydrated ions for the main components from references [30, 31]. The mesh size has an inverse relation to the cost, so an estimation of the size of the hydrated ions in seawater is very useful.

TABLE 1. Arabian Gulf seawater composition adapted from [30, 31].

Ion	Conc. [ppm]	Ion radius [nm]	Hydrated ion radius [nm]
Na ⁺	14,161	0.098	0.360
Cl ⁻	25,491	0.181	0.270
SO ₄ ²⁻	3,594	0.147	0.300
Mg ²⁺	1,642	0.078	0.395
K ⁺	722	0.133	0.315
Ca ²⁺	530	0.106	0.348

As seen from the table, the radii of hydrated ions are almost twice the radius of the water molecule which is 0.138 nm. The knowledge of the values of the hydrated ions helps in the manufacture of membranes with optimal size and the costs of devices for desalination are reduced as a result of the lower pressures involved. The choice of the average pore size depends on the desired result of excluding a particular species and in turn is dependent on the size of the particular hydrated ion. Selection of a membrane material is based on the fact that it should be thin to maximize flow rate, chemically inert and stable and mechanically strong, with size-defined pore that provides selectivity by blocking large molecules and allowing smaller

ones. The bright future for desalination with novel nanoporous membranes, like graphene and the related materials, as well as the tremendous progress and promise shown in this direction discussed with the related patents [32-35].

In the process described by [32], a perforated graphene membrane separates sodium, chlorine and other ions from water. The apertures in the membrane are designed to pass water molecules and to not pass the smallest Na^+ , Cl^- and other relevant ions. The deionized water flowing through the graphene membrane is collected. Fig. 6 shows a notational representation of this disclosure using a perforated graphene sheet.

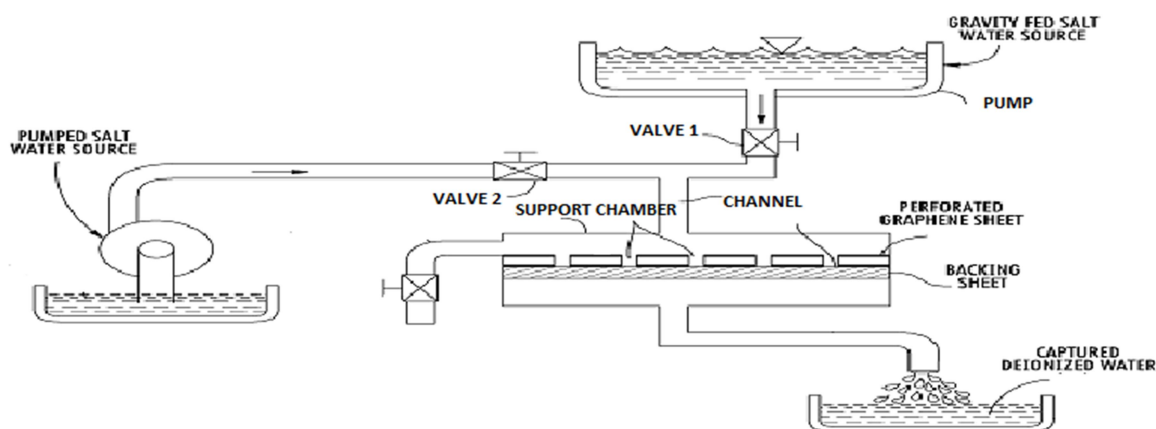


FIG. 6. A notational representation of a water filter, using a perforated graphene sheet [32].

A channel conveys the ion-laden water to a filter membrane mounted on a supporting chamber. The ion-laden water may be seawater or brackish water. The filter membrane can be wound into a spiral in a known manner. Flow impetus or pressure of the ion-laden water flowing through channel of Fig. 6 can be

provided either by gravity from a tank or from a pump. Valves 1 and 2 allow for the selection of the source of ion-laden water. In the apparatus or arrangement, the filter membrane is a perforated graphene sheet. A plan view of the same is shown in Fig. 7 below.

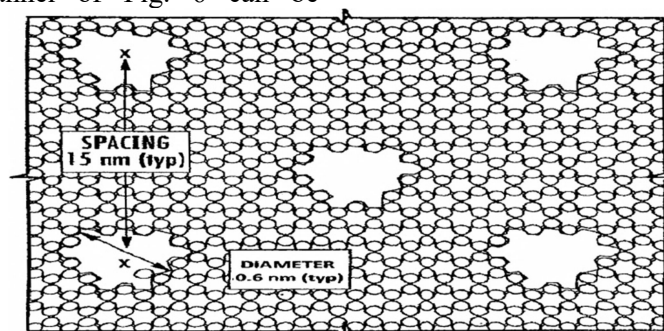


FIG. 7. A plan view of a perforated graphene sheet, showing 0.6 nm diameter perforations or apertures and interperforation dimensions [32].

The ionized water flows first through a graphene layer dimensioned with pores allowing chlorine ions to pass and then through a second graphene layer with pores designed to pass Na^+

ions. The concentrated Cl^- and Na^+ ions accumulating on the graphene layers can be separately harvested.

Mahurin et al. [34] also used nanoporous graphene for desalination. They have devised a process for the flow of salt water through a free standing graphene layer, having pores up to a size of 1 nm and with pore edges passivated by silicon. When water flows through the first planer side, the salt ions are blocked and salt free

desalinated water exits from the other side. The membrane is supported on a substrate that contains a window and the free standing graphene layer spans this window and the salt water flows only through this portion. Fig. 8 shows the single graphene layer suspended over the hole /window in the support material.

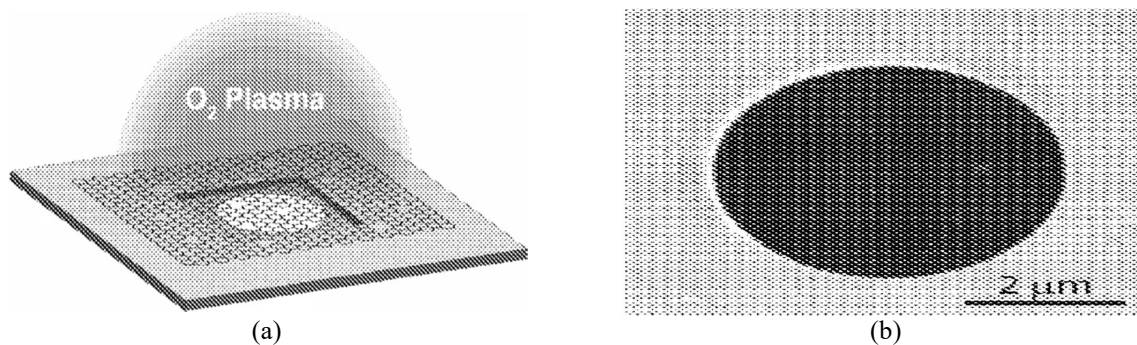


FIG. 8. (a) Schematic of single-layer graphene being subjected to oxygen plasma etch process while suspended over a hole in a support material (b) SEM image of single-layer graphene suspended over a hole in a support material [34].

Seawater contains at least one of sodium or potassium ions and at least 10 g/L of the salt species, while the removal of salts is ~ 95-99%. The membrane is disposed on the opening of the container, which is inverted to feed seawater by gravity to the first planer side, resulting in desalinated water flowing out of the second planer side. The seawater is fed continuously into the container.

Grossman et al. [33] used a variety of porous materials, including nanoporous materials for filtration, purification and/or separation applications. The materials may be thin, flexible and manufactured with a control over pore size and spatial distribution for applications in desalination. These could be a nano-structured carbon material, such as carbon nanotubes, graphite, graphene or graphene oxide. For example, the porous material could be a single layer or multiple layers of graphene arranged on a support or formed on a substrate that can be fabricated to include a plurality of pores having an average pore size of about 1 nm or less. The pores can be made to have an optimal size so as to effectively reject certain ion species, such as Na⁺ and Cl⁻ and allow the flow of other species; e.g. water molecules. Nanoporous graphene

materials having an overall porosity of 10% and containing a plurality of pores with an average pore size of about 6 Å may exhibit a water permeability of about 50 L/cm² /day/MPa to about 60 L/cm² /day/MPa, which is two to three orders of magnitude higher than known UF, NF and reverse osmosis membranes. Functionalization in addition to pore size affect the permeability of the water and the salt rejection performance of the membrane. As shown by [36], the chemical functionalization of graphene nanopores can tune and selectively reject certain solvated ions. The carbon atoms at the edge of a pore on a graphene membrane can be functionalized by hydrophilic groups-OH or hydrophobic groups-hydrogen, alkyl, aryl, ... etc. or by substituted/un-substituted amino, ... etc. The hydrophilic functionalization allows faster water flow by providing a smoother entropic landscape for the water molecules, whereas hydrophobic functionality at or near the pore edges with hydrogen may enhance salt rejection. The key performance indicators of any desalination technology are salt rejection and water flux and Fig.9 illustrates the high performance of graphene nanopores as compared to RO and other common desalination methods.

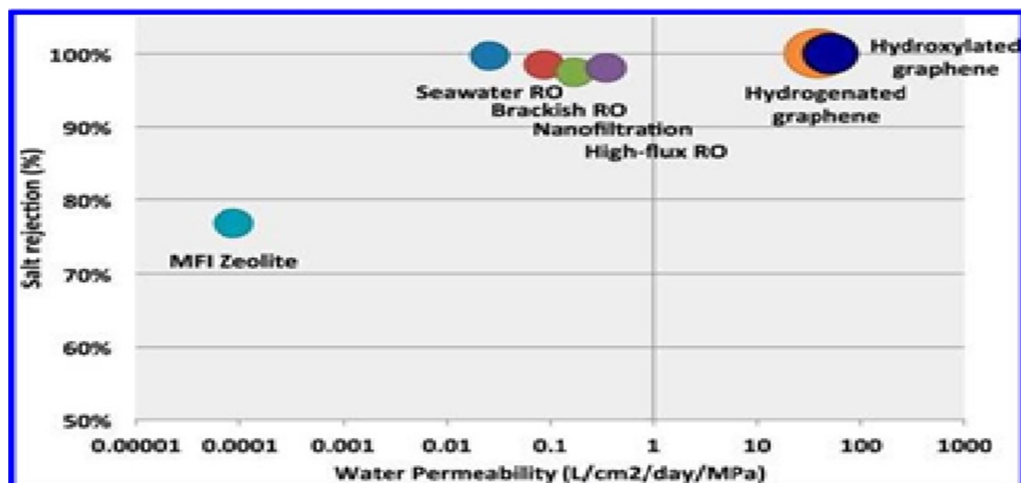


Fig.9. The two most important key performance parameters, salt rejection on y axis and water flux/permeability on x axis of graphene nanopores compared with the other common desalination technologies; reproduced with permission from Cohen-Tanugi and Grossman copyright (2012) ACS.

In another patent, Li and Ruhong [35] use mechanical strain control to open and close pores and tune a 2D MoS₂ desalination membrane. This invention offers more flexibility compared to graphene which has a fixed open/closed state that cannot be tuned externally. The sandwich-like structure of a ML of MoS₂ has a Young's modulus of ~270 GPa which is significantly smaller than the graphene sheet-like structure of a single layer of about 1 TPa. It is therefore more sensitive to mechanical strain and MoS₂ nanopores and can be made controllable with "open" and "closed" states; i.e., the pore opening size can be changed to allow or stop water flow by using strain. The steps involved in strain-controlled MoS₂ as desalination membrane are first to fix the MoS₂ nanoporous membrane on a frame, second install the frame-film device filter in seawater, third apply a pull force to the frame to increase the membrane frame surface area about 6-12% and fourth to pass pressurized seawater with a pressure range of 0-100 MPa through the MoS₂ membrane to allow water molecules to pass and block the salt ions and thus complete the desalination process. In some embodiments, the MoS₂ monolayer can have Mo or S or both Mo and S vacancy defects for selectivity and performance improvement.

Challenges and Outlook

Nanopores, with low energy requirements and high desalination efficiency are proving to be the new generation desalination devices. The theoretical studies of graphene and low-dimensional TMDs give insight to numerous

possibilities and predict the device characteristics for efficient desalination. The low-pressure operation of these nanoporous membranes and the self-cleaning, no fouling characteristics make them very attractive for use in desalination. Graphene, BN, MoS₂ and related nanopores offer a safe, reliable, sensitive, energy-saving and cost-effective water desalination technology that is ready to be put into action. But, in order to translate this technology to large-scale production, various aspects concerning process and fabrication need to be addressed. The main challenges are large-scale defect-free, well-defined membrane synthesis, uniform, precise and small-size pore generation, mechanical stability and functionalization of membranes. Liu et al. [37] successfully generated nanopores of 1-10 nm diameters in MoS₂ using a transmission electron microscope with a highly focused electron beam. Large-area, good-quality membrane with nanopores in the nm and sub-nm range can be fabricated, as shown by Waduge et al. [38] and Feng et al. [39]. Graphene is the ideal membrane with its only one-atom layer thickness and the simple techniques for introducing nanopores by ionic irradiation or chemical treatment and can be implemented with great success. The simulation study of Jun et al. [40] found that graphene mono-layers pinned every 40–160 Å can withstand pressures greater than 500 MPa without ripping. Experimental results for bulge tests, Bunch et al. [41] also confirmed the high strength of graphene. The rapid experimental progress suggests the practical feasibility of accurate and large-scale synthesis of highly

ordered nanoporous graphene and related 2D materials and the commercialization of this desalination technology is anticipated to be in the immediate future.

Acknowledgements

This work was not supported by any funding. The authors would like to take the opportunity to thank Eng. Wajeeh M. A. Aqra for his continuous encouragement and support.

References

- [1] Wali, F., "The future of desalination research in the Middle East", *Nature Middle East*, (2014); doi:10.1038/nmiddleeast.2014.273.
- [2] Elimelech, M. and Phillip, W.A., *Science*, 333 (2011) 712.
- [3] Pendergast, M.M. and Hoek, E.M.V., *Energy and Environmental Science*, 4 (6) (2011) 1946.
- [4] Zhu, C., Li, H., Zeng, X.C., Wang, E.G. and Meng, S., *Scientific Reports*, 3 (2013) 3163.
- [5] Yuan, H., Abu-Reesh, I.M. and He, Z., *Chemical Engineering Journal*, 270 (2016) 437.
- [6] Nguyen, B.H. and Nguyen, V.H., *Adv. Nat. Sci.: Nanosci. Nanotechnol.*, 7 (2016) 023002.
- [7] Thanh, T.D., Chuong, N.D., Hien, H.V., Kshetri, T., Tuan, L.H., Kim, N.H. and Lee, J.H., *Progress in Materials Science*, 96 (2018) 51.
- [8] Wasfi, A., Awwad, F. and Ayesh, A.I., *Biosensors & Bioelectronics*, 119 (2018) 191.
- [9] Moghadam, F. and Park, H.B., *Current Opinion in Chemical Engineering*, 20 (2018) 28.
- [10] Ramanathan, A.A., Aqra, M.W. and Al-Rawajfeh, A.E., *Environ. Chem. Lett.*, 16 (2018) 1217.
- [11] Suk, M.E., Raghunathan, A.V. and Aluru, N.R., *Appl. Phys. Lett.*, 92 (2008) 133120.
- [12] Tamsyn, A., Hilder, T.A., Gordan, D. and Chung, S-H., *Small*, 5 (19) (2009) 2183.
- [13] Suk, M.E. and Aluru, N.R., *J. Phys. Chem. Lett.*, 1 (2010) 1590.
- [14] Tanugi, D.C. and Grossman, J.C., *Nano Lett.*, 12 (2012) 3602.
- [15] Surwade, S.P., Smirnov, S.N., Vlassiuk, I.V., Unocic, R.R., Dai, S., Veith, G.M. and Mahurin, S.M., *Nature Nanotechnology*, 10 (2015) 459.
- [16] Heiranian, M., Farimani, A.B. and Aluru, N.R., *Nature Communications*, 6 (2015) 8616.
- [17] Wu, Y.B., Wagner, L.K. and Aluru, N. R., *J. Chem. Phys.*, 142 (2015) 234702.
- [18] Li, W., Yang, Y., Weber, J.K., Zhang, G. and Zhou, R., *ACS Nano*, 10 (2016) 1829.
- [19] Tanugi, D.C. and Grossman, J.C., *The Journal of Chemical Physics*, 141 (2014) 074704.
- [20] Tanugi, D.C., Lin, L. and Grossman, J.C., *Nano Lett.*, 16 (2) (2016) 1027.
- [21] Choi, J.Y. and Park, B.H., S.M.I.G. U.S. Patent, (2012) 0255899.
- [22] Sinsabaugh, S.L., Bedworth, P.V., Casey, Jr.D.F., Heise, S.E., Sinton, S.W. Stoltenberg, R.M. and Swett, J.L., United States Patent Application, (2015) 20150217219.
- [23] Stoltenburg, R.M., Bedworth, P.V., Heise, S.E. and Sinton, S.W., U.S. Patent, (2017) 20170043300.
- [24] Gilbert, S.M., Dunn, G., Pham, T., Shevitski, B., Dimitrov, E., Aloni, S. and Zettl, A., *Science Reports*, 7 (2017) 15096.
- [25] Khin, M.M., Nair, A.S., Babu, V.J., Murugan, R. and Ramakrishna, S., *Energy Environ. Sci.*, 5 (8) (2012) 8075.
- [26] Goh, P.S., Ismail, A.F. and Ng, B.C., *Desalination*, 308 (2013) 2.
- [27] International Desalination Association (IDA), "Desalination in 2008 global marker snapshot", 21st GWI/International Desalination Association Worldwide Desalting Plant Inventory (2008).

- [28] Fritzmann, C., Löwenberg, J., Wintgens, T. and Melin, T., *Desalination*, 216 (1) (2007) 1.
- [29] Semiat, R., *Environ. Sci. Technol.*, 42 (22) (2008) 8193.
- [30] Baldanov, M., Baldanova, D., Zhigzhitova, S. and Tanganov, B., *Reports of the Russian High School Academy of Science*, (2006) 32.
- [31] Tanganov, B.B., *European Journal of Natural History*, 1 (2013) 36.
- [32] Stetson, J.B., Mercurio, J., Alan Rosenwinkel, A. and Bedworth, P.V., *US Patent*, B2 (2013) 8361321.
- [33] Grossman, J., Ferralis, N., Tanugi, D.C. and Dave, S.H., *P.M.M.I.N.M.F.W.F. Google Patents*, WO (2014) 2014152407.
- [34] Mahurin, S.M., Vlassioux, I., Dai, S., Surwade, S.P., Unocic, R.R. and Smirnov, S., *N.G.M.f.D.o.S.W. US Patent*, (2016) 0207798.
- [35] Li, W. and Ruhong, W., *Google Patents*, CN (2015) 104925907A.
- [36] Sint, K., Wang, B. and Král, P., *J. Am. Chem. Soc.*, 130 (49) (2008) 16448.
- [37] Liu, K., Feng, J.D., Kis, A. and Radenovic, A., *A.T.M.D.N.W.H.S.D.T., ACS Nano*, 8 (2014) 2504.
- [38] Waduge, P., Bilgin, I., Larkin, J., Henley, R.Y., Goodfellow, K., Graham, A.C., Bell, D.C., Vamivakas, N., Kar, S. and Wanunu, M., *ACS Nano*, 9 (7) (2015) 7352.
- [39] Feng, J., Liu, K., Graf, M., Lihter, M., Bulushev, R.D., Dumcenco, D., Alexander, D.T.L., Krasnozhan, D., Vuletic, T., Kis, A. and Radenovic, A., *Nano Lett.*, 15(5) 2015 3431.
- [40] Jun, S., Tashi, T., Park, H., S., *Journal of Nanomaterials*, 2011(12) (2010) 380286. Doi: 10.1155/2011/380286
- [41] Bunch, J.S., Verbridge, S.S., Alden, J. S., Zande, A.M.V.D, Parpia, J.M., Craighead, H.G., McEuen, P.L., *Nano Letters* 8 (2008) 2458-2462 Doi: 10.1021/nl801457b

Probability Distribution of Magnetic Field Strengths through the Cyclotron Lines in High-Mass X-ray Binaries

A. Taani^a, A. Abushattal^b, A. Khasawneh^c, N. Almusleh^d and M. Al-Wardat^{d,e,g}

^aPhysics Department, Faculty of Science, Al Balqa Applied University, 19117 Salt, Jordan.

^bDepartment of Physics, Al-Hussein Bin Talal University, 71111, Ma'an, Jordan.

^cRegional Centre for Space Science and Technology Education for Western Asia-UN, Amman, Jordan.

^dDepartment of Physics, Al al-Bayt University, Al-Mafraq, 25113 Jordan.

^eDepartment of Applied Physics and Astronomy, University of Sharjah, P. O. Box 27272, Sharjah, UAE.

^gSharjah Academy for Astronomy, Space Science and Technology, Sharjah, UAE.

Doi : <https://doi.org/10.47011/13.3.8>

Received on: 08/08/2019;

Accepted on: 5/2/2020

Abstract: The study of variation of measured cyclotron lines is of fundamental importance to understand the physics of the accretion process in magnetized neutron star systems. We investigate the magnetic field formation, evolution and distribution for several High-Mass X-ray Binaries (HMXBs). We focus our attention on the cyclotron lines that have been detected in HMXB classes in their X-ray spectra. As has been correctly pointed out, several sources show variation in cyclotron lines, which can result due to the effect of accretion dynamics and hence that would reflect the magnetic field characteristics. Besides, the difference in time scales of variation of accretion rate and different types of companion can be used to distinguish between magnetized neutron stars.

Keywords: Stars: neutron stars, High-Mass X-ray binaries, Stars: magnetic field, Cyclotron lines.

Introduction

The cyclotron lines in accreting neutron stars (NSs) are detected as absorption features in their X-ray spectra. This detection is due to resonant scattering processes with electrons which are perpendicular to the B-field [1-5]. The significant detection of such behavior helps study the formation and evolution of X-ray binaries through the direct calculation of the magnetic field strength. However, most observed cyclotron lines have been detected above 10 keV and are interpreted as electron features, with inferred magnetic fields $B \sim 10^{12}$ G [6]. The amount of mass loss and the effect of the mass-loss *via* stellar winds may influence the stellar binary evolution. This will also allow

distinguishing the phenomenology of the X-ray sources and their optical counterparts in a natural way [4, 5, 7-13]. Despite its importance, many questions remain unanswered in terms of the accretion geometry and flow with significant uncertainties due to the small number of detected cyclotron lines in some sources [13-16]. In addition, a cutoff below 2-3 keV would remain undetected in the available spectra of some sources. Therefore, the physical properties of the accretion column, as well as the line profiles of cyclotron lines must be studied in detail [18]. Calculated cyclotron lines assume a strong variation in field strength with the distance from an emission region. However, no model

generating such high flux and high temperature at a layer deeper than absorbing heavy atoms has been proposed. According to recent studies, several pulsars show luminosity dependence changes on cyclotron resonance energy. The main aim of this paper is to investigate the probability distribution of magnetic field strengths among the HMXBs, using more robust values of the B-field obtained from cyclotron

lines in their X-ray spectra (see Table 1). One of the interesting properties of this class is the observed correlation between the orbital period and the spin period of the NS [19]. This would reveal the clues about the evolution of HMXBs, which can be understood in terms of the conservative evolution of normal massive binary systems.

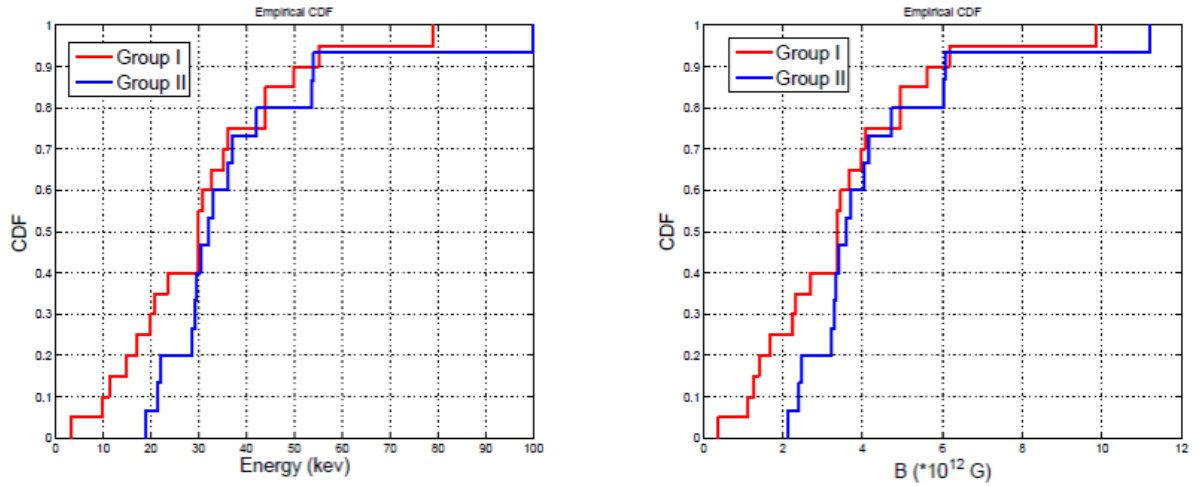


FIG. 1. The cumulative distribution function of cyclotron energy and magnetic field strength of the observed sample HMXBs, dividing them into two groups; transient sources (Group I) and persistent sources (Group II).

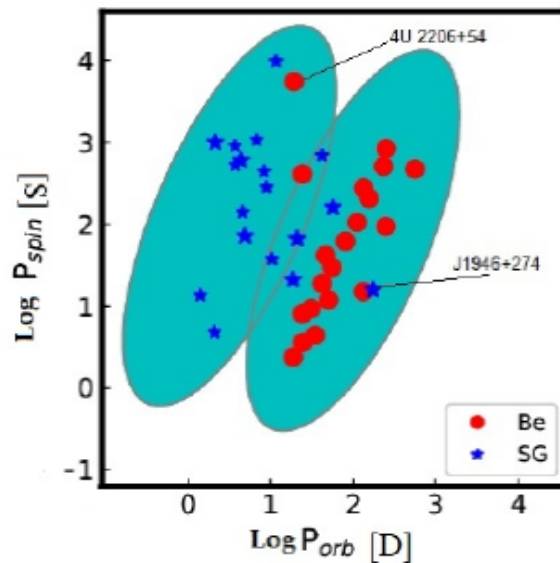


FIG. 2. Corbet diagram for all the HMXBs that have presented a cyclotron line. A group of SG and Be clusters act together and occupy the same regions of the parameter space, akin to the separated regions in this figure. Note that the peculiar properties of J1946+274 and 4U 2206+54 let them be observed in Be and SG regions, respectively. Future observation and modeling including disk/wind fed with orbital motion would figure out the true nature and any further evolution of such binaries. The shaded regions represent the potential observations of the orbital parameters of those groups.

Statistical Tests

We make use of two statistical tests to try to quantitatively evaluate our sample of magnetic field strength (see Table 1): the Kolmogorov-Smirnov (KS) test and the Anderson-Darling (AD) test (e.g. [20-21]). Because the AD test uses the cumulative distribution, we use it as our primary comparison and use the KS test results as a consistency check. The first test that we perform is for normality, checking whether the distribution is consistent with a single Gaussian which has the mean and standard deviation of the observed populations. Neither the mean nor the variance is known beforehand for the distributions and we perform testing at the 5% level of significance. Furthermore, we use Monte Carlo (MC) test to examine the confidence that the given distribution is either normally or log-normally distributed. Our results are tabulated in Table 2. The results of the KS test agree in every case with those of the AD test and have therefore been omitted from the table. From the table, it is clear that every distribution, with the exception of the magnetic field for the transient sources, fails the AD test for normality. However, every distribution passes the test for log-normality. The confidence levels from the MC test are all below 50% for the persistent sources and slightly above 50% for the spin and orbit distributions of the transient sources. While these statistical tests and fits do not, by themselves, constitute a proof of two populations, coupled with the other pieces of evidence (i.e., such as mass transfer due to Roche lobe overflow or stellar wind that can also be a supplement to the mass transfer rate in HMXB systems, tidal interaction, gravitational wave radiation, magnetic braking or X-ray irradiated wind outflow), they do lend support to the hypothesis of two populations. We show in Fig. 1 the cumulative distribution function of the energy of cyclotron absorption lines (left) and magnetic field strength (right) of the observed sample of HMXBs. We note that this function is not smooth, implying that the energy of the lines is not constant, but changes linearly with the luminosity of the sources [22]. We excluded the data after 65 KeV, because the high field cut-off appears to be real. On the observational level, this variability in transient sources, for example, is most likely due to the irregular optical and IR outbursts generally observed in Be stars and it is attributed to changes in the presence structure of

the circumstellar disk. These effects were investigated by [23].

P_{SPIN} VS. P_{ORB}

The P_{Spin} versus P_{orb} diagram [19] (also known as the Corbet diagram, see Fig. 2) is a valuable tool to study the interaction and feedback between the NS and accreted matter and the influence of the local absorbing matter, the location of the different systems being determined by the equilibrium period reached by the rotation of the NS accreting matter on its surface. The main parameters of the HMXB sample are summarized in Table 1. However, the orbital period of X-ray binaries is expected to change due to redistribution of the angular momentum due to the interaction between the components of the binary system. As such, measurement of the rate of change of the orbital period (i.e., orbital period derivative) of the binary system is, therefore, necessary in order to understand the evolution of compact binary systems [24-25]. The spin and orbital periods of all HMXBs for which values are known are plotted in Fig. 2, which represents a panoramic perspective for binaries occupying separate parts of the plot. This is not only because the NSs in HMXBs have a different type of companion, but also because the accretion process itself seems to be universal [4-5], with the NS spin in or near an equilibrium state in which the magnetospheric radius of the NS equals the Keplerian co-rotation radius. They are a group of supergiant (SG) sources having peculiar properties of orbital parameters and could be a good test-candidate for those in Be sources. Future observations can identify these candidates. This group is categorized according to their observed spin period as in Table 1. It is noteworthy to mention here that the effect of mass exchange process on the orbital evolution has two scenarios 1) conservative case: where the total mass and the total angular momentum of the system do not change (see i.e., [26-27]). Hence, the size and the orbital period of the system must be decreased if the mass is transferred to the less massive component (NS) and *vice versa*. 2) non-conservative case (more complex): this will depend on how and how much angular momentum is lost from the system (see i.e., [28-29] for full details and references).

TABLE 1. List of observational parameters of all known HMXBs with cyclotron resonant scattering features.

Object	P_{spin} (s)	P_{orbit} (d)	E_{cyc} (keV)	B (10^{12}G)	Type	Ref.
4U 0115+63	3.6	24.3	15 ± 0.15	1.7	Transient/ Be	^{3,30}
4U 1907+09	439	8.37	18.8 ± 0.4	2.1	Persistent/SG	^{31,14}
4U 1538-52	529	3.73	$21.4^{+0.9}_{-2.4}$	2.4	Persistent/SG	^{24,32}
Vela X-1	283	8.96	$54^{+0.5}_{-1.1}$	6	Persistent/ SG	^{33,34}
Cen X-3	4.8	2.09	$30.4^{+0.3}_{-0.4}$	3.4	Persistent/ SG	^{14,35}
V0332+53	4.37	34.25	$30^{+0.2}_{-0.2}$	3.4	Transient/ Be	^{36,37}
Cep X-4	66.3	20.85	$30.7^{+1.8}_{-1.9}$	3.4	Transient/ SG	^{1,38}
A 0535+26	105	111	50 ± 0.7	5.6	Transient/ Be	^{3,39}
GX 301-2	690	41.5	$42.4^{+3.8}_{-2.5}$	4.7	Persistent/ Be	^{14,38}
LMC X-4	13.5	1.4	100 ± 2.1	11.2	Persistent/ SG	^{14,40}
4U 0352+309	837	250	$28.6^{+1.5}_{-1.7}$	3.2	Persistent/ Be	¹⁴
OAO1657-415	37.7	10.4	36	4	Persistent/ SG	^{41,42}
J1946+274	15.83	169.2	$36.2^{+0.5}_{-0.7}$	4	Transient/SG	^{6,43}
MXB 0656-072	160.4	56.2	$32.8^{+0.5}_{-0.4}$	3.7	Transient/SG	^{6,44}
GX 304-1	275.46	132.5	$53.7^{+0.7}_{-0.6}$	6	Transient/Be	^{45,46}
J16493-4348 [†]	1069	6.78	33 ± 4	3.7	Persistent/SG	^{47,48}
GS 1843+00	29.5	55	20 ± 0.45	2.2	Transient/Be	^{41,49}
1A1118-61	408	580	$55.1^{+1.6}_{-1.5}$	6	Transient/Be	^{50,51}
J1008-57	93.5	247.8	79	10	Transient/Be	^{52,53}
EXO 2030+375	41.7	46	11.44 ± 0.02	1.3	Transient/Be	^{3,52}
J1626.6-5156	15	132	10	1.1	Transient/Be	^{53,54}
4U 1700-377	–	3.4	37	4.1	Persistent/SG	^{41,55}
J01583+6713	469	561	35.3 ± 1.6	4	Transient/Be	⁵⁶
4U 2206+54	5500	19.11	29.6 ± 2.8	3.3	Persistent/Be	^{57,58}
2S 0114+65	9700	11.6	22	2.5	Persistent/SG	^{59,60}
J1739-302 [†]	–	51.5	30	3.4	Transient/SG	^{61,62}
J18483-0311 [†]	21	18.6	3.3	0.4	Transient/SG	^{63,64}
J0440.9+4431	205	155	32	3.6	Persistent/Be	⁶⁵
J1409 - 619	506	233	44 ± 3	4.9	Transient/Be	⁶⁶
J18462-0223	997	–	30 ± 7	3.4	Transient/SG	⁶⁷
J18179-1621	11.82	20-50	$20.8^{+1.4}_{-1.8}$	2.3	Transient/Be	⁶⁸
J17544-261	71.5	4.9	17	1.45	Transient/SG	⁶⁹
2S 1553-542	9.27	30.6	23.5 ± 0.4	2.7	Transient/Be	⁷⁰
4U 1909+07	604	4.4	44	4.9	Transient/SG	⁷¹
J16393-4643	904	4.2	$29.3^{+1.1}_{-1.3}$	3.3	Persistent/SG	⁷²
J054134.7-68	61.6	80	10	1.2	Persistent/Be	⁷³
KS 1947+300	1808	41.5	12.5	1.4	Transient/Be	⁷⁴
IGR J18027-201	140	4.6	23	2.6	Persistent/SG	⁷⁵
SMC X-2	2.4	18.6	27	3.1	Transient/Be	⁷⁶
J0520.5-69	8	24	31.5	3.6	Transient/Be	⁷⁷

TABLE 2. Anderson-Darling and Monte Carlo statistical tests of the distributions of the spin period, orbital period and magnetic field for the persistent and transient sources.

		Anderson-Darling (5%)		MC confidence	
		Normal	Log-Normal	Normal	Log-Normal
Persistent	Spin	3.264	0.502	0.001%	26.7%
	Orbit	2.454	0.548	0.002%	21.2%
	Bfield	1.307	0.389	0.4%	46.6%
Transient	Spin	1.974	0.355	0.001%	54.6%
	Orbit	1.861	0.367	0.004%	51.7%
	Bfield	0.4963	0.5442	27.5%	21.7%

Candidate sources for cyclotron features are references related to period measurements in the literature. Some have errors originating from the applied analysis, designated with a dagger or from the supplied data, designated with an asterisk.

B_{FIELD} VS. P_{SPIN}

It may be interesting to investigate the relation between the magnetic field strength and spin period, also known as the spin-up line [88, 95, 110] to discuss the formation and evolution of these systems through various evolutionary stages. Fig. 3 represents a plot of the magnetic field strength as a function of the spin period in logarithmic scale with cyclotron energy colored. It can be seen clearly that there is a possible correlation between the magnetic field strength and the spin period. Moreover, the cyclotron energy independence of the spin period is very clear. This implies that the NSs in these systems generally have ages $\sim 10^6$ years. However, there are strong magnetic fields ($B > 10^{12}$ G) in the HMXBs as evidenced by their regular x-ray pulsations, while the absence of such regular pulsations and thus strong magnetic fields can be noticed in the Low Mass X-ray Binaries (LMXBs) [69]. However, the known magnetic field strengths of the X-ray pulsars are all lying in a very narrow band (due to the observational selection effect) and can be used by the equation:

$$E_{cyc} = 11.6 B_{12}(1+z) \quad (1)$$

where z is the gravitational redshift at the NS surface, which is approximately ($z = 0.3$) in the

line-forming region. Here, B_{12} is the magnetic field strength in units of 10^{12} G and the higher harmonics have a cyclotron energy n times the fundamental energy E_{cyc} . Using Eq. (1), the surface magnetic field strengths of HMXB sample have been calculated and presented in Table 1. We found that these values are clustered in a relatively narrow range of $(1-13.3) \times 10^{12}$ G.

To illustrate all HMXB magnetic field strength distributions, a histogram of HMXB magnetic field strengths is plotted in Fig. 4 and the smooth curve represents the normal fit to the observed data. We assume that the distribution follows a Gaussian distribution, centered at 12.5×10^{12} G. In these systems, the data suffers from the selection effect, which may be due to the sensitivity of the current X-ray observatories. About 89% of all HMXBs considered in this study have high magnetic fields of the order of $B = 12.5 \times 10^{12}$ G. The maximum and minimum values of HMXB magnetic fields are, respectively, 11.2×10^{12} G (J0520.5-69) and 1.1×10^{12} G (J1626.6-5156). We fit the Gauss function to the magnetic distributions. The Gauss function we choose reads:

$$y = y_0 + \frac{A}{\omega \sqrt{\frac{\pi}{2}}} \exp\left(-2\left(\frac{x-x_c}{\omega}\right)^2\right). \quad (2)$$

Here, the parameters y_0 , x_c , ω and A are: offset of vertical axis, center of horizontal axis, width and area of the curve describing the magnetic distribution, respectively. The fitting results are listed in Table 3.

TABLE 3. Fit parameters of the distribution of magnetic field strengths.

quantity	y0	xc	w	A	σ	χ^2/Dof	R^2
Magnetic field	12.6 ± 0.43	15.03 ± 0.02	2.38 ± 0.02	12.76 ± 0.016	0.22	0.05	0.26

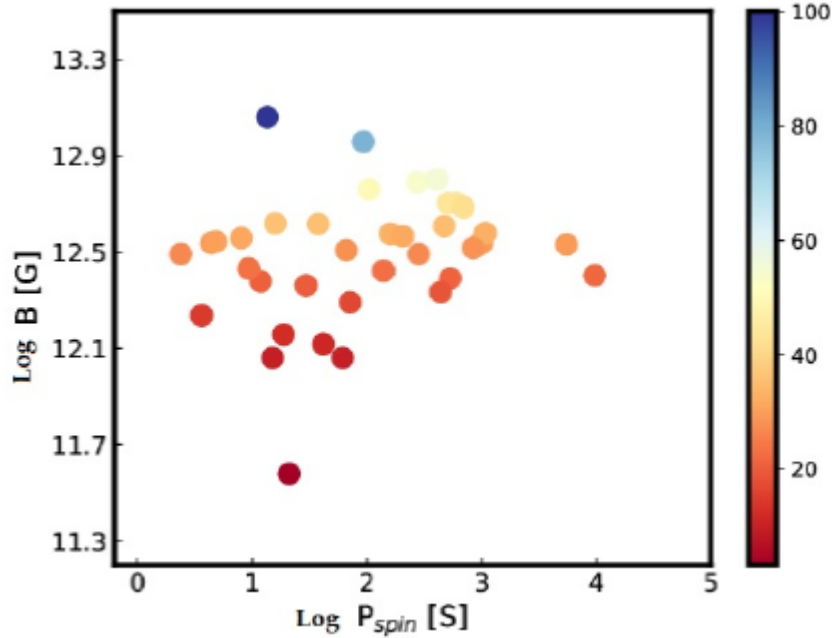


FIG. 3. The diagram of magnetic field strengths *versus* spin periods for our data sample of HMXBs (SG and Be sources) in Table 1. Color coding is based on the associated cyclotron energy. Sources with the same energy (same color) show zero slope against the spin period.

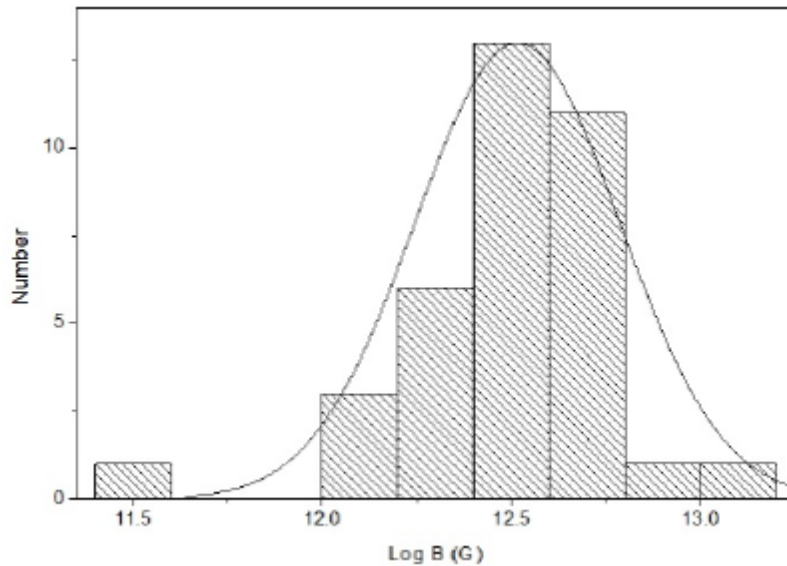


FIG. 4. Magnetic field strength distribution of the observed sample. The solid line is the curve fitted using a Gaussian function.

Summary and Conclusions

The magnetic field strength of several HMXB systems has been investigated. As such, the magnetic field is responsible for the formation of an accretion column, since it forces the particles to hit the NS surface at its magnetic poles.

Therefore, the cyclotron lines are of fundamental importance to understand the properties of other physical parameters of the magnetized X-ray system. Here, we find that most NSs in the HMXBs show an intermediate level of field strength, $\sim 10^{12}$ G. However, the characteristics of their X-ray behaviors and properties are

different. We analyze and discuss the distribution of the characteristics of the HMXB sample, through benefiting from the Corbet diagram. In particular, one can see that all transient sources have an orbital period more extended than 11 d, thus newly detected sources for which $P > P_{11d}$ have a high probability of being transients. An attempt is made to quantify the possible distribution of the magnetic field strength through the cumulative probability distribution. The extent to which the sample is complete is well demonstrated by a log-normal law and shows somewhat similar behavior for both groups. Such parameters greatly affect the model of wind-fed binary systems and can be constrained by stellar properties during the binary evolution. However, the quantity of these exciting objects has greatly increased in recent years, mainly due to successful surveys. More details and results on the multiplicity of the cyclotron line features from some sources are

required to explain the behavior of shape variation during the rotation phase as well as the change in accretion rate and characteristics.

Acknowledgements

Ali Taani gratefully acknowledges the Institute of High Energy Physics, Chinese Academy of Sciences through the CAS-PIFI Fellowship 2018, where this work started. M. Mardini thanks the National Natural Science Foundation of China for the support under the grant numbers 11988101 and 11890694 and also the National Key RandD Program of China No. 2019YFA0405500. A. Abushattal acknowledges the support from Al-Hussein Bin Talal University, Deanship of Scientific Research and Graduate Studies under grant No. (17/2018). The authors would like to thank the anonymous referees for helpful suggestions and comments on the manuscript.

References

- [1] Truemper, J., Pietsch, W., Reppin, C. et al., *ApJ*, 219 (1978) 105.
- [2] Voges, W., Pietsch, W., Reppin, C. et al., *ApJ*, 263 (1982) 803.
- [3] Wilson, C., Finger, M. and Camero-Arranz, A., *ApJ*, 678 (2008) 1263.
- [4] Taani, A., Karino, S., Song, L. et al., *Research in Astronomy and Astrophysics*, 19 (2019a) 12.
- [5] Taani, A., Karino, S., Song, L. et al., *Journal of Physics: Conference Series*, 1258 (2019b) 012029.
- [6] Heindl, W., Coburn, W., Gruber, D. et al., *ApJ*, 563 (2001) L35.
- [7] Taani, A., Zhang, C.M., Al-Wardat, M. et al., *Astronomische Nachrichten*, 333 (2012) 53.
- [8] Shakura, N., Postnov, K., Kochetkova, A. and Hjalmarsdotter, L., *MNRAS*, 420 (2012) 216.
- [9] Taani, A., *Research in Astronomy and Astrophysics*, 16 (2016) 101.
- [10] Mardini, M., Li H., Placco, V. et al., *ApJ*, 875 (2019a) 89.
- [11] Mardini, M., Placco, V., Taani, A. et al., *ApJ*, 882 (2019a) 27.
- [12] Mardini, M., Ershiadat, N. and Al-Wardat, M., *Journal of Physics: Conference Series*, 1258, (2019a) 12024.
- [13] Karino, S., Nakamura, K. and Taani, A., *Publications of the Astronomical Society of Japan*, 71 (2019) 58.
- [14] Coburn, W., Heind, W., Rothschild, R. et al., *ApJ*, 580 (2002) 394.
- [15] Kreykenbohm, I., Mowlavi, N., Produit, N. et al., *A&A*, 433 (2019) 45.
- [16] Taani, A., Al-Wardat, M. and Zhao, Y. H., *International Journal of Modern Physics: Conference Series*, 23 (2013) 284.
- [17] Taani, A. and Khasawneh, A., *Journal of Physics: Conference Series*, 869 (2017) 012090.
- [18] Nishimura, O., *PASJ*, 57 (2005) 769.
- [19] Corbet, R.H.D., 1986, *MNRAS*, 220, 1047.
- [20] Press, W. H., Teukolsky, S. A., Vetterling, W. T. et al., *Numerical Recipes: "The Art of Scientific Computing"*, (Cambridge University Press, 2007).
- [21] Cai, Y., Taani, A., Zhao, Y. and Zhang, C., *Chinese Astronomy and Astrophysics*, 36 (2012) 137.

- [22] Tsygankov, S., Krivonos, R. and Lutovinov, A., *MNRAS*, 421 (2012) 2407T.
- [23] Reig, P., Negueruela, I., Buckley, D. A. et al., *A&A*, 367 (2001) 266.
- [24] Rivers, E., Markowitz, A., Pottschmidt, K. et al., *ApJ*, 709 (2010) 179.
- [25] Wei, Y. C., Taani, A., Pan, Y. Y. et al., *Chin. Phys. Lett.*, 27 (2010) 9801.
- [26] Dosopoulou, F. and Kalogera, V., *ApJ*, 825 (2016) 70.
- [27] Bobrick, A., Davies M.B. and Church, R.P., *MNRAS*, 467 (2017) 3556.
- [28] Demircan, O., Eker, Z., Karata, Y. et al., *MNRAS*, 366 (2006) 1511.
- [29] Eker, Z., Demircan, O., Billir, S. et al., *MNRAS*, 373 (2006) 1483.
- [30] Wheaton, W., Doty, J., Primini, F. et al., *Nature*, 282 (1979) 240.
- [31] Nagase F., Dotani, T., Tanaka, Y. et al., *ApJ*, 375 (1991) 49.
- [32] Rodes-Roca, J., Torrejon, J., Kreykenbohm, I. et al., *A&A*, 508 (2009) 395.
- [33] Kretschmar, P., Kreykenbohm, I., Pottschmidt K. et al., *ATel*, (2005) 601.
- [34] Makishima, K., Mihara, T. and Ishida, M., *ApJ*, 365 (1990), 59.
- [35] Kreykenbohm, I., Coburn, W., Wilms, J. et al., *A&A*, 395 (2002) 129 .
- [36] Santangelo, A., del Sordo, S., Segreto, A. et al., *ApJ*, 340 (1998) 55.
- [37] Makishima, K., Mihara, T. and Ishida, M., *ApJ*, 365 (1990) 59.
- [38] Pottschmidt, K., Kreykenbohm, I., Wilms, J. et al., *ApJ*, 634 (2005) 97.
- [39] Nakajima, M., Mihara, T. and Makishima, K., *ApJ*, 710 (2010) 1755.
- [40] McBride, V., Wilms, J., Kreykenbohm, I. et al., *A&A*, 4470 (2007) 1065M.
- [41] Wilson, C. A. and Finger, M. H., *ATel*, (2005) 605.
- [42] Terada, Y., Mihara, T., Nakajima, M. et al., *ApJ*, 648 (2006) 139.
- [43] Barbera, A., Burderi, L., Di Salvo, T. et al., *ApJ*, 553 (2001) 375.
- [44] Coburn, W., Heind, W., Gruber D. et al., *ApJ*, 552 (2001) 738.
- [45] Orlandini, M., Frontera, F., Masetti, N. et al., *ApJ*, 748 (2012) 86.
- [46] Denis, M., Bulik T. and Marcinkowski R., *AcA*, 60 (2010) 75D .
- [47] Pottschmidt, K., Suchy, S., Rivers E. et al., *AIP Conf. Ser.* 1427 (2011) 60.
- [48] Heindl, W., Coburn, W., Kreykenbohm, I. et al., *ATel*, 200 (2003) 1.
- [49] Sakamoto, T., Barthelmy, D., Baumgartner W. et al., *ATel*, (2010) 2815.
- [50] Yamamoto, T., Sugizaki, M., Mihara T. et al., *Astron. Soc. Jpn.* 63 (2011) 751.
- [51] Nespoli, E., Fabregat, J. and Mennickent, R. E., *A&A*, 516 (2010) A106.
- [52] D’Ai, A., Cusumano, G., La Parola, V. et al., *A&A*, 532 (2011) A73.
- [53] Piraino, S., Santangelo, A., Segreto S. et al., *A&A*, 357 (2000) 501.
- [54] Doroshenko, V., Suchy, S., Santangelo A. et al., *A&A*, 515 92010) L1.
- [55] Devasia, J., James, M., Paul, B. et al., *MNRAS*, 414 (2011) 1023.
- [56] Naik, S., Paul B., Kachhara, C. et al., *MNRAS*, 413 (2011) 241.
- [57] Sguera, V., Bazzano, A., Ubertini, P. et al., *ATel*, 6664 (2014) 1S.
- [58] Sasaki, M., Klochkov, D., Kraus, U. et al., *A&A*, 517 (2010) A8.
- [59] Wang, W., *A&A*, 516 (2010) A15.
- [60] Wang, W., *MNRAS*, 398 (2009) 1428.
- [61] Rodriguez, J., Tomsick, J. A., Bodaghee, A. et al., *A&A*, 508 (2009) 889.
- [62] Blay, P., Martnez-Nunez, S., Negueruela, I. et al., *A&A*, 489 (2008) 669.
- [63] Drave, S. P., Clark, D. J., Bird, A. J. et al., *MNRAS*, 409 (2010) 1220.
- [64] Chernyakova, M. et al., *Astron. Telegram*, (2003) 157.
- [65] Sguera, V. Ducci, L., Sidoliet, L. et al., *MNRAS*, 402 (2010) L49.
- [66] Orlandini, M., Frontera, F., Masetti, N. et al., *ApJ*, 748 (2012) 86.

- [67] Grebenev, S.A. and Sunayev, R.A., *Astr. Lett.*, 36 (2010) 53.
- [68] Tuerler, M., Chenevez, J., Bozzo, E. et al., *ATel*, (2012) 3947.
- [69] Bhalerao, V., Romano, P., Tomsick, T. et al., *MNRAS*, 447 (2015) 2274.
- [70] Tsygankov, S., Lutovinov, A., Krivonos, R. et al., *MNRAS*, 457 (2015) 258T.
- [71] Jaisawal, G.K., Naik, S., Paul, B. et al., *ApJ*, 779 (2013) 54.
- [72] Bodaghee, A, Tomsick, J. A., Fornasini, F. A. et al., *ApJ*, 823 (2016) 146.
- [73] Manousaki, S.A., Walter, R., Audard, M. et al., *A&A*, 498 (2009) 217.
- [74] Lutovinov, A. and Tsygankov, S., *MNRAS*, (2017) 466.
- [75] Jaisawal, G. and Naik, S., *MNRAS*, 461 (2016) L97.
- [76] Tendulkar, S. P., Furst, F., Pottschmidt, K. et al., *ApJ*, 795 (2014) 154.
- [77] Enoto, T., Makishima, K., Terada, Y. et al., *PASJ*, 60 (2008), 57.

Composite Metallic Nano Emitters Coated with a Layer of Insulator Covered by Au Layer

A. Al Soud^a, R. N. Al Buqain^b and M. S. Mousa^a

^a *Surface Physics and Materials Technology Lab, Department of Physics, Mutah University, Al-Karak 61710, Jordan.*

^b *Cell Therapy Center, University of Jordan.*

Doi : <https://doi.org/10.47011/13.3.9>

Received on: 28/11/2019;

Accepted on: 22/4/2020

Abstract: In this work, the differences in the behavior and properties of the emitted electron beam from tungsten (W) tips were studied before and after coating these tips with a thin layer of dielectric material followed by a thin layer of gold, to improve the emission current density, stability and emission current pattern concentration. The core of the composite cathode is made of high-purity tungsten (W). Measurements have been made with clean W emitters before and after coating these tips with two types of epoxy resins (epoxy 478 resins or epoxy UPR- 4 resins) followed by a thin layer of gold. For critical comparison, several tungsten tips with various apex-radii have been prepared using electrochemical etching techniques. The emitters have been coated by dielectric thin films of various thicknesses and the layer of Au used for coating the Epoxy layer has the same thicknesses. Their behavior has been recorded before and after the process of coating. These measurements include the current-voltage (I-V) characteristics and Fowler-Nordheim (F-N) plots. Imaging has also been done using a visible light microscope (VLM), along with a scanning electron microscope (SEM) to help in characterizing the epoxy layer thickness on the tip surface after coating. Besides, the emission patterns have been recorded from the phosphorescent screen of a field electron emission microscope (FEM). Having two types of composite systems tested under similar conditions provided several advantages. These measurements helped in producing a new type of emitters that have more suitable features with each of the two resins.

Keywords: Cold field emission, Nano emitter, Dielectric coating, Au layer.

Introduction

The improved electron emission from metal through dielectric and metallic coatings has been a subject of considerable interest at present. Within the search for stable and bright electron sources, a deeper understanding of high voltage breakdown phenomena has been greatly required by developing theories of induced electron emission in the metal-insulator-metal-vacuum interface. The emitter is usually formed into a tip, which has an apex radius ranging from several nanometers to a hundred nanometers [1-

4]. When preparing very sharp emitters, it is necessary to use a metal of the highest possible quality. Within this work, all experiments have been carried out using high-purity polycrystalline tungsten wire. Tungsten is used due to its favorable properties, such as the highest melting point, high strength, high work function and heat resistance at high temperatures [1, 3- 7]. Moreover, tungsten emitters with different apex radii ranging from 100 -150 nm have been prepared and coated with a thin layer

of various epoxy resin types (478 and UPR-4 resins) [1, 4- 7]. Additionally, the Epoxy layer has been covered by a thin layer of gold. The thickness of the epoxy layer was approx. 150 nm. The scanning electron microscope was used to extract the thickness of the epoxy layer. The thickness of the Au layer was 4 nm determined by the sputter coater. The emission patterns have been directly recorded from the phosphor screen of the field electron microscope (FEM) using a digital camera. The current-voltage (I-V) measurements and Fowler–Nordheim (F-N) plots have been obtained under ultra-high vacuum (UHV) conditions with a basic pressure of about 10^{-7} Pa.

Experimental Techniques

The tungsten emitters (tips) were prepared by electrolytic etching. A 0.1 mm diameter tungsten wire was immersed into a 2 molar sodium hydroxide solution with the emitter held by a conductive cylinder usually made of corrosion-proof material. Both the anode (tungsten wire) and the cathode (steel cylinder) were immersed in the sodium hydroxide solution and connected to a DC power source (12 V). When immersing approximately 0.8 cm of tungsten wire in NaOH solution, the etching current starts with a value of around (5 μ A). Then, the tip is placed in an ultrasonic bath for 15 minutes to clean it from the oxide layers formed on the tip surface [1, 6-10].

We have discovered that to obtain a layer of 150 nm thick epoxy layer (EpoxyLite 478 resin or EpoxyLite UPR-4 resin) on the emitter surface, the tip has to be dipped into the epoxy 12 times very slowly and vertically, which yields a 15 nm layer [1, 8, 11]. In the following way, the sample holder that keeps the sample in a vertical position is mounted on a trolley that moves vertically and lowers to a flask of EpoxyLite resin and the tip [7, 10]. To ensure an even distribution of resin on the surface of the tip and stabilize the EpoxyLite resin on the tip surface, the coated tip is transferred into a furnace and subjected to 30-minute curing at 373 K to drive off the solvent, followed by 30-minute curing at 453 K to complete the curing of the resin [4, 7-10]. Then, we used the sputter coater to cover the tips by 4nm of Au, where a desired operating pressure has been obtained by a rotary pump

with an inert gas, such as argon, admitted to the chamber by a fine control valve to ionize the argon gas. It also applies an electric field which accelerates the ions to the tip, as shown in Fig. 1 [9-14].

Next, the composite emitter is mounted in a standard FEM with an emitter screen distance of 10 mm [1, 4, 10- 13]. The emission patterns are recorded from a phosphor screen coated by tin oxide layers. All the experiment was performed under ultra-high vacuum (UHV) system pressures of approx. 10^{-7} Pa. The UHV system has been baked at a temperature of about 453 K for 12 hours [1, 13- 18]. Before adding the liquid nitrogen to the trap, the radius of each emitter apex has been measured from an image taken in a 30 kV SEM at magnifications up to 1000 X.

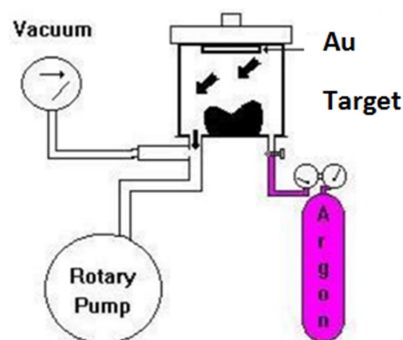


FIG.1. A schematic diagram showing the sputter coater.

Results and Discussion

The tungsten micro emitters have been prepared to have an apex radius of approximately 100 to 150 nm. Presented results include SEM images [14, 15] of emitter's apex, as well as I-V characteristics and F-N type plots of the field emission characteristics.

Fig. 2A, B shows the visible light microscope (VLM) images for uncoated type 1 and type 2 emitters. The measurement radii for emitter types 1 and 2 were 125 nm and 120 nm, respectively. Fig. 3A shows SEM images for emitter type 1 which had an approximately hemispherical apex being coated with a 150 nm thick layer of the EpoxyLite UPR- 4 resin followed by 4 nm of gold. Fig. 3B shows a SEM image for emitter type 2 which had an approximately hemispherical apex being coated with a 150 nm thick layer of EpoxyLite 478 resin followed by 4 nm of gold.

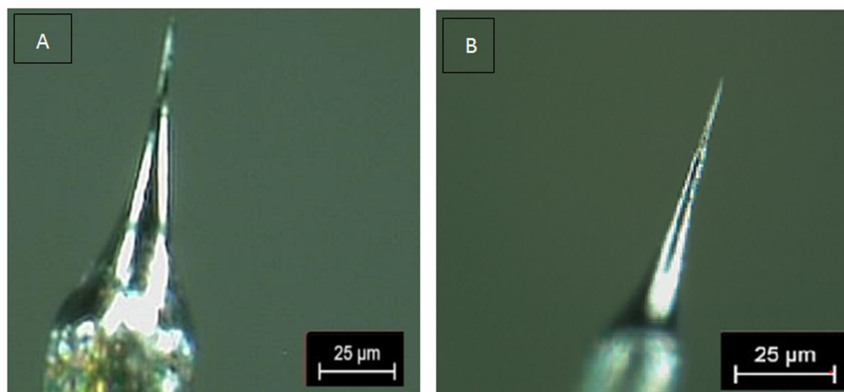


FIG. 2. A) Visible light microscope image (X 1500) for uncoated emitter type 1, with an apex radius of 125 nm. B) Visible light microscope image (X 1500) for uncoated emitter type 2, with an apex radius of 120 nm.

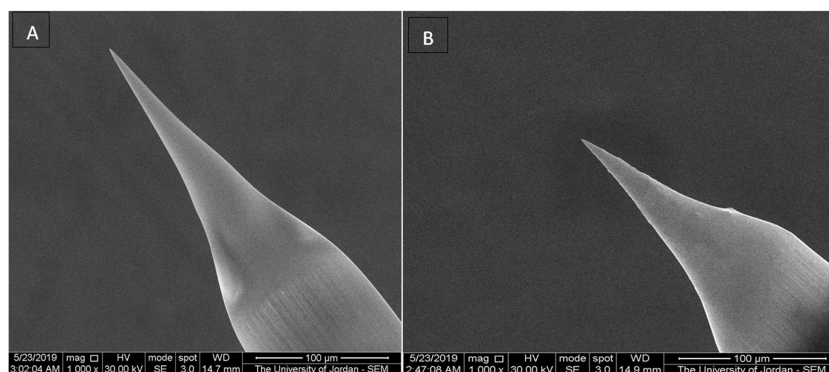


FIG. 3. A) SEM image at magnification (X 1000) for emitter type 1 (tungsten/ 150 nm UPR- 4 resin/ 4 nm Au). B) SEM image at magnification (X 1000) for emitter type 2 ((tungsten/ 150 nm 478 resin/ 4 nm Au).

The most important factors to be considered are the structure and stability of the emission pattern, as these effects are a reflection of the influence of the intermediate coating on the emission properties. The emission of two types of newly synthesized emitters was tested and photographed on the phosphorus emission screen. The emission current patterns for the uncoated emitters have been taken at the same voltage values when the voltage was decreased slowly. In detail, the FEM emission current

pattern primarily consists of multi bright spots. Fig. 4 shows the emission current pattern for uncoated emitter type 1. Fig. 5 shows the emission current pattern for uncoated emitter type 2. Fig. 6 shows the stability structure pattern for uncoated emitter type 1. Fig. 7 shows the stability structure pattern for uncoated emitter type 2. However, the stability structure images for the two types of emitter were taken at the same voltage and the duration time between obtaining the next images is 15 minutes.

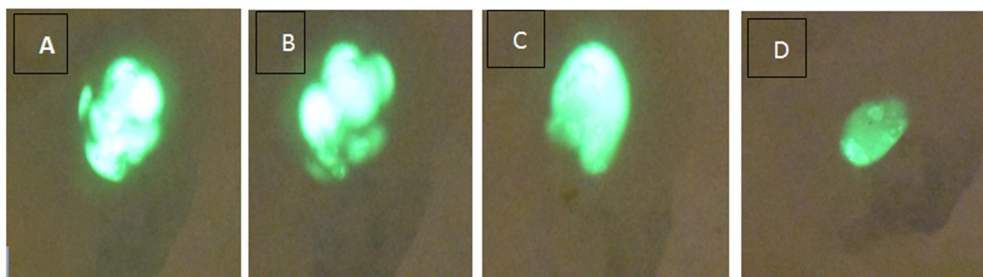


FIG. 4. Emission current pattern for uncoated emitter type 1. A) Emission current 1.5 μA , applied voltage 1600 V. B) Emission current 1.2 μA , applied voltage 1400 V. C) Emission current 1 μA , applied voltage 1200 V. D) Emission current 0.4 μA , applied voltage 1000 V.

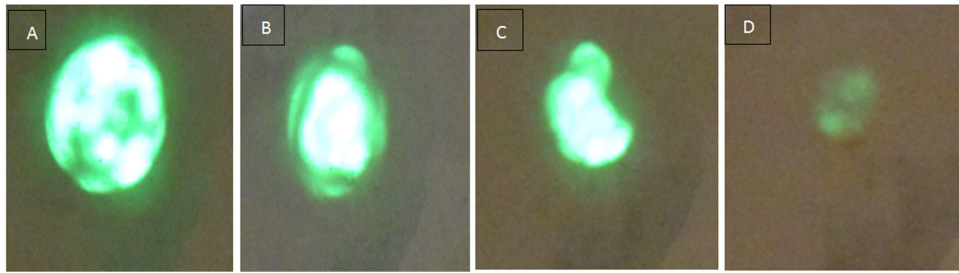


FIG. 5. Emission current pattern for uncoated emitter type 2. A) Emission current $1.8 \mu\text{A}$, applied voltage 1600 V. B) Emission current $1.6 \mu\text{A}$, applied voltage 1400 V. C) Emission current $1.3 \mu\text{A}$, applied voltage 1200 V. D) Emission current $0.8 \mu\text{A}$, applied voltage 1200 V.

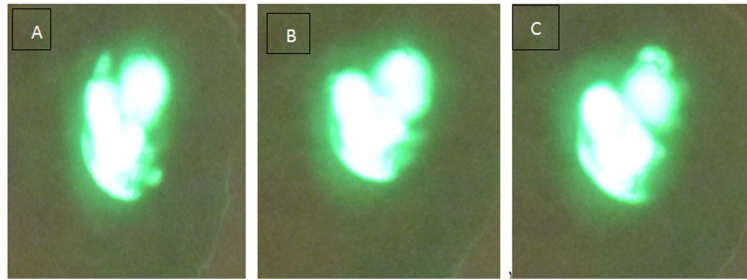


FIG. 6. The stability structure pattern for uncoated emitter type 1, at emission current $2.1 \mu\text{A}$ and applied voltage 1800 V; the duration time between obtaining the next images is 15 minutes.

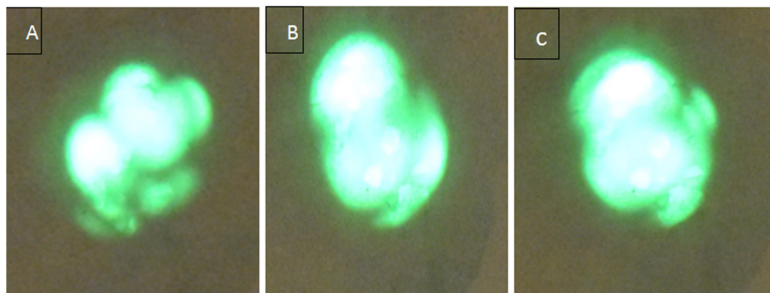


FIG. 7. The stability structure pattern for uncoated emitter type 2, at emission current $2.3 \mu\text{A}$ and applied voltage 1800 V; the duration time between obtaining the next images is 15 minutes.

The emission current patterns for coated emitters were taken at the same voltage values. The images were taken for the emission current patterns at the switch-on voltage and then, the voltage was regularly decreased, where the FEM image primarily consists of a single bright spot. Fig. 8 shows the emission current pattern of emitter type 1 after being coated with a 150 nm thick layer of EpoxyLite UPR- 4 resin followed by 4 nm of Au. Fig. 9 shows the emission current pattern of emitter type 2 after being coated with a 150 nm thick layer of EpoxyLite 478 resin followed by 4 nm of Au. The stability structure pattern for emitter type 1 after being coated with EpoxyLite UPR- 4 resin followed by 4 nm of Au is shown in Fig. 10. The stability structure pattern for emitter type 2 after being coated with EpoxyLite UPR- 4 resin followed by 4 nm of Au is also shown in Fig. 11. However, the stability structure patterns for the two types

of emitters have been taken at the same voltage and the duration time between obtaining the next images is 15 minutes.

From the comparison of the emission patterns, emission pattern stability and the SEM image show the tip geometry and surface. With that, it has been concluded that the emission current pattern and stability structure for the emission current from emitter type 2 (tungsten/ 150 nm 478 resin/ 4 nm Au) is more stable in comparison with the emission current from emitter type 1 (tungsten/ 150 nm UPR-4 resin/ 4 nm Au). The emitted electrons were concentrated in one single spot with high brightness, where a single bright spot formed. Also, the electrons will be emitted from the epoxy layer in different proportions, depending on the components of each type of epoxy.

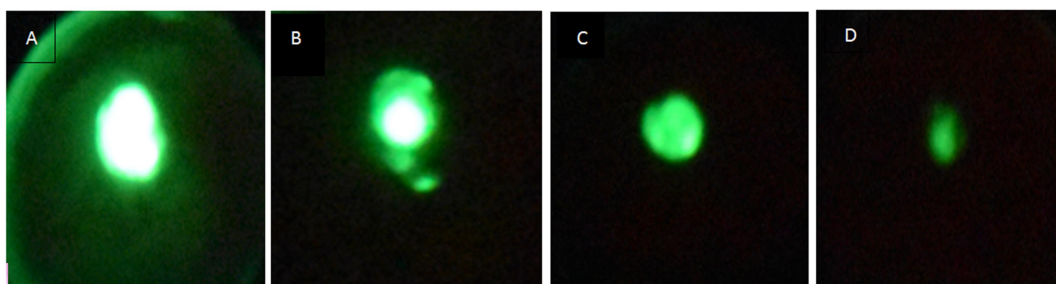


FIG. 8. Emission current pattern for emitter type 1 (Tungsten/ 150 nm UPR-4 resin/ 4 nm Au). A) Emission current $7 \mu\text{A}$, applied voltage 1600 V. B) Emission current $4 \mu\text{A}$, applied voltage 1400 V. C) Emission current $3.6 \mu\text{A}$, applied voltage 1200 V. D) Emission current $2.4 \mu\text{A}$, applied voltage 1000 V.

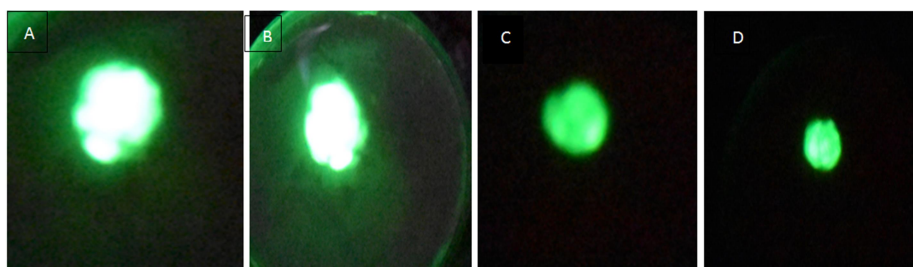


FIG. 9. Emission current pattern for emitter type 2 (Tungsten/ 150 nm 478 resin/ 4 nm Au) A) Emission current $10.6 \mu\text{A}$, applied voltage 1600 V. B) Emission current $9.4 \mu\text{A}$, applied voltage 1400 V. C) Emission current $8.3 \mu\text{A}$, applied voltage 1200 V. D) Emission current $2.5 \mu\text{A}$, applied voltage 900 V.

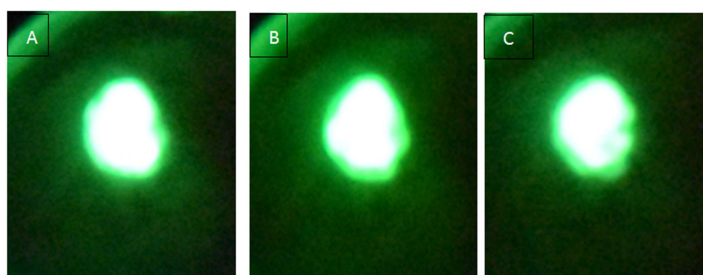


FIG. 10. The stability structure pattern for emitter type 1 (Tungsten/ 150 nm UPR-4 resin/ 4 nm Au), at emission current $10 \mu\text{A}$ and applied voltage 1800 V. The duration time between obtaining the next images is 15 minutes.

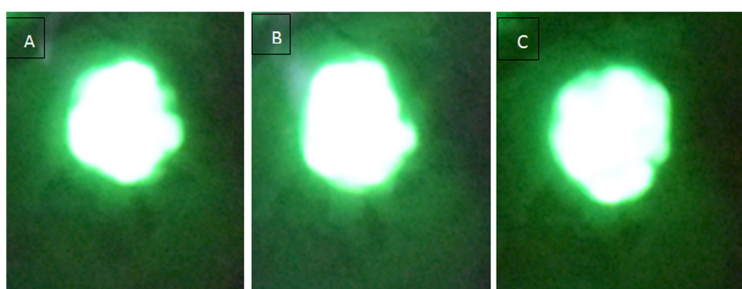


FIG. 11. The stability structure pattern for emitter type 2 (Tungsten/ 150 nm 478 resin/ 4 nm Au), at emission current $13 \mu\text{A}$ and applied voltage 1800V. The duration time between obtaining the next images is 15 minutes.

The (I-V) plot shows the total emission of current on voltage V externally applied between cathode and anode. Fig. 12A shows the I-V characteristics for uncoated emitter type 1. This typical curve for the non-ohmic behavior for tungsten emitter has been cleaned by alcohol, distilled water and ultrasonic bath. Fig. 12B shows the I-V characteristics for emitter type 1 after being coated with 150 nm EpoxyLite 478 resin. There were obvious fluctuations of

emission current while the voltage applied has been slowly applied throughout the emitter. At a certain threshold switching voltage value, $V_{\text{sw}} = 1600 \text{ V}$, the emission current starts from zero to $2 \mu\text{A}$, by decreasing the voltage of the line region of F-N plot that extends down to $V_{\text{SAT}} = 1300 \text{ V}$ with $I_{\text{SAT}} = 1.1 \mu\text{A}$, by decreasing the voltage of the emission current that vanishes at $V_{\text{TH}} = 600 \text{ V}$ with emission current $I_{\text{Th}} = 56.3 \text{ PA}$. Fig. 12C shows the I-V characteristics after

being coated with 150 nm with EpoxyLite UPR-4 resin followed by 4 nm of Au, where a switch-on phenomenon has been observed without detecting current fluctuations before switching the threshold switching voltage $V_{SW} = 1400$ V and switching current $I_{SW} = 5$ μ A, by decreasing

the voltage of the line region of F-N plot that extends down to $V_{SAT} = 700$ V with $I_{SAT} = 1.17$ μ A, by decreasing the voltage of the emission current that vanishes at $V_{TH} = 500$ V with emission current $I_{TH} = 86.4$ pA.

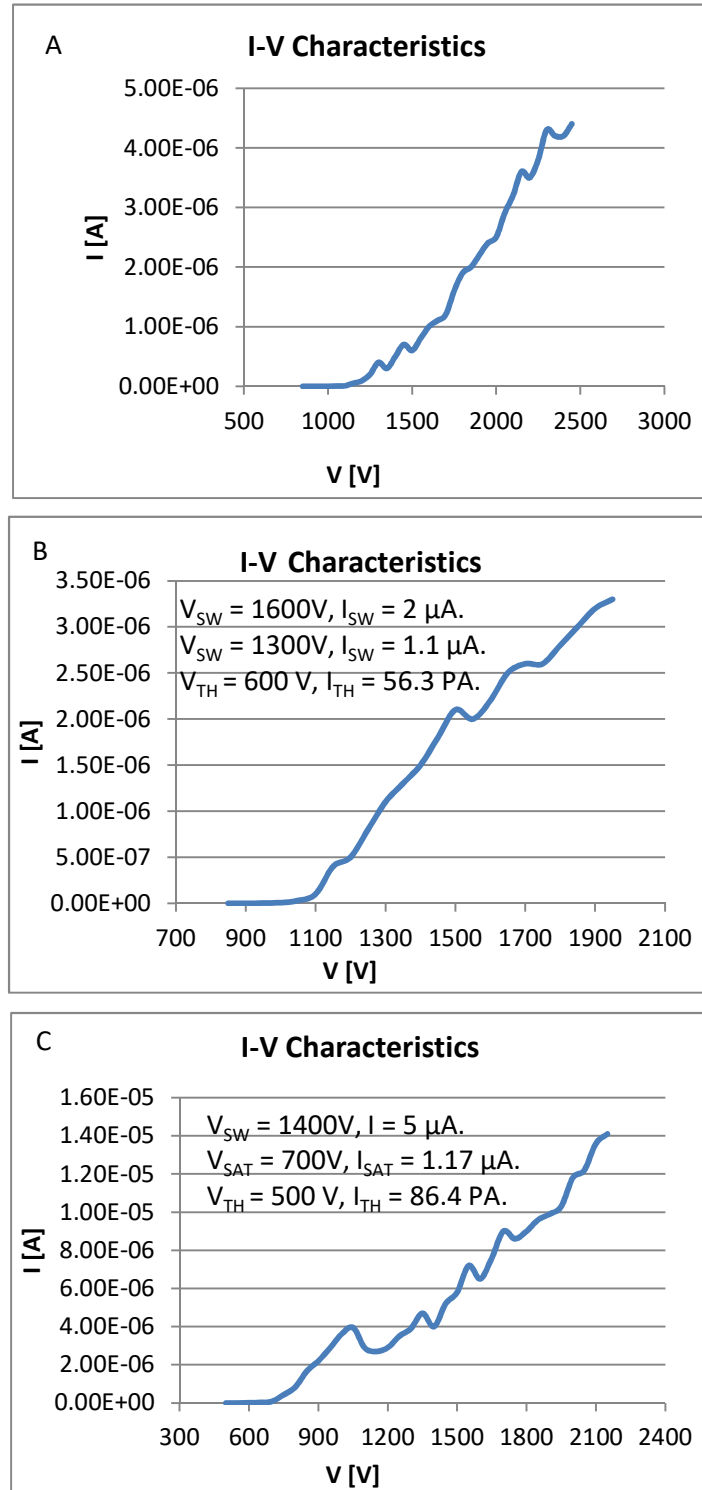
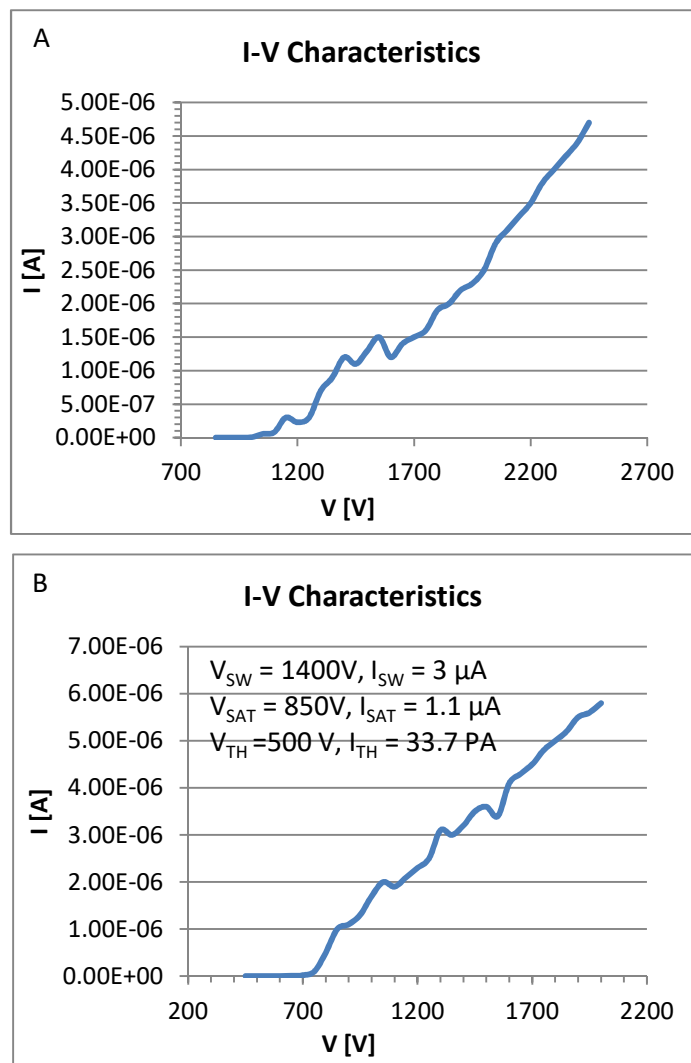


FIG. 12. The I-V characteristics. A) Uncoated emitter type 1. B) Emitter type 1(Tungsten/ 150 nm 478 resin), $V_{SW} = 1600$ V with $I_{SW} = 1.7$ μ A, $V_{SAT} = 1300$ V with $I_{SAT} = 1.1$ μ A, $V_{TH} = 600$ V, $I_{TH} = 56.3$ pA. C) Emitter type 1 (Tungsten/ 150 nm UPR-4 resin/ 4 nm Au), $V_{SW} = 1400$ V with $I_{SW} = 5$ μ A, $V_{SAT} = 850$ V with $I_{SAT} = 1.67$ μ A.

Fig. 13A shows the I-V characteristics for uncoated emitter type 2, as this is a typical curve for the non-ohmic behavior. Tungsten emitter has been cleaned by alcohol, distilled water and ultrasonic process. Fig. 13B shows the I-V characteristics for emitter type 2 after coating with 150 nm Epoxylite 478 resin. There were obvious fluctuations of emission current, while the voltage has been slowly applied throughout the emitter. At a certain threshold switching voltage value, $V_{sw} = 1400$ V the emission current starts from zero to $3 \mu\text{A}$, by decreasing the voltage of the line region of F-N plot that extends down to $V_{SAT} = 850$ V with $I_{SAT} = 1.1 \mu\text{A}$, by decreasing the voltage of the emission

current that vanishes at $V_{TH} = 500$ V with $I_{TH} = 33.7$ PA Fig. 13C shows the I-V characteristics after coating with 150 nm Epoxylite 478 followed by 4 nm of gold, where a switch-on phenomenon has been observed without detecting current fluctuations before switching the threshold switching voltage $V_{sw} = 1300$ V and the switching current $I_{sw} = 9 \mu\text{A}$, by decreasing the voltage of the line region of F-N plot that extends down to $V_{SAT} = 650$ V with $I_{SAT} = 1.12 \mu\text{A}$, by decreasing the voltage of the emission current that vanishes at $V_{TH} = 350$ V with $I_{TH} = 65.9$ PA.



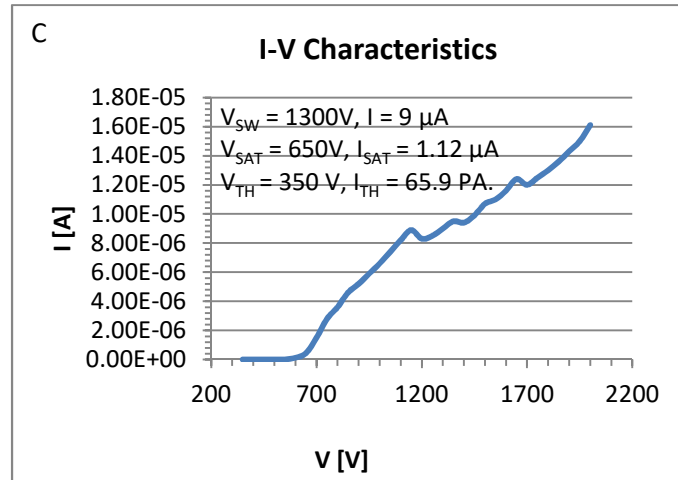


FIG.13. The I-V characteristics for A) Uncoated emitter type 2. B) Emitter type 2 (Tungsten/ 150 nm 478 resin), $V_{SW} = 1400 V$ with $I_{SW} = 3 \mu A$, $V_{SAT} = 850$ with $I_{SAT} = 1.1 \mu A$, $V_{TH} = 350 V$, $I_{TH} = 65.9 pA$. C) Emitter type 2 (Tungsten/ 150 nm 478 resin/ 4 nm Au), $V_{SW} = 1300 V$ with $I_{SW} = 9 \mu A$, $V_{SAT} = 700 V$ with $I_{SAT} = 1.12 \mu A$, $V_{TH} = 350 V$, $I_{TH} = 65.9 pA$.

The study of the second approach of I-V data is conducted through the Fowler-Nordheim (FN) plot via $\ln(\frac{1}{V^2})$ versus $(\frac{1}{V})$, as shown in Fig. 14. Curve (A) shows the characteristics of clean tungsten emitter type 1, while curve (B) shows the characteristics of tungsten emitter after being coated with 150 nm EpoxyLite UPR- 4 resin. However, curve (C) shows the characteristics of tungsten emitter after being coated with 150 nm

EpoxyLite UPR- 4 resin followed by 4 nm Au. Curve (A) of Fig. 15 shows the characteristics of clean tungsten emitter type 2, while curve (B) shows the characteristics of tungsten emitter after being coated with a 150 nm thick layer of EpoxyLite 478 resin. Curve (C) shows the characteristics of tungsten emitter after being coated with a 150 nm thick layer of EpoxyLite 478 resin followed by 4 nm Au.

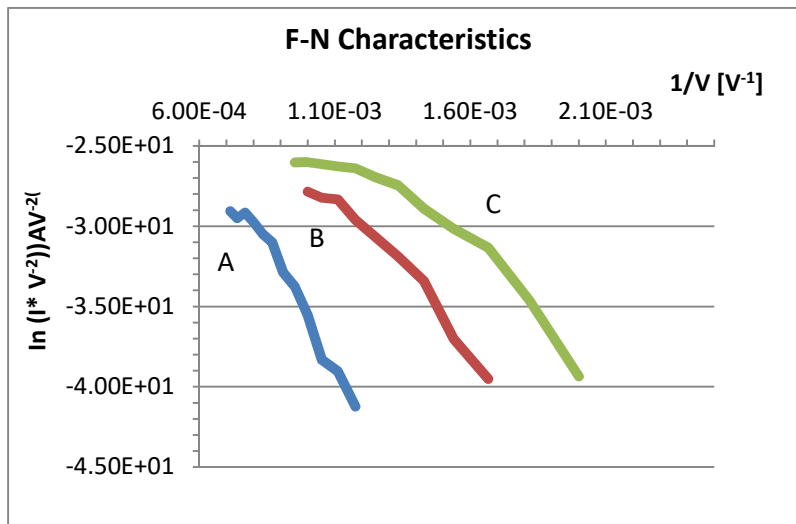


FIG. 14. The F-N plot for emitter type 1, where curve A is for clean emitter, curve B after being coated with a 150 nm thick layer of EpoxyLite UPR- 4 resin and curve C after being coated with a 150 nm thick layer of EpoxyLite UPR- 4 resin followed by 4 nm of Au.

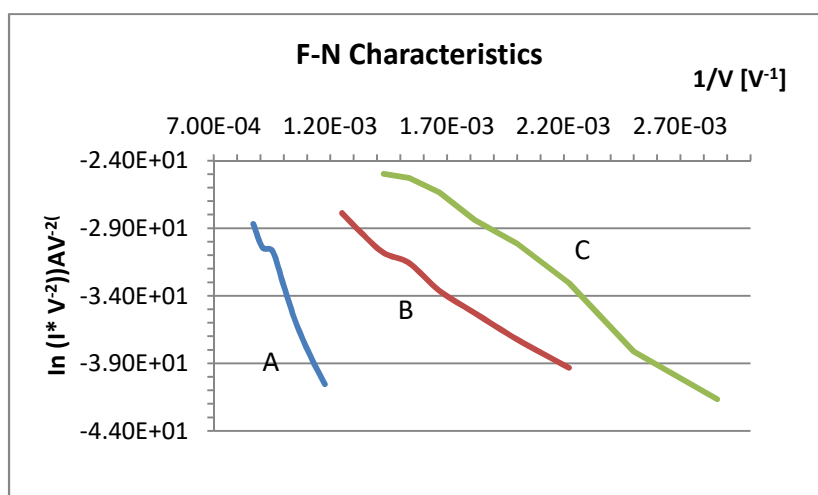


FIG. 15. The F-N plot for emitter type 2, where curve A is for clean emitter, curve B after being coated with a 150 nm thick layer of Epoxylite 478 resin curve C after being coated with a 150 nm thick layer of Epoxylite 478 resin followed by 4nm of Au.

The new composite micro emitters covered by Epoxylite resin and followed by Au layer had the following effects: A) The switch-on voltage for the emitter after being coated with epoxy layer followed by Au layer is lower than the switch-on voltage for clean emitters and the emitter is coated with epoxy layer only with high emission current. B) The F-N plots are approximately linear for emission current below 10^{-7} A with a duration of higher currents. C) The emission patterns are in the form of a very regular and concentrated spot more than the emission patterns for the clean emitter and the emission patterns for coated emitter with the epoxy layer only.

Conclusion

Details of new types of composite microstructure have been presented. The results confirmed that the excellent field emission behaviour of the coated emitter tip is a prospective candidate for advanced electron field emitters. The most important finding from this work is that the switch-on phenomenon occurs with the 2 types of the epoxy resin that were used even covered with the Au layer. Another

important finding is that the emission patterns, at the gross level, are in all cases relatively stable, as this is a necessary requirement if an emitter is to be used as an electron source. The switch-on voltage and the threshold switch-voltage have been decreased after coating the emitters with a dielectric material even after being covered with a thin layer of Au. This has been accompanied by a rise in the value of the emission current and stability in the electrons' emission patterns, where the electrons have been centered in the form of a bright spot. The field emission characteristics of a tungsten electron source are intrinsically changed by coating the tips with a micro-thin layer of epoxy resin covered with a thin layer of Au. This is in line with the results obtained from similar studies [19]. This change in the characteristics varied depending on the type of epoxy resin used in coating the tungsten tips.

Acknowledgments

The authors would like to thank the Deanship of Academic Research at Mu'tah University for supporting this work through research project number 241/19/120.

References

- [1] Latham, R.V. and Mousa, M.S., Journal of Physics D: Applied Physics, 19 (1986) 699.
- [2] Forbes, R.G., Deane, J.H.B., Fischer, A. and Mousa, M.S., Jordan J. Phys., 8 (3) (2015) 125.
- [3] Forbes, R.G., Mathematical, Physical and Engineering Sciences, 469 (2013) 20130271.
- [4] Mousa, M.S., Latham, R.V., Le Journal de Physique Colloques, 47 (1986) 139.
- [5] Mousa, M.S., Surface Science, 231 (1990) 142.

- [6] Mousa, M.S., Karpowicz, A. and Surma, S., *Vacuum*, 45 (1994) 249.
- [7] Forbes, R.G., Deane, J.H., Hamid, N. and Sim, H.S., *Journal of Vacuum Science & Technology*, 22 (2004) 1222.
- [8] Sergeev, E., Knápek, A. and Grmela, L., "Alternative conditions of preparing ultrasharp tungsten field-emission cathodes". (Institution of the University of Zilina, 2013).
- [9] Knápek, A., Sýkora, J., Chlumská, J. and Sobola, D., *Microelectronic Engineering*, 173 (2017) 42.
- [10] Latham, R.V. and Salim, M.A., *Journal of Physics E: Scientific Instruments*, 20 (1987) 181.
- [11] Ala'a, M., Al-Qudah, A.A., Mousa, M.S. and Fischer, I., *IOP Conference Series: Materials Science and Engineering*. IOP Publishing, 92 (2015) 01202.
- [12] Benada. O and Pokorný, V., *Journal of Electron Microscopy Technique*, 16 (1990) 235.
- [13] Mousa, M.S., *An International Journal Devoted to the Development and Application of Techniques for the Analysis of Surfaces, Interfaces and Thin Films*, 39 (2007) 102.
- [14] Mayer, A., Mousa, M.S. and Vigneron, J.P., *Ultramicroscopy*, 89 (2001) 95.
- [15] Ala'a, M. and Mousa M.S., *Applied Microscopy*, 46 (2016)155.
- [16] Meza, J.M., Lubin, C., Thoyer, F., Rosales, K.V., Espinoza, A.G., Martin, F. and Cousty, J., *Carbon*, 86 (2015) 363.
- [17] Zhou, W. and Wang, Z.L., (Eds.), "Scanning Microscopy for Nanotechnology", (Springer Science & Business Media, 2007).
- [18] FEI Company, "Introduction to Electron Microscope", (2010).
- [19] Mousa, M.S., *Surface Science*, 231 (1990), 142.

Authors Index

A. Abushattal.....	243
A. Al Soud.....	191, 253
A. Fattoum.....	181
A. Khasawneh	243
A. Knápek	191
A. Taani.....	243
A. Tachafine.....	201
A.A. Ramanathan	233
B. Assi.....	221
B. M. G. Melo	181
D. Fasquelle.....	201
D. Mezdour	227
H. Ait Laasri.....	201
H. Shehabi.....	211
J. -C. Carru	201
L. C. Costa.....	181, 201
M. Al-Wardat	243
M. E. Achour.....	181
M. E. Touhami	181
M. Elaatmani	201
M. P. F. Graça	181
M. Rekaby.....	211
M. S. Mousa	191, 253
M. Tabellout.....	227
M.W. Aqra	233
N. Almusleh	243
N. Tentillier.....	201
P. R. Prezas	181
R. Awad.....	211, 221
R. N. Al Buqain.....	253
R. Sayed Hassan.....	211
S. El Bouazzaoui	181
W. Malaeb.....	221
Y. Nioua.....	181
Z. Bitar	221

Subject Index

2D nanopores	233
Au layer	253
BaFe ₁₂ O ₁₉ Hexaferrite	211
Ceramic	201
Cold field emission.....	191, 253
Composites.....	181
Conductivity	201
Co-precipitation method.....	211, 221
Cyclotron lines	243
Desalination.....	233
Dielectric coating	253
Dielectric constant.....	227
Dielectric properties	181, 201, 211, 221
EpoxyLite 478	191
EpoxyLite UPR-4	191
Fillers	181
Glass transition.....	181
Graphene	181, 233
High-Mass X-ray binaries	243
Membrane	233
Nano emitter.....	253
NaOH molarity.....	221
Optical gap	227
Patents	233
Polyamide.....	227
Polyaniline.....	227
Polymer	227
Stars: magnetic field.....	243
Stars: neutron stars	243
Strontium calcium titanate.....	201
Structure	201
XRD	211
Yttrium Iron Garnet (YIG).....	221

المراجع: يجب طباعة المراجع بأسطر مزدوجة ومرقمة حسب تسلسلها في النص. وتكتب المراجع في النص بين قوسين مربعين. ويتم اعتماد اختصارات الدوريات حسب نظام Wordlist of Scientific Reviewers.

الجدول: تعطى الجداول أرقاماً متسلسلة يشار إليها في النص. ويجب طباعة كل جدول على صفحة منفصلة مع عنوان فوق الجدول. أما الحواشي التفسيرية، التي يشار إليها بحرف فوقي، فتكتب أسفل الجدول.

الرسوم التوضيحية: يتم ترقيم الأشكال والرسومات والرسومات البيانية (المخططات) والصور، بصورة متسلسلة كما وردت في النص.

تقبل الرسوم التوضيحية المستخرجة من الحاسوب والصور الرقمية ذات النوعية الجيدة بالأبيض والأسود، على أن تكون أصيلة وليست نسخة عنها، وكل منها على ورقة منفصلة ومعرفة برقمها بالمقابل. ويجب تزويد المجلة بالرسومات بحجمها الأصلي بحيث لا تحتاج إلى معالجة لاحقة، وألا تقل الحروف عن الحجم 8 من نوع Times New Roman، وألا تقل سماكة الخطوط عن 0.5 وكتافة متجانسة. ويجب إزالة جميع الألوان من الرسومات ما عدا تلك التي ستنشر ملونة. وفي حالة إرسال الرسومات بصورة رقمية، يجب أن تتوافق مع متطلبات الحد الأدنى من التمايز (1200 dpi Resolution) لرسومات الأبيض والأسود الخطية، و 600 dpi للرسومات باللون الرمادي، و 300 dpi للرسومات الملونة. ويجب تخزين جميع ملفات الرسومات على شكل (jpg)، وأن ترسل الرسوم التوضيحية بالحجم الفعلي الذي سيظهر في المجلة. وسواء أرسل المخطوط بالبريد أو عن طريق الشبكة (Online)، يجب إرسال نسخة ورقية أصلية ذات نوعية جيدة للرسومات التوضيحية.

مواد إضافية: تشجع المجلة الباحثين على إرفاق جميع المواد الإضافية التي يمكن أن تسهل عملية التحكيم. وتشمل المواد الإضافية أي اشتقاقات رياضية مفصلة لا تظهر في المخطوط.

المخطوط المنقح (المعدل) والأقراص المدمجة: بعد قبول البحث للنشر وإجراء جميع التعديلات المطلوبة، فعلى الباحثين تقديم نسخة أصلية ونسخة أخرى مطابقة للأصلية مطبوعة بأسطر مزدوجة، وكذلك تقديم نسخة إلكترونية تحتوي على المخطوط كاملاً مكتوباً على Microsoft Word for Windows 2000 أو ما هو استجد منه. ويجب إرفاق الأشكال الأصلية مع المخطوط النهائي المعدل حتى لو تم تقديم الأشكال إلكترونياً. وتخزن جميع ملفات الرسومات على شكل (jpg)، وتقدم جميع الرسومات التوضيحية بالحجم الحقيقي الذي ستظهر به في المجلة. ويجب إرفاق قائمة ببرامج الحاسوب التي استعملت في كتابة النص، وأسماء الملفات على قرص مدمج، حيث يعلم القرص بالاسم الأخير للباحث، وبالرقم المرجعي للمخطوط للمراسلة، وعنوان المقالة، والتاريخ. ويحفظ في مغلف واقٍ.

حقوق الطبع

يُشكّل تقديم مخطوط البحث للمجلة اعترافاً صريحاً من الباحثين بأن مخطوط البحث لم يُنشر ولم يُقدّم للنشر لدى أي جهة أخرى كانت وبأي صيغة ورقية أو إلكترونية أو غيرها. ويشترط على الباحثين ملء نموذج ينص على نقل حقوق الطبع لتصبح ملكاً لجامعة اليرموك قبل الموافقة على نشر المخطوط. ويقوم رئيس التحرير بتزويد الباحثين بنموذج نقل حقوق الطبع مع النسخة المُرسلة للتتقيح. كما ويُمنع إعادة إنتاج أي جزء من الأعمال المنشورة في المجلة من دون إذن خطي مُسبق من رئيس التحرير.

إخلاء المسؤولية

إن ما ورد في هذه المجلة يعبر عن آراء المؤلفين، ولا يعكس بالضرورة آراء هيئة التحرير أو الجامعة أو سياسة اللجنة العليا للبحث العلمي أو وزارة التعليم العالي والبحث العلمي. ولا يتحمل ناشر المجلة أي تبعات مادية أو معنوية أو مسؤوليات عن استعمال المعلومات المنشورة في المجلة أو سوء استعمالها.

الفهرسة: المجلة مفهرسة في:

	Emerging Sources Citation Index (ESCI)	
---	---	---

المجلة الأردنية للفيزياء هي مجلة بحوث علمية عالمية متخصصة مُحكمة تصدر بدعم من صندوق دعم البحث العلمي، وزارة التعليم العالي والبحث العلمي، عمان، الأردن. وتقوم بنشر المجلة عمادة البحث العلمي والدراسات العليا في جامعة اليرموك، إربد، الأردن. وتنتشر البحوث العلمية الأصيلة، إضافة إلى المراسلات القصيرة Short Communications، والملاحظات الفنية Technical Notes، والمقالات الخاصة Feature Articles، ومقالات المراجعة Review Articles، في مجالات الفيزياء النظرية والتجريبية، باللغتين العربية والإنجليزية.

تقديم مخطوط البحث

تقدم البحوث عن طريق إرسالها إلى البريد الإلكتروني : jjp@yu.edu.jo

تقديم المخطوطات إلكترونياً: اتبع التعليمات في موقع المجلة على الشبكة العنكبوتية.

ويجري تحكيم البحوث الأصيلة والمراسلات القصيرة والملاحظات الفنية من جانب مُحكمين اثنين في الأقل من ذوي الاختصاص والخبرة. وتُشجّع المجلة الباحثين على اقتراح أسماء المحكمين. أما نشر المقالات الخاصة في المجالات الفيزيائية النشطة، فيتم بدعوة من هيئة التحرير، ويُشار إليها كذلك عند النشر. ويُطلب من كاتب المقال الخاص تقديم تقرير واضح يتسم بالدقة والإيجاز عن مجال البحث تمهيداً للمقال. وتنتشر المجلة أيضاً مقالات المراجعة في الحقول الفيزيائية النشطة سريعة التغير، وتشجّع كاتبي مقالات المراجعة أو مُسكّتيها على إرسال مقترح من صفحتين إلى رئيس التحرير. ويرفّق مع البحث المكتوب باللغة العربية ملخص (Abstract) وكلمات دالة (Keywords) باللغة الإنجليزية.

ترتيب مخطوط البحث

يجب أن تتم طباعة مخطوط البحث ببنت 12 نوعه Times New Roman، وبسطر مزدوج، على وجه واحد من ورق A4 (21.6 × 27.9 سم) مع حواشي 3.71 سم، باستخدام معالج كلمات ميكروسوفت وورد 2000 أو ما استُجد منه. ويجري تنظيم أجزاء المخطوط وفق الترتيب التالي: صفحة العنوان، الملخص، رموز التصنيف (PACS)، المقدمة، طرق البحث، النتائج، المناقشة، الخلاصة، الشكر والعرفان، المراجع، الجداول، قائمة بدليل الأشكال والصور والإيضاحات، ثمّ الأشكال والصور والإيضاحات. وتُكتب العناوين الرئيسية بخط غامق، بينما تُكتب العناوين الفرعية بخط مائل.

صفحة العنوان: وتشمل عنوان المقالة، أسماء الباحثين الكاملة وعناوين العمل كاملة. ويكتب الباحث المسؤول عن المراسلات اسمه مشاراً إليه بنجمة، والبريد الإلكتروني الخاص به. ويجب أن يكون عنوان المقالة موجزاً وواضحاً ومعبراً عن فحوى (محتوى) المخطوط، وذلك لأهمية هذا العنوان لأغراض استرجاع المعلومات.

الملخص: المطلوب كتابة فقرة واحدة لا تزيد على مائتي كلمة، موضحة هدف البحث، والمنهج المتبع فيه والنتائج وأهم ما توصل إليه الباحثون.

الكلمات الدالة: يجب أن يلي الملخص قائمة من 4-6 كلمات دالة تعبر عن المحتوى الدقيق للمخطوط لأغراض الفهرسة.

PACS: يجب إرفاق الرموز التصنيفية، وهي متوفرة في الموقع <http://www.aip.org/pacs/pacs06/pacs06-toc.html>.

المقدمة: يجب أن توضّح الهدف من الدراسة وعلاقتها بالأعمال السابقة في المجال، لا أن تكون مراجعة مكثفة لما نشر (لا تزيد المقدمة عن صفحة ونصف الصفحة مطبوعة).

طرائق البحث (التجريبية / النظرية): يجب أن تكون هذه الطرائق موضحة بتفصيل كاف لإتاحة إعادة إجرائها بكفاءة، ولكن باختصار مناسب، حتى لا تكون تكراراً للطرائق المنشورة سابقاً.

النتائج: يستحسن عرض النتائج على صورة جداول وأشكال حيثما أمكن، مع شرح قليل في النص ومن دون مناقشة تفصيلية.

المناقشة: يجب أن تكون موجزة وتركز على تفسير النتائج.

الاستنتاج: يجب أن يكون وصفاً موجزاً لأهم ما توصلت إليه الدراسة ولا يزيد عن صفحة مطبوعة واحدة.

الشكر والعرفان: الشكر والإشارة إلى مصدر المنح والدعم المالي يكتبان في فقرة واحدة تسبق المراجع مباشرة.

Jordan Journal of

PHYSICSAn International Peer-Reviewed Research Journal issued by the
Support of the Scientific Research Support Fund

Published by the Deanship of Research & Graduate Studies, Yarmouk University, Irbid, Jordan

Name: الأسم:
 Specialty: التخصص:
 Address: العنوان:
 P.O. Box: صندوق البريد:
 City & Postal Code: المدينة/الرمز البريدي:
 Country: الدولة:
 Phone: رقم الهاتف:
 Fax No: رقم الفاكس:
 E-mail: البريد الإلكتروني:
 No. of Subscription: عدد الاشتراكات:
 Method of Payment: طريقة الدفع:
 Amount Enclosed: المبلغ المرفق:
 Signature: التوقيع:

Cheques should be paid to Deanship of Research and Graduate Studies - Yarmouk University.

I would like to subscribe to the Journal
For

- One Year
 Two Years
 Three Years

One Year Subscription Rates

	Inside Jordan	Outside Jordan
Individuals	JD 8	€ 40
Students	JD 4	€ 20
Institutions	JD 12	€ 60

Correspondence**Subscriptions and Sales:**

Prof. Ibrahim O. Abu Al-Jarayesh
 Deanship of Research and Graduate Studies
 Yarmouk University
 Irbid – Jordan
Telephone: 00 962 2 711111 Ext. 2075
Fax No.: 00 962 2 7211121



جامعة اليرموك



المملكة الأردنية الهاشمية

المجلة الأردنية

للفيزياء

مجلة بحوث علمية عالمية متخصصة محكمة
تصدر بدعم من صندوق دعم البحث العلمي

المجلة الأردنية
للفيزياء
مجلة بحوث علمية عالمية محكمة

المجلد (13)، العدد (3)، كانون الأول 2020م / جمادى الأولى 1442هـ

المجلة الأردنية للفيزياء: مجلة علمية عالمية متخصصة محكمة تصدر بدعم من صندوق دعم البحث العلمي، عمان، الأردن، وتصدر عن عمادة البحث العلمي والدراسات العليا، جامعة اليرموك، إربد، الأردن.

رئيس التحرير:

ابراهيم عثمان أبو الجرايش

قسم الفيزياء، جامعة اليرموك، إربد، الأردن.

ijaraysh@yu.edu.jo

هيئة التحرير:

نبيل يوسف أيوب

رئيس الجامعة الأمريكية في مادبا، مادبا، الأردن.

nabil.ayoub@gju.edu.jo

جميل محمود خليفة

قسم الفيزياء، الجامعة الأردنية، عمان، الأردن.

jkalifa@ju.edu.jo

طارق فتحي حسين

قسم الفيزياء، الجامعة الأردنية، عمان، الأردن.

t.hussein@ju.edu.jo

مروان سليمان الموسى

قسم الفيزياء، جامعة مؤتة، الكرك، الأردن.

mmousa@mutah.edu.jo

محمد خالد الصغير

قسم الفيزياء، الجامعة الهاشمية، الزرقاء، الأردن.

msugh@hu.edu.jo

عبد المجيد الياسين

قسم الفيزياء، جامعة اليرموك، إربد، الأردن.

alyassin@yu.edu.jo

محمد العمري

قسم الفيزياء، جامعة العلوم والتكنولوجيا، إربد، الأردن.

alakmoh@just.edu.jo

إبراهيم البصول

قسم الفيزياء، جامعة آل البيت، المفرق، الأردن.

Ibrahimbsoul@yahoo.com

سكرتير التحرير: مجدي الشناق

ترسل البحوث إلى العنوان التالي:

الأستاذ الدكتور إبراهيم عثمان أبو الجرايش
رئيس تحرير المجلة الأردنية للفيزياء
عمادة البحث العلمي والدراسات العليا، جامعة اليرموك
إربد، الأردن

هاتف 00 962 2 7211111 فرعي 2075

E-mail: jjp@yu.edu.jo Website: <http://Journals.yu.edu.jo/jjp>